Dissertation

submitted to the

Combined Faculties of the Natural Sciences and Mathematics

of the Ruperto-Carola-University of Heidelberg, Germany

for the degree of

Doctor of Natural Science

Put forward by

Diplom-Physiker Karsten Dittrich

Born in: Rostock, Germany

Oral Examination: 30.10.2013

Numerical Simulations of Planetesimal Formation in Protoplanetary Disks

Referees: Priv.-Doz. Dr. Hubert Klahr

                          Prof. Dr. Cornelis P. Dullemond

Zusammenfassung

In der ersten Stufe der Planetenentstehung wachsen mikrometergroße Staubteilchen in einer protoplanetaren Scheibe durch inelastische Stöße. Dieses Wachstum wird ineffizient, sobald die Partikel mehrere Zentimeter oder, je nach Entfernung zum Stern, Meter groß werden. Die entstandenen Agglomerate werden durch Turbulenz in der Scheibe weiter konzentriert bis sie Dichten erreichen, unter denen sie durch Eigengravitation zu 100 km großen Planetesimalen fragmentieren.

In meiner Doktorarbeit simuliere ich die Konzentration von Staubteilchen im turbulenten Gas der protoplanetaren Scheibe. Dabei behandele ich das Gas als eine Flüssigkeit und löse die magnetohydrodynamischen Gleichungen mit dem PENCIL CODE. Staubteilchen werden als kollisionsfreie Punktteilchen simuliert, welche mit dem Gas über Reibung wechselwirken und sich gegenseitige gravitativ anziehen können. Zunächst teste ich die Darstellung der Partikel im PENCIL CODE durch einen Vergleich einer Simulation der Rayleigh-Taylor-Instabilität (RTI) einer staubhaltigen Flüssigkeit mit der klassischen RTI-Simulation zweier Flüssigkeiten. Außerdem simuliere ich die Sedimentation einer Schicht aus Staubteilchen in einer Flüssigkeit welche experimentell überprüfbare Daten liefert.

Desweiteren studiere ich zonale Strömungen und die resultierenden langlebigen radialen Druckmaximum (axialsymmetrisch), die in Simulationen der Magnetorotationsinstabilität entstehen. Zonale Strömungen sind Ringe aus Gas, das schneller oder langsamer als das druckgestützte Keplersche Rotationsprofil rotieren. Sie entstehen durch zeitliche und räumlich Fluktuationen im magnetischen Druck. In einer Konvergenzstudie bestimmte ich die typische radiale Ausdehnung zu 5 bis 7 vertikalen Gas-Druckskalenhöhen mit einer Lebensdauer von bis zu 50 Umlaufperioden ($T_{\mathrm{orb}} = 2\pi\Omega^{-1}$). Partikel werden in diesen Druckmaxima eingefangen. Für Staubteilchen mit einer Reibungszeit $\tau_{\mathrm{f}} \sim 0.1\Omega^{-1}$ finde ich Konzentrationen, die einige hundert mal höher sind als zu Beginn. Größere Teilchen ($\tau_{\mathrm{f}} \geq 0.5\Omega^{-1}$) erreichen Dichten, die 10.000 mal höher sind als die Anfangsdichte. Das ist ausreichend, um sekundäre Instabilitäten wie die Strömungsinstabilität und einen Gravitationskollaps zu starten.

Die Strömungsinstabilität im Zusammenhang mit zonalen Strömungen untersuchte ich in höher aufgelösten Simulationen. Diese berücksichtigen die Rückreaktion der Teilchen auf das Gas. Diese Simulationen zeigen, dass das radiale Druckmaximum genug Teilchen ansammeln können, um die Strömungsinstabilität selbst mit kleineren Teilchen ($\tau_{\mathrm{f}} = 0.1\Omega^{-1}$) auszulösen. Bei Berücksichtigung der Eigengravitation entstehen Staubklumpen, die allerdings die Gezeitenkräfte nicht überstehen können. Das liegt hier an der nicht ausreichenden Auflösung.

Für mein letztes Projekt untersuchte ich den Kollaps einer kugelförmigen Wolke aus Staub in Simulationen mit einer sehr viel höheren Auflösung als in den obigen Simulationen. In dieser Studie betrachte ich Staubwolken mit einer Anfangsdichte von der Roche-Dichte ρ_{Roche} bis zu $10^{-3}\rho_{\mathrm{Roche}}$. Staubwolken mit einer Anfangsdichte von $0.1\rho_{\mathrm{Roche}}$, wie ich sie in großskaligen Simulationen typischerweise erreiche, fragmentieren zu einem Schwarm gravitationsgebundener Objekte mit einer Größenverteilung, die mit der Größenverteilung von Asteroiden vergleichbar ist.

Abstract

In the first step of planet formation micrometer-sized dust grains grow in a protoplanetary disk through collisional sticking. This growth becomes inefficient at several centimeters up to meters in size, depending on the distance to the star. The resulting agglomerates are concentrated by turbulence in the disk up to densities at which they fragment through self-gravitaty to 100 km sized planetesimals.

In my PhD thesis I simulate the concentration of dust particles in the turbulent gas flow of protoplanetary disks. Here I treat the gas as a fluid and solve the magnetohydrodynamic equations with the PENCIL CODE. Dust particles are simulated as non-collisional point particles, decoupled from the grid. At first I test the particle representation of the PENCIL CODE by comparing a Rayleigh-Taylor instability (RTI) simulation of a dust-laden fluid with a classical two-layer fluid RTI simulation. Additionally I simulate the sedimentation of a dust clump in a fluid which can be compared with experiments.

Further I study zonal flows and the resulting long-lived axisymmetric pressure bumps that are created in magnetorotational instability simulations. Zonal flows are described by annuli of gas rotating faster or slower than the pressure-supported Keplerian rotation. They are created by temporal and spacial variances in the magnetic pressure. In a convergence study I measured a typical radial size of 5 to 7 vertical gas pressure scale heights with a life time of up to 50 local orbits ($T_{\mathrm{orb}} = 2\pi\Omega^{-1}$). Particles get captured by these pressure bumps. For dust particles with a friction time $\tau_{\mathrm{f}} \geq 0.1\Omega^{-1}$ I found concentrations that are some hundred times higher than initially. Larger particles ($\tau_{\mathrm{f}} \geq 0.5\Omega^{-1}$) reach densities 10,000 times higher than their initial densities, sufficient to trigger secondary instabilities such as the streaming instability and gravitational collapse.

I study the streaming instability in a zonal flow environment in simulations of higher resolution including the back-reaction drag from particles to the gas. These simulations show that the axisymmetric pressure bumps can accumulate enough particles to trigger the streaming instability, even with small particles ($\tau_{\mathrm{f}} = 0.1\Omega^{-1}$). Allowing for self-gravity dust clumps form, yet they are not stable against tidal forces. This is due to the insufficient resolution here.

For my last project I studied the final collapse of a spherical dust cloud with a much higher resolution than in the above simulations. In this study I investigate a dust cloud with an initial density ranging from Roche density ρ_{Roche} down to $10^{-3}\rho_{\mathrm{Roche}}$. Dust spheres with $0.1\rho_{\mathrm{Roche}}$, like I typically get from large scale simulations, fragment to a swarm of bound objects with a size distribution that is comparable to the observed size distribution of asteroids.

Contents

List of Figures

List of Tables

x

Chapter 1

Introduction

1.1 Historical Overview

The origin of our planet and the solar system is subject of the earliest known writings. While our view changed particularly with the acceptance of heliocentrism (Copernicus, 1543), there are still many difficulties in the currently accepted hypothesis. The term "Solar System" was first used in the 17th century (Galilei et al., 1663). Emanuel Swedenborg first proposed the nebular theory (Swedenborg, 1734). Immanuel Kant later suggested that planets form out of local density enhancements which orbit the sun (Kant, 1755). Interestingly Kant explains the formation of planets such that small particles stick together until they become gravitationally unstable once they reached a certain size. That view is not so different from the modern formation picture.

Pierre Simon de Laplace formulated the theory that solar material forms a flat disk (Laplace and Young, 1832), which then formed the planets. This was the first mention of a protoplanetary disk. They hypothesized that the disk forms rings which then condensed into planets.

Other scenarios such as capture were proposed. Early theories (Chamberlin, 1901, 1916; Moulton, 1905) investigated the formation of planetesimals by a close encounter with another star. The resulting disruption of the Sun's surface lead to the eruption of huge flares. Planetesimals were condensed out of these flares and formed planets by collisions with each other.

Most of these theories were disproved completely or in part over the years. The modern theory was mainly formulated by Weizsäcker (1943). According to him planets are a by-product of star formation.

1.2 Modern View on Planet Formation

Star formation takes place in molecular clouds. If a region gets more massive than the Jeans mass (Jeans, 1902), it undergoes gravitational collapse. Most of the mass ends
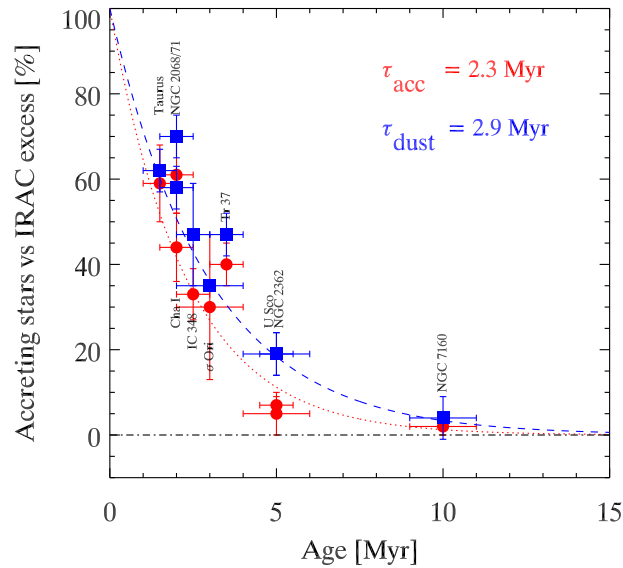
Figure 1.1 Ultra-violet (UV) excess (read dots) and infra-red (IR) excess (blue squares) against age of the stars. Exponential fits are in dotted red and dashed blue lines. They estimate the life-time of the UV excess and IR excess respectively. This plot was taken from Fedele et al. (2010) with kind permisson of the author.

up in the pre-stellar core (Hoyle, 1960; Cameron, 1962; Terebey et al., 1984). The small specific angular momentum, that always exist in molecular clouds (Weizsäcker, 1951; Fleck, 1980), add up as matter is accreted by the core. The material spins faster around the newborn star and finally builds a stable disk – the protoplanetary disk. This disk consists of only 1% to 10% (Weidenschilling, 1977a; Cassen and Moosman, 1981) of the mass of the entire system, but contains the vast majority of the angular momentum. The inner-most regions of the disk are constantly accreting onto the star. High energy ultra-violet (UV) radiation is the result of that accretion. This UV excess is visible at many young stellar objects (Mendigutía et al., 2011). Many disks also show an infra-red (IR) excess (Mendigutía et al., 2012). The IR excess is emitted by micrometer-sized dust grains. Measuring the age of a star along with the UV and IR excess allows an estimation for the life-time of protoplanetary disks.

The mean life-time is estimated to be 2.3 million years for the gas[1] and 3 million years for the dust[2] (see Figure 1.1, Fedele et al. (2010))[3]. Thus, the time scale in which planetesimals must be formed is about 2 million years. Smaller dust grains are replenished by planetesimal collisions. This process is inefficient after about 3 million years. The UV excess shows that mass is accreted onto the star. This is only possible if angular momentum is transported outwards, allowing gas to spiral inwards. In an idealized way, the angular momentum transport in a protoplanetary disk can be described with an alpha-disk model (Shakura and Sunyaev, 1973). There the turbulent

---

[1]hydrogen and helium
[2]condensations of elements heavier than helium
[3]A newer study (Bell et al., 2013) shows that the life-time can be a factor of 2 longer.

viscosity is

$$\nu_t = \alpha c_s H \,, \tag{1.1}$$

where α is a dimensionless parameter, c_s is the isothermal sound speed, and $H = H(R)$ is the gas pressure scale height, a function of the radial distance R to the star.

The general understanding of how planets in our Solar System form was detailed in Safronov (1969). The dust in protoplanetary disks needs to be concentrated by a mechanism that does not heat it up too much in a dynamical sense. The concentrating mechanism I investigate in my work is the magneto-rotational instability (MRI, Balbus and Hawley, 1991, 1998) described in Section 1.3.1. The resulting large-scale pressure bumps are able to concentrate dust enough to trigger further concentration processes such as the streaming instability (Youdin and Johansen, 2007; Johansen and Youdin, 2007). This instability is described in Section 1.3.3. When a reservoir of dust is sufficiently cold and dense it becomes gravitationally unstable (Jeans, 1902; Kopal, 1989). Planetesimals are gravitationally bound objects that sweep up dust grains and grow to protoplanets, the dominant planetesimals in their orbit.

1.2.1 From Planetesimals to Planets

Planetesimals accrete material from their feeding zone (Weidenschilling, 1976; Zhou and Lin, 2007). This zone has the size of a few Hill radii (Hamilton and Burns, 1992)

$$R_{\text{Hill}} = \left(\frac{m}{3M_\odot} \right)^{1/3} a(1-e) \,, \tag{1.2}$$

where m is the mass of the planetesimal, $M_\odot$ the mass of the Sun (or the star in a more general case), a and e are the semi-major axis and the eccentricity of the orbit, respectively. Slightly more massive planetesimals will grow faster than other planetesimals and decouple from the mass function. This process is called runaway growth. The formed objects become dominant in their orbit and form the protoplanets. Further accretion of material after the disk dissipates creates planets from the protoplanets.

The first step in planet formation is to form gravitationally bound objects, the planetesimals, from micrometer-sized dust particles. The growth from agglomerates of molecules (a few µm) up to planetesimals (> 1 km) is described in the following section.

1.3 Planetesimal Formation

When molecules collide, they stick to each other due to Van der Waals forces and build agglomerates. These fluffy agglomerates grow further by low-velocity collisions with other agglomerates. The resulting objects are more compact and can be referred to as dust particles. Dust particles grow due to coagulation (Weidenschilling et al., 1997). However, coagulation models show that there are several barriers to overcome to grow dust large enough to become gravitationally bound in kilometer-sized planetesimals,

such as the bouncing barrier (Zsom et al., 2010; Windmark et al., 2012a,b), the frag-
mentation barrier (e.g. Beitz et al., 2011; Birnstiel et al., 2012, and references therein),
and the kilometer-size barrier (Ida et al., 2008; Cuzzi et al., 2008). Dust growth mech-
anisms are summarized in Dominik et al. (2007) and the review of Blum and Wurm
(2008) gives an overview on the mentioned barriers.

This work addresses the fragmentation barrier or meter-size barrier. Pebbles of
several decimeters in size will drift very fast inwards due to the headwind from the
sub-Keplerian gas (Weidenschilling, 1977a). Thus, dust has to grow very quickly from
some centimeters to several kilometers in size in order to avoid drifting into the inner
region of the protoplanetary disk and onto the star. Turbulence in protoplanetary disks
around young stars provides promising mechanisms for rapid planetesimal formation
(Johansen et al., 2007, 2011). The MRI is the source of the turbulence in my simulations
and is described in the following section.

1.3.1   Magneto-Rotational Instability

The magneto-rotational instability (MRI) in the context of protoplanetary disks was
first studied in Balbus and Hawley (1991). After this linear analysis they studied the
non-linear evolution (Hawley and Balbus, 1991), the long-term evolution in a shearing
sheet (Hawley and Balbus, 1992), and the effect of non-axisymmetric perturbations
(Balbus and Hawley, 1992).

The MRI acts in differentially rotating disks with weak magnetic fields. Strong
magnetic fields tend to destroy small eddies and damp any instability. A simple treat-
ment of the MRI was described in Balbus and Hawley (1998): For this simplification,
I treat the protoplanetary disk as an axisymmetric gas disk with a weak vertical mag-
netic field $\boldsymbol{B} = B_z\hat{\boldsymbol{z}}$. This field does not disturb the equilibrium of gravitational and
rotational forces. A fluid element in the disk is displaced from its circular orbit by
$\boldsymbol{\xi} = \xi_R\hat{\boldsymbol{R}} + \xi_\phi\hat{\boldsymbol{\phi}}$ with a vertical oscillation proportional to e^{ikz}. The induction equa-
tion in real space $\omega\delta\boldsymbol{B} = kB_z\delta\boldsymbol{u}$, where ω is the oscillation frequency and $\boldsymbol{u}$ is the gas
velocity, is transformed to

$$\delta\boldsymbol{B} = \mathrm{i}kB_z\boldsymbol{\xi} \tag{1.3}$$

in Fourier space. Thus, the displacement $\boldsymbol{\xi}$ results in a change of the magnetic field
$\delta\boldsymbol{B} = \delta B_R\hat{\boldsymbol{R}} + \delta B_\phi\hat{\boldsymbol{\phi}}$ which lies in the orbital plane. The magnetic tension force is then

$$\frac{\mathrm{i}kB_z}{4\pi\rho}\delta\boldsymbol{B} = -\left(\boldsymbol{k}\cdot\boldsymbol{c}_A\right)^2\boldsymbol{\xi}\,, \tag{1.4}$$

where ρ is the gas volume density and $\boldsymbol{c}_A$ is the Alfvén velocity. The equations of
motion then take the simple form of two coupled, damped harmonic oscillators

$$\ddot{\xi}_R - 2\Omega\dot{\xi}_\phi = \left[\frac{d\Omega^2}{d\ln R} + (\boldsymbol{k}\cdot\boldsymbol{c}_A)^2\right]\xi_R\,, \tag{1.5}$$

$$\ddot{\xi}_\phi + 2\Omega\dot{\xi}_R = -(\boldsymbol{k}\cdot\boldsymbol{c}_A)^2\xi_\phi\,,$$

where $\Omega = \sqrt{GM_\odot/R^3}$ is the Keplerian angular velocity. In these equations 2Ω rep-
resents the Coriolis force and $d\Omega^2/d\ln R$ represents the tidal force. The equations 1.5
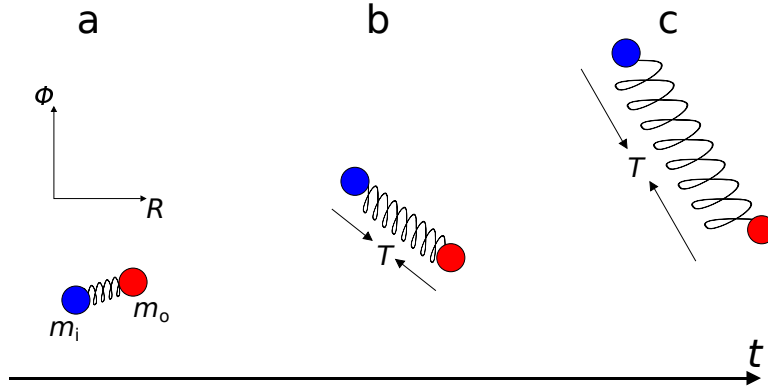
Figure 1.2 This simplified picture explains how the magneto-rotation instability (MRI) acts in a protoplanetary disk. The two fluid elements (or point masses) are orbiting the star with the main gas flow. The vertical magnetic field acts like a weak spring (with tension T) that is attached to both masses. Initially (a) both masses are close to each other, but on slightly different orbits. The inner mass m_i is in a slightly faster orbit than the outer mass m_o (b). Angular momentum is transported from m_i to m_o by stretching the spring. The inner mass loses angular momentum (c) and drops to inner, faster rotating orbits. The outer mass gains angular momentum and is forced to move through slower rotating outer orbits. This increases the tension and creates a runaway process.

are the leading-order WKB equations for local fluid displacements in a magnetized disk. They can, however, also be used to describe two orbiting point masses that are connected by a spring with spring constant $K = (\mathbf{k} \cdot \mathbf{c}_A)^2$. This analogy is shown in Figure 1.2.

From the right-hand side in equation (1.5) one can extract the stability requirement for the MRI as

$$(\mathbf{k} \cdot \mathbf{c}_A)^2 > -\frac{d\Omega^2}{d\ln R}\,. \tag{1.6}$$

Since the left-hand side of this equation is always positive, stability is only achieved if

$$\frac{d\Omega^2}{d\ln R} > 0\,. \tag{1.7}$$

This is, except for anomalous regions, never true in protoplanetary disks. One can always choose a small enough k in order to have instability. The corresponding length ($k_{\mathrm{MRI}} = 2\pi/\lambda_{\mathrm{MRI}}$) needs to fit into the disk height which I approximate here by twice the gas pressure scale height H. Then equation (1.6) becomes

$$c_A^2 = -\frac{1}{k^2}\frac{d\Omega^2}{d\ln R} \approx -\frac{H^2}{\pi^2}\frac{d\Omega^2}{d\ln R} \approx \frac{6}{\pi^2}c_s^2\,. \tag{1.8}$$

This relation assumes an isothermal Gaussian density profile for the vertical dimension of the disk. Relation 1.8 means that the Alfvén velocity must exceed the sound speed to stabilize all wavelengths. For weak magnetic fields $|c_A|$ is small. Thus, the MRI always works in the presence of weak magnetic fields.

1.3.2   Zonal Flows

Zonal flows are a product of large-scale variations in the magnetic field that transport momentum differentially, thus creating regions of slightly faster and slightly slower rotating gas. Large-scale pressure bumps are excited through geostrophic balance. This creates long-lived over-densities that potentially trap dust particles. I describe the creation of zonal flows in my simulations more thoroughly in Section 3.2. A simplified explanation is the fact that the turbulence parameter α is not a constant in MRI, but a function of R and t. These fluctuations lead to locally varying angular momentum transportation and excite zonal flows. A more complete theory on zonal flows and their creation is found in Johansen et al. (2009a). They found that zonal flows always populate the largest radial mode available in the local box approximation. In their largest box they simulated $L_{\mathrm{x}} = L_{\mathrm{y}} = 10.56H$, where L_{i} is the length of the simulation domain in direction i. More recently Simon et al. (2012) found a more complex structure in their largest simulation with $L_{\mathrm{x}} = 16H$. They further studied the autocorrelation function (Guan et al., 2009) of the magnetic field and the gas density. Both have a two component structure. The first is tilted with respect to the azimuthal axis and highly localized. The second component is seen at the largest scales and can be associated with the (predominantly toroidal) background magnetic field. Simon et al. (2012) measure the radial length scale of the zonal flows to converge at $6H$.

In this work I consider even larger physical extents for zonal flow structures. This gives me the opportunity to measure physical properties such as size and life-time independent of the simulated domain. Further, I investigate properties of the zonal flows in radially and azimuthally stretched boxes. I alter the radial and azimuthal domain up to $\sim 20H$.

Additionally, I study the behavior of dust in zonal flows. Whipple (1972) was the first to suggest that axisymmetric pressure bumps can trap gas. Pinilla et al. (2012) invoked zonal flows as a possibility to explain the sub-millimeter and millimeter-sized particles observed in protoplanetary disks. They used artificial static density bumps introduced as sinusoidal density perturbations with different amplitudes (e.g., $A = 0.1$ and $A = 0.3$) and different wavelengths ($\lambda = 0.3 \ldots 3H$). They found that a 30% density perturbation (with $\lambda = 1H$) is necessary to stop the drift of the dust grains. The present work is the first 3D MHD study that combines zonal flows and the reaction of dust particles on them.

Shearing box simulations (Brandenburg et al., 1995) are a powerful tool for analyzing the MRI as a source of turbulence. These simulations consider a local, co-rotating box, representing a small part of a Keplerian disk. Johansen et al. (2009a) reported long-lived axisymmetric sub- and super-Keplerian flows, zonal flows, in shearing box simulations of turbulence caused by the MRI. These zonal flows have been seen in several other local (Fromang and Stone, 2009; Stone and Gardiner, 2010; Simon et al., 2012) and global (Lyra et al., 2008; Dzyurkevich et al., 2010; Uribe et al., 2011; Flock et al., 2011, 2012) simulations using a wide variety of codes.

1.3.3   Particle Feedback and Streaming Instability

Solid bodies embedded in a protoplanetary disk have a different velocity than the ambient medium. The gas is pressure-supported and thus orbits with sub-Keplerian velocity. Particles, however move with Keplerian velocity on their orbit and feel a headwind $\Delta v_{\mathrm{HW}} = u_\phi^{(0)} - u_\phi = v_\phi - u_\phi$, where $u_\phi^{(0)}$ is the Keplerian velocity which is equal to the velocity of the particle v_ϕ. The headwind causes a radially inward drift of dust particles.

Solids moving through the gas create a tailwind that drags gas along. This effect becomes stronger, the higher the dust density is in relation to the gas density. Thus, when the density of solid and gas components become comparable, one has to consider the feedback from the dust particles to the gas. Youdin and Goodman (2005); Youdin and Johansen (2007) found that this feedback is capable of triggering a local, linear instability, the streaming instability (SI). The enhanced gas density due to the tailwind acts as an attractor for more particles, further increasing the feedback from the solid component. The SI can enhance the dust overdensity by a factor of 100 or more (Johansen and Youdin, 2007). The efficiency of the SI depends on dust particle size distribution.

1.4   Minor Bodies in the Solar System

The initial size distribution of objects in the asteroid belt (Bottke et al., 2005) and in the Kuiper belt (Nesvorný et al., 2010) has been retrieved from observational data and simulations that study the dynamics of these belts. Both studies claim that the size distribution has a steep part for objects with a diameter $> \approx 100\,\mathrm{km}$ and a shallow slope for smaller objects. Figure 1.3 shows a derived initial size distribution for the asteroid belt, taken from Bottke et al. (2005) with kind permission of the author.

The Kuiper belt has a high number of binary objects. Observations (Noll et al., 2008a,b) indicate that the binary fraction is at about 30 percent for objects larger than 100 km and at low inclinations. Simulations from Nesvorný et al. (2011) show a binary fraction of up to 100 percent are possible for the initial population. They are then presumed to be dynamically disrupted over the time between the Kuiper belt formation and observations.

1.5   Numerical Simulations

I use the PENCIL CODE, a 6th order spatial and 3rd order temporal finite difference code, for my simulations. The code is written in Fortran-90 and uses modules to turn different physics on or off. It makes use of the message passing interface (MPI) that is widely used in many computer clusters. Details on the PENCIL CODE and download information can be found at `http://www.nordita.org/software/pencil-code/`.
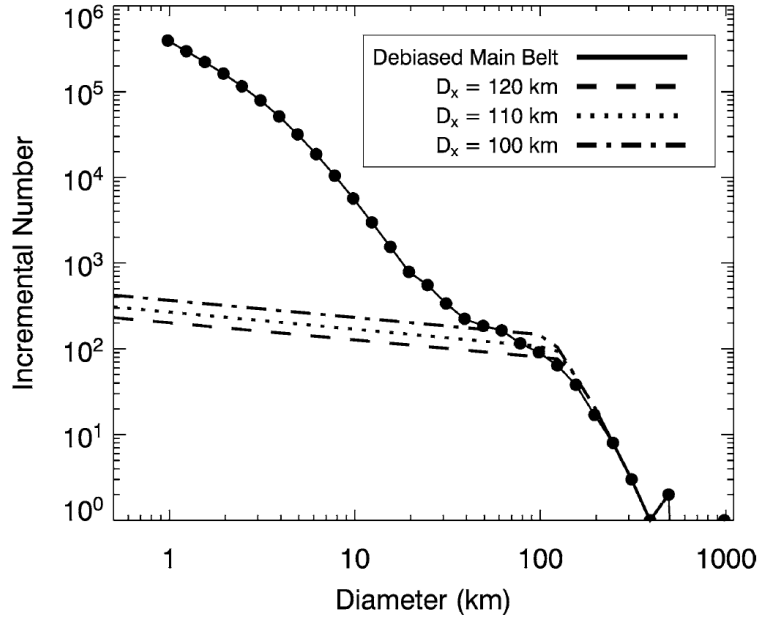
Figure 1.3 The initial main belt size distribution for the remnant population of aster-oids. For $D > 200\,\text{km}$ the size distribution mimics the very few objects of this size currently in the asteroid belt. For $D_x < D < 200\,\text{km}$ the size distribution follows the steep power-law index of -4.5 and for $D < D_x$ the shallow power-law index of -1.2. The de-biased main belt shows the observed size distribution. This figure is taken from Bottke et al. (2005) with kind permission of the author.

1.6   About this Thesis

This thesis is structured as follows: in Chapter 2 I discuss a code verification for Rayleigh-Taylor instability with dust-laden fluids and sedimenting dust clumps in the PENCIL CODE. In Chapter 3 the excitation, size, life-time, and dust concentration abil-ity of zonal flows and the resulting axisymmetric pressure bumps is displayed. This essential part of the thesis if mainly taken from my first paper Dittrich et al. (2013). The 4th Chapter covers high-resolution simulations of zonal flows including back-reaction and self-gravity. Here I show the concentration abilities of the pressure bumps of zonal flows. In Chapter 5 I present the results of collapse-simulations of spherical dust clouds that are or become gravitationally unstable. Finally, the discussion and conclusion of all results are found in Chapter 6.

Chapter 2

Code Verification

2.1 Rayleigh-Taylor Instability

The Rayleigh-Taylor instability (RTI; Rayleigh, 1882; Taylor, 1950) is a standard test for numerical simulations. The standard setup is a two-dimensional simulation with a two-layer incompressible fluid. In the classical RTI without surface tension and viscosity all wave lengths are unstable. The smallest available wave length grows fastest. The smallest available wave length depends on surface tension and viscosity.

In the linear phase of the RTI the growth rate is given by the dispersion relation $\omega^2 = g k_{\mathrm{RT}} \mathcal{A}$, where g is the gravitational acceleration, $k_{\mathrm{RT}} = 2\pi/\lambda_{\mathrm{RT}}$ is the wave number of the smallest available wave length λ_{RT}, and $\mathcal{A} = (\rho_1 - \rho_2)/(\rho_1 + \rho_2)$ is the Atwood number with ρ_1 and ρ_2 being the densities of the upper and lower fluid respectively (Chandarsekhar, 1955). The typical time scale of the RTI is then defined by

$$\tau_{\mathrm{RT}} = \frac{1}{|\omega|} = \sqrt{\frac{\lambda_{\mathrm{RT}}}{2\pi \mathcal{A} g}} . \tag{2.1}$$

2.2 Equations

The gas density is evolved with the continuity equation

$$\frac{\partial \rho}{\partial t} = -(\boldsymbol{u} \cdot \boldsymbol{\nabla}) \rho - \rho \boldsymbol{\nabla} \cdot \boldsymbol{u} + f_D(\rho) , \tag{2.2}$$

where mass diffusion is explicitely ignore. I use an equation of state for an ideal gas $P = c_{\mathrm{s}}^2 \rho \gamma^{-1}$, where c_{s} is the speed of sound and γ is the adiabatic index.

In the simulations I evolve the gas velocity with the following equation of motion

$$\frac{\partial \boldsymbol{u}}{\partial t} = -(\boldsymbol{u} \cdot \boldsymbol{\nabla}) \boldsymbol{u} - \frac{1}{\rho} \boldsymbol{\nabla} P + \boldsymbol{g} - \frac{\epsilon}{\tau_{\mathrm{f}}} \left[\boldsymbol{u}(\boldsymbol{x}^{(i)}) - \boldsymbol{v}^{(i)} \right] + \boldsymbol{f}_\nu(\boldsymbol{u}, \rho) , \tag{2.3}$$

where the terms on the right-hand side are the advection term, the pressure gradient, the gravitational acceleration $\boldsymbol{g} = (0, 0, -g)$, the drag term, and the viscosity term.

9

The latter is discussed in Section 2.2.1. The drag term only acts, if the dust-to-gas ratio $\epsilon = \rho_\mathrm{p}\rho^{-1}$ is larger than 0, i.e., in simulations with particles.

Particles in my simulations represent particle clouds of individual particles of equal size. Particle i has a position $\boldsymbol{x}_i$ and velocity $\boldsymbol{v}_i$ and is evolved with

$$\frac{d\boldsymbol{x}^{(i)}}{dt} = \boldsymbol{v}^{(i)} \tag{2.4}$$

and

$$\frac{d\boldsymbol{v}^{(i)}}{dt} = -\frac{1}{\tau_\mathrm{f}}\left[\boldsymbol{v}^{(i)} - \boldsymbol{u}(\boldsymbol{x}^{(i)})\right] + \boldsymbol{g}\,, \tag{2.5}$$

where the first term represents the gas drag on the particles. The friction time τ_f is a measure for the size of the particles[1]. Particles only interact with each other via gas drag and are otherwise collisionless. The gas velocity at particle location is using the triangular shaped cloud scheme of the PENCIL CODE, where the gas velocity of the surrounding 27 grid cells is taken into account. This gives a much better estimation for the drag force than adopting the gas velocity in the nearest grid cell (Youdin and Johansen, 2007).

2.2.1 Viscosity

The viscosity term is fully expressed by

$$\begin{aligned}
\boldsymbol{f}_\nu &= \nu_1\left[\boldsymbol{\nabla}^2\boldsymbol{u} + \frac{1}{3}\boldsymbol{\nabla}\boldsymbol{\nabla}\cdot\boldsymbol{u} + 2\left(\boldsymbol{S}^{(1)}\cdot\boldsymbol{\nabla}\ln\rho\right)\right] \\
&\quad + \nu_3\left[\boldsymbol{\nabla}^6\boldsymbol{u} + \left(\boldsymbol{S}^{(3)}\cdot\boldsymbol{\nabla}\ln\rho\right)\right] \\
&\quad + \nu_\mathrm{sh}\left[\boldsymbol{\nabla}\boldsymbol{\nabla}\cdot\boldsymbol{u} + (\boldsymbol{\nabla}\cdot\boldsymbol{u})(\boldsymbol{\nabla}\cdot\ln\rho)\right] + (\boldsymbol{\nabla}\nu_\mathrm{sh})\,\boldsymbol{\nabla}\cdot\boldsymbol{u}\,.
\end{aligned} \tag{2.6}$$

The first term is the regular Navier-Stokes viscosity with the constant coefficient ν_1, the second term is the hyper-viscosity with the constant coefficient ν_3, and the last terms are the shock viscosity with a variable coefficient ν_sh.

The traceless first order rate-of-strain tensor $\boldsymbol{S}^{(1)}$ is

$$S_{ij}^{(1)} = \frac{1}{2}\left(\frac{\partial u_i}{\partial x_j} + \frac{\partial u_j}{\partial x_i} - \frac{2}{3}\delta_{ij}\boldsymbol{\nabla}\cdot\boldsymbol{u}\right) \tag{2.7}$$

and the third-order rate-of-strain tensor $\boldsymbol{S}^{(3)}$ is defined by

$$S_{ij}^{(3)} = \frac{\partial^5 u_i}{\partial x_j^5}\,. \tag{2.8}$$

The high-order Laplacian $\boldsymbol{\nabla}^6$ in equation (2.6) is expanded as $\boldsymbol{\nabla}^6 = \partial^6/\partial x^6 + \partial^6/\partial y^6 + \partial^6/\partial z^6$. The shock viscosity is expressed by

$$\nu_\mathrm{sh} = c_\mathrm{sh}\left\langle\max\left[-\boldsymbol{\nabla}\cdot\boldsymbol{u}\right]_+\right\rangle\min\left(\delta x, \delta y, \delta z\right)^2\,. \tag{2.9}$$

---

[1]The conversion from τ_f to a physical size is discussed in Section 3.7.2.

In the fashion of von Neumann and Richtmyer (1950) it is proportional to positive[2] flow convergence (compression). One takes the maximum over five zones, and smooth it to second order. As suggested by von Neumann and Richtmyer (1950), I set the shock viscosity coefficient to $c_{sh} = 1.0$ to dissipate energy in shocks.

2.2.2 Initial Conditions

The fluid at the top has twice the density than one at the bottom. The upper left panel in Figure 2.1 shows the initial condition. The vertical velocity is initialized with a sinusoidal shape

$$u_z(x, t = 0) = u_{z,0} \cos(2\pi x / L_x), \tag{2.10}$$

where $u_{z,0} = 0.79 \tau_{RT} g$ is the amplitude of the vertical velocity and L_x is the box length in x-direction[3].

In the particle simulations I initialize a uniform gas density and fill the upper half of the simulation box with dust particles. The dust-to-gas ratio in the upper half is set to be $\epsilon_0 = 1$. Since the particles are distributed on the grid scale, there are grid cells that already have an initial local dust-to-gas ratio enhancement. I chose tightly coupled particles with a friction time $\tau_f = 0.046 \tau_{RT}$ (and $\tau_f = 0.46 \tau_{RT}$ for comparison). The sinusoidal initial vertical velocity is set to

$$v_z(x^{(i)}, t = 0) = v_{z,0} \cos(2\pi x^{(i)} / L_x), \tag{2.11}$$

where $v_{z,0} = 0.79 \tau_{RT} g$ is the amplitude of the vertical velocity. The random initial velocity is set to a uniform random velocity (Press et al., 1992) in all directions. The amplitude of the random initial velocity is $v_{z,0} = 0.16 \tau_{RT} g$.

All runs in this chapter are summarized in Table 2.1. The simulation box dimension in code units is $L_x = 0.5 l_{code}$, $L_y = 0.5 l_{code}$, $L_z = 1.5 l_{code}$ for all simulations. In the two-dimensional (2D) simulations, the y-direction is simulated as one grid cell. Hence, structure in y-direction is not possible in 2D simulations. In every simulation the gravitational acceleration is $g = 0.1$.

2.2.3 Boundary Conditions

The boundary conditions for these simulations are periodic in x and, if applicable, y direction. In the vertical (z) direction, the boundaries are reflecting for the gas. Particles that cross any vertical boundary leave the simulation and are not considered further.

---

[2]Symbolized by the plus sign in equation (2.9). I only apply shock viscosity where the velocity flow is converging. A positive convergence implies a negative divergence, i.e., compression.

[3]In a box ranging from $-L_x/2$ to $L_x/2$ the maximum positive flow is in the center of the box while the maximum negative flow is at the (periodic) box boundary.

Table 2.1 Run parameters

Run	$N_x \times N_y \times N_z$	ν_1	ν_3	$u_{z,0}$ or $v_{z,0}$	$n_{\text{particles}}$	τ_{f}
(1)	(2)	(3)	(4)	(5)	(6)	(7)
2Dgas	$72 \times 1 \times 216$	8.0×10^{-8}	0	cosine wave: Eq. (2.10)	0	0
3Dgas	$72 \times 72 \times 216$	8.0×10^{-8}	0	cosine wave: Eq. (2.10)	0	0
2Dcos0.01	$72 \times 1 \times 216$	0	1.0×10^{-14}	cosine wave: Eq. (2.11)	311,040	0.01
2Dcos0.1	$72 \times 1 \times 216$	0	1.0×10^{-14}	cosine wave: Eq. (2.11)	311,040	0.1
3Dcos0.01	$72 \times 72 \times 216$	0	1.0×10^{-14}	cosine wave: Eq. (2.11)	22,394,880	0.01
3Dcos0.1	$72 \times 72 \times 216$	0	1.0×10^{-14}	cosine wave: Eq. (2.11)	22,394,880	0.1
2Drnd0.01	$72 \times 1 \times 216$	0	1.0×10^{-14}	random	311,040	0.01
2Drnd0.03	$72 \times 1 \times 216$	0	1.0×10^{-14}	random	311,040	0.03
2Drnd0.1	$72 \times 1 \times 216$	0	1.0×10^{-14}	random	311,040	0.1
2Drnd0.3	$72 \times 1 \times 216$	0	1.0×10^{-14}	random	311,040	0.3
2Drnd1	$72 \times 1 \times 216$	0	1.0×10^{-14}	random	311,040	1
2Drnd0.1HR	$144 \times 1 \times 432$	0	3.0×10^{-16}	random	1,244,160	0.1
2Drndall	$72 \times 1 \times 216$	0	1.0×10^{-14}	random	1,555,200	$0.01, 0.03, 0.1, 0.3, 1$
3Drnd0.01	$72 \times 72 \times 216$	0	1.0×10^{-14}	random	22,394,880	0.01
3Drnd0.1	$72 \times 72 \times 216$	0	1.0×10^{-14}	random	22,394,880	0.1
3Drnd1	$72 \times 72 \times 216$	0	1.0×10^{-14}	random	22,394,880	1
3Drndall	$72 \times 72 \times 216$	0	1.0×10^{-14}	random	111,974,400	$0.01, 0.03, 0.1, 0.3, 1$

Notes. Column (1): name of run. Column (2): grid resolution. Column (3-4): dissipation coefficients. Column (5): initial velocity perturbation. Column (6): number of particles in simulation. Column (7) friction time in code units t_{code}.

2.3   Results

2.3.1   Classical Rayleigh-Taylor Instability

In this section, I study the results of the 2D simulations in x and z. The classical RTI with two layers of fluid is shown in Figure 2.1 from run *2Dgas*.

Vertical gravity is acting on the fluid and it starts to mix. The fluids on the sides are moving with opposing velocities, triggering a Kelvin-Helmholtz instability (KHI) on both sides. The typical RTI mushroom forms (third panel in Figure 2.1). This creates new small regions similar to the initial condition that become unstable themselves. The last panel in Figure 2.1 shows the instability at an advanced stage. At this point the time step of the simulation becomes very short and the simulation is aborted. Run *3Dgas* is not shown here, because the structures formed are the same. This is due to the axisymmetric initial condition in y.

In a classical RTI, the gas velocity can be expected to grow with

$$u_{\text{max}}(t) = u_{\text{max},0} e^{t/\tau_{\text{RT}}} ,\tag{2.12}$$

where $u_{\text{max},0}$ is the proportionality factor. Using the analytical expression in equation (2.1) with $\lambda_{\text{RT}} = 2 * L_x = l_{\text{code}}$ I calculate $\tau_{\text{RT}} = 2.185 t_{\text{code}}$. Figure 2.2 shows the measured evolution of $u_{\text{max}}(t)$ for three runs with a sinusoidal vertical velocity initialization and the analytical prediction from equation (2.12). In the linear growth phase (up to $\sim 2\tau_{\text{RT}}$) the slopes agree quite well. This comparison shows that the simulated linear growth phase of the RTI can be explained with the analytical prediction for $u_{\text{max}}(t)$ using the analytically predicted τ_{RT}.
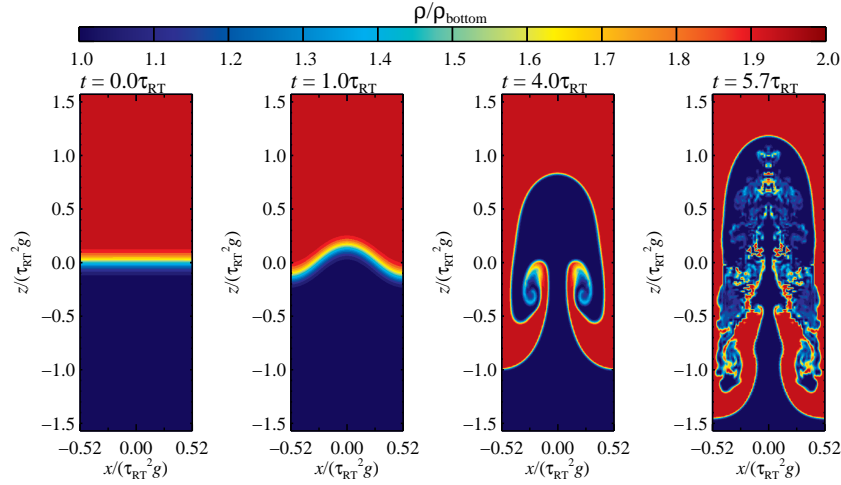
Figure 2.1 Snapshots of a classical Rayleigh-Taylor instability (RTI), run *2Dgas*. The upper fluid has a density $\rho_1 = 2\rho_2$ and the initial fluid velocity has a sinusoidal shape (equation (2.10)) pointing upwards in the simulation center. The linear RTI develops at $t = 1\tau_{RT}$. The snapshot at $t = 4\tau_{RT}$ shows the typical RTI mushroom that develops because of a Kelvin-Helmholtz instability (KHI) on the sides. Smaller versions of the RTI and the KHI develop and create a very speckled density structure. The time step of the simulation becomes very short after $t = 5.7\tau_{RT}$ and the simulation is aborted. Run *3Dgas* has exactly the same appearance, since the velocity perturbation is only dependent on x.
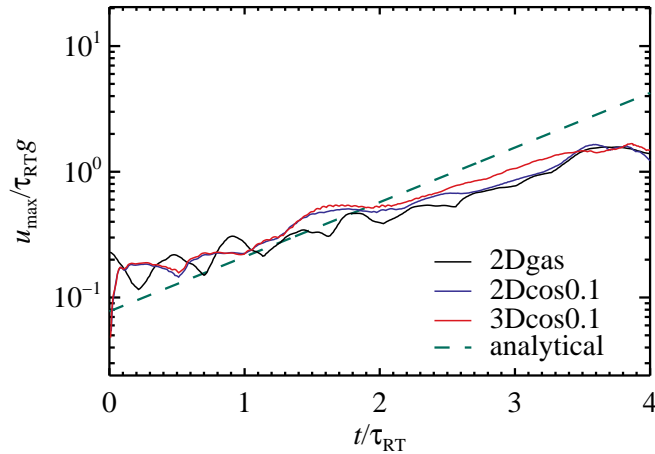
Figure 2.2 The measured and analytical (using equation (2.12)) evolution for the maximum gas velocity u_{max} in the simulations with a cosine initial velocity. The curves agree well and show that the Rayleigh-Taylor instability is nicely simulated with the PENCIL CODE.

2.3.2   Rayleigh-Taylor Instability with Dust-laden Fluids

As a code verification I use a dust-laden fluid that has a total density of $\rho_p + \rho = 2\rho$ to create the high-density upper region. Figures 2.3 and 2.4 show snapshots of the
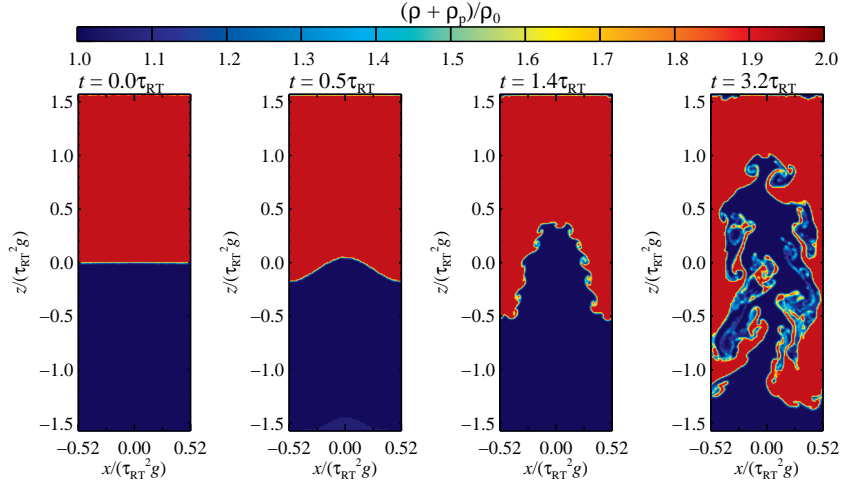
Figure 2.3 Snapshots of a dust-laden fluid simulation (run *2Dcos0.01*) with acting Rayleigh-Taylor instability (RTI). The panels show the initial evolution of the RTI. The fluid density is uniform initially; the upper half of the simulation box is dust-laden with a local dust-to-gas ratio of $\epsilon_0 = 1$ of dust particles with the friction time $\tau_f = 0.046\tau_{RT}$. The gas and the dust particles have an initial sinusoidal vertical velocity and react to a vertical gravity. A shape similar to the classical RTI develops. Additionally to the small-scale RTI and Kelvin-Helmholtz instabilities, the streaming instability increases the dust density locally.
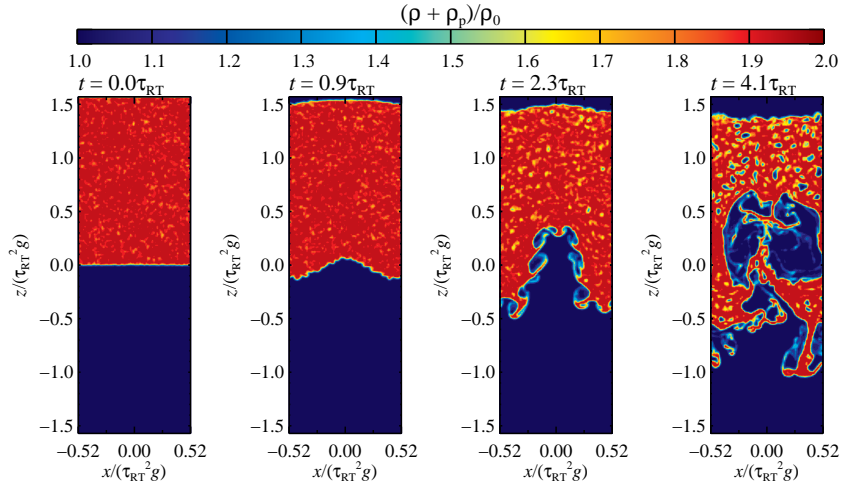
Figure 2.4 Snapshots of a dust-laden fluid simulation (run *2Dcos0.1*), similar to the one in Figure 2.3. Here, particles with $\tau_f = 0.46\tau_{RT} = 0.1t_{code}$ are simulated. The panels show the initial evolution of the Rayleigh-Taylor instability (RTI). The time scales of the RTI in runs *2Dcos0.01* and *2Dcos0.1* are different. The dust density enhancement due to the streaming instability is stronger.

combined dust particle and gas density in runs *2Dcos0.01* and *2Dcos0.1*, respectively. The shapes that develop are initially very similar to those with a two-layer fluid (run *2Dgas*, Figure 2.1). At later times they deviate more because the dust particles

are not incompressible. Also, the time scales at which the RTI acts is different. At later times, both dust particles simulations develop densities that are higher than the initial density maximum.

This test shows that a dust-laden fluid undergoes a RTI and that the PENCIL CODE is able to simulate the linear growth sufficiently, although the time scales are different.

2.3.3   Sedimenting Dust Clump

Two-dimensional simulations
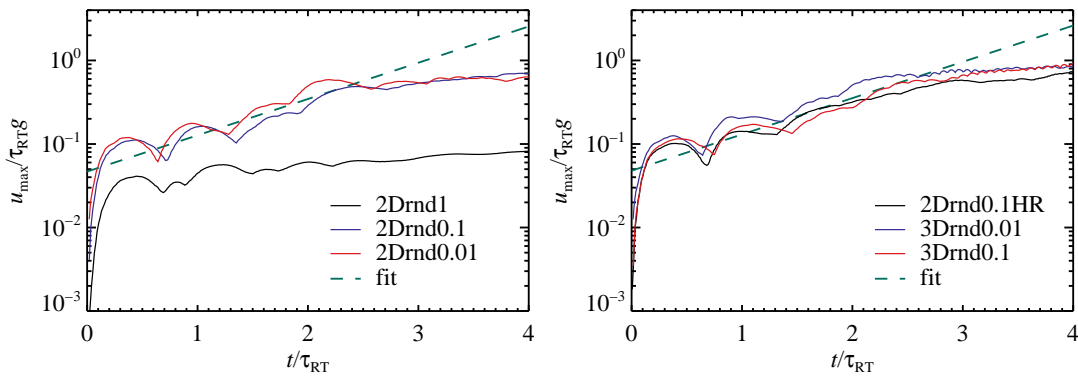
Figure 2.5 Both panels show the measured evolution of u_{max} of different simulations. The shown fit in the left panel is averaged for runs *2Drnd0.1* and *2Drnd0.01* while the fit in the right panel is averaged for all shown runs. These figures illustrate how I measured the Rayleigh-Taylor time scale τ_{RT} in my simulations with random initial velocities. The fits use $u_{fit} = a \exp\left(t/\tau_{RT}\right)$ (after equation (2.12)) to measure τ_{RT}. All measured time scales are summarized in Table 2.2.

In order to scale my simulations, I need to determine the Rayleigh-Taylor time scale τ_{RT}. I measured them using equation (2.12). This procedure is illustrated in Figure 2.5 for some simulations. The evolution of u_{max} shows that τ_{RT} does not depend on the particle size if $\tau_f < t_{code}$. It is also independent of resolution and whether the simulation is 2D or 3D. The difference in the measured τ_{RT} for these simulations is smaller than their uncertainty.

A sedimenting dust clump in a protoplanetary disk will form RTI structures as shown in the test of the previous chapter. I use the same setup of a dust-laden fluid. The initial velocity however is random instead of a sinusoidal shape. As the particles are being pulled down they form finger-like structures (compare Figures 2.6–2.8). These structures are observed in many astronomical objects, such as the Crab nebula (Hester et al., 1996) and can be explained with a form of the Rayleigh-Taylor instability (Hillier et al., 2012). I performed simulations with particles of different friction times τ_f to compare their reaction on the gas. The friction times used are $\tau_f = \{0.0038, 0.012, 0.038, 0.12, 0.380\} \tau_{RT}$[4]; see Table 2.2 for more information.

---

[4]Note that the Rayleigh-Taylor time scale is different to the previous used one, because the wavelength of the perturbation has changed.
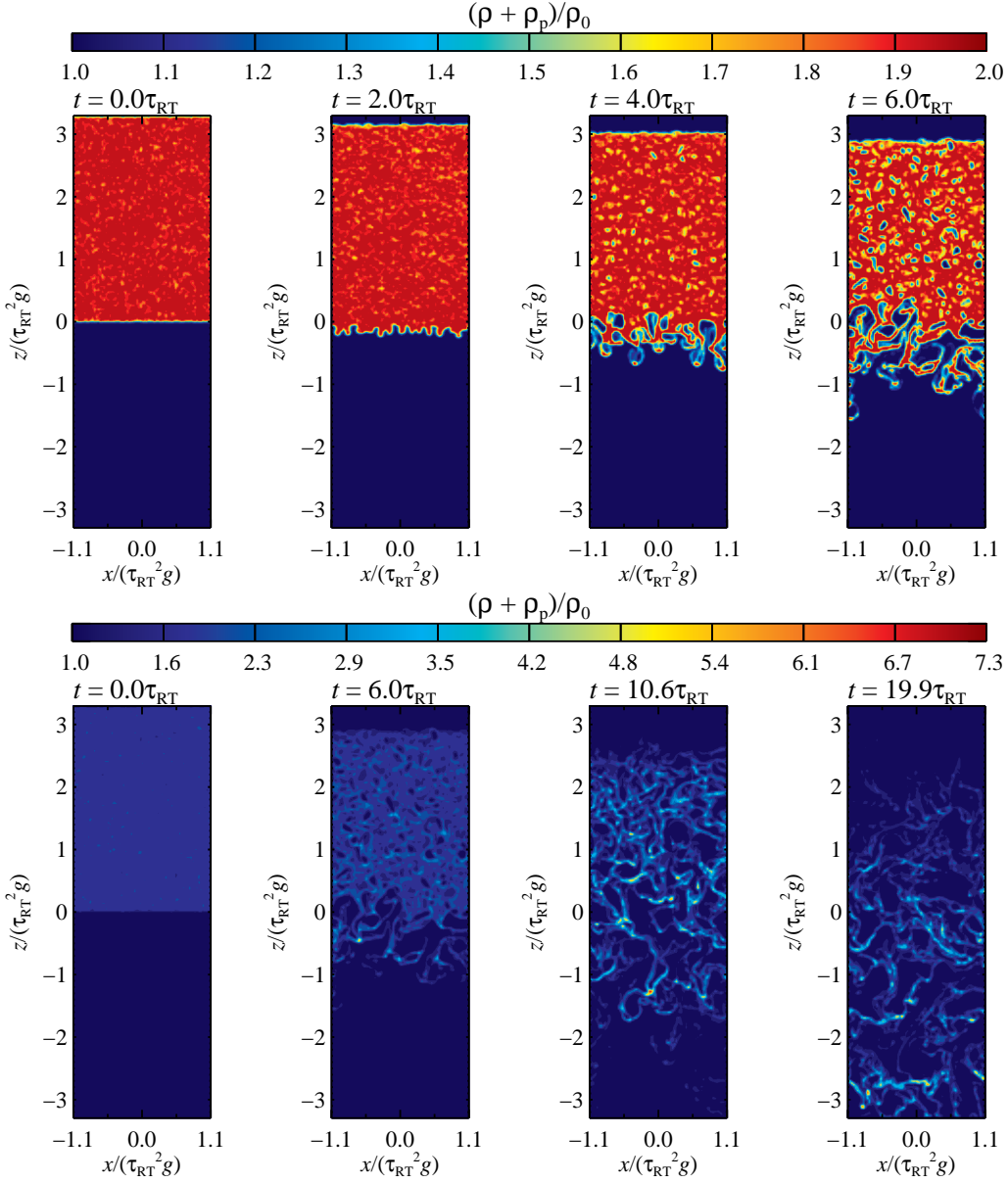
Figure 2.6 Snapshots of a sedimenting dust clump simulation, run *2Drnd0.1*. The particles in this simulation have a friction time of $\tau_f = 0.066\tau_{RT} = 0.1t_{code}$ The upper panel shows the initial evolution of the Rayleigh-Taylor instability (RTI). The lower panel shows the non-linear development in a different color scale. After $2\tau_{RT}$, finger-like structures appear. The structures at late simulation times are similar to the structures in run *2Dcos0.1*.

For comparison, I show only two simulations (runs *2Drnd0.1* and *2Drnd0.1HR*) with a monodisperse particle size distribution. In Figure 2.6 I show snapshots of run *2Drnd0.1* with particles that have the same friction time τ_f in code units as the particles in run *2Dcos0.1* (Figure 2.4). The Rayleigh-Taylor time scale τ_{RT} is shorter due to the smaller instability scales in code units. Thus, in run *2Drnd0.1*, τ_f in physical
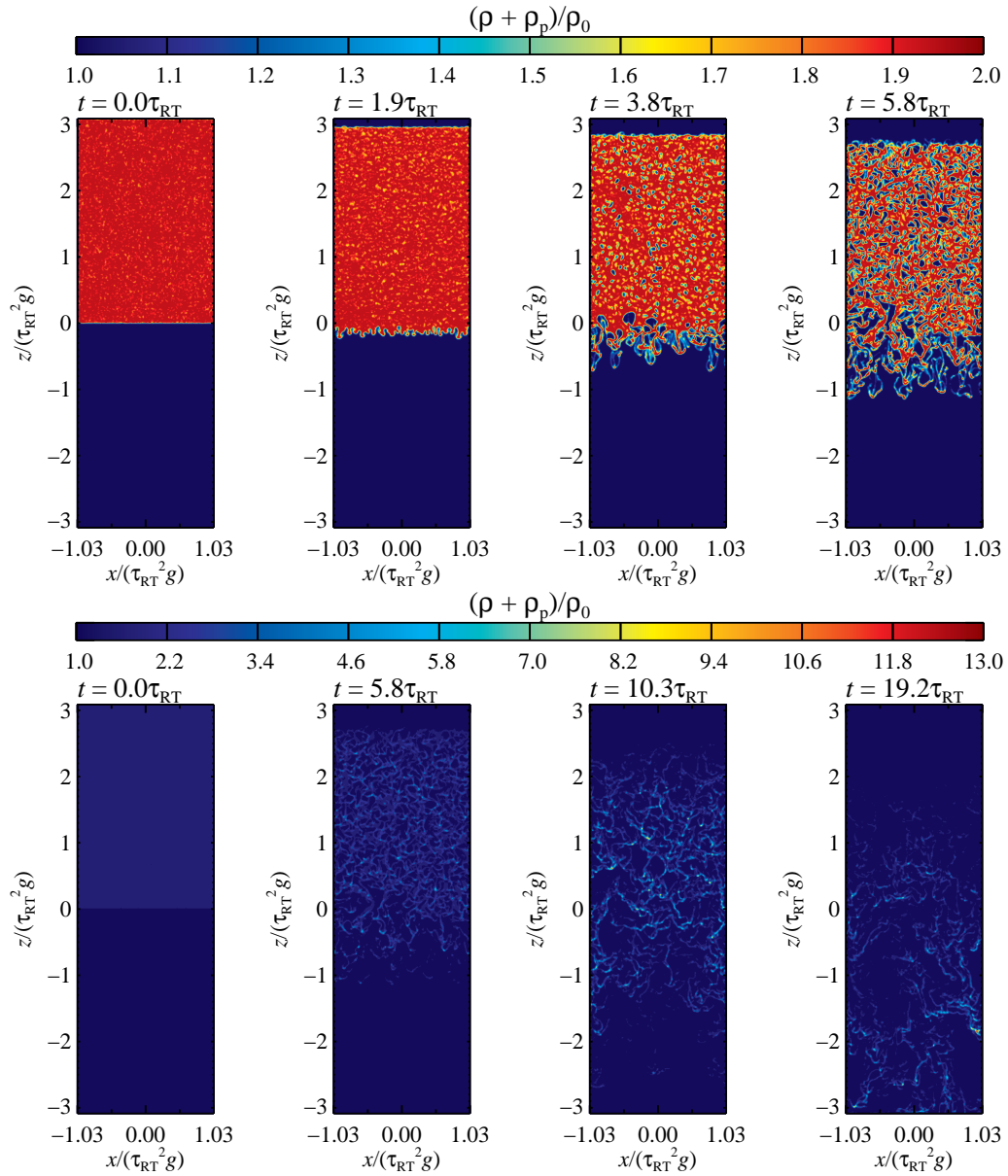
Figure 2.7 Snapshots of a sedimenting dust clump simulation at high resolution, run *2Drnd0.1HR*. The snapshots were taken at the same times in code units as for run *2Drnd0.1* in Figure 2.6. The friction time for the particles in this simulation is $\tau_f = 0.064\tau_{RT} = 0.1t_{code}$. The higher resolution run shows that the size of the Rayleigh-Taylor instability fingers depends on the resolution of the simulation grid (see second panel in the upper row). At late times (lower panels) the streaming instability creates higher over-densities than at lower resolution (compare with Figure 2.6).

units differs to the one in run *2Dcos0.1* as does the physical length scale.

The high resolution run *2Drnd0.1HR* in Figure 2.7 shows that the size of the RTI fingers depends very much on resolution. Their real size might still be smaller. To deduce their real size one has to do a resolution study on sedimenting dust clumps.

The size of the RTI fingers does not depend on the size of the particles in my simula-
tions. Maybe that changes when the resolution is sufficient. The late-time evolution of
run *2Drnd0.1HR* shows that the streaming instability density enhancements depend
on resolution as well (see also Johansen et al., 2012, for the same observation).
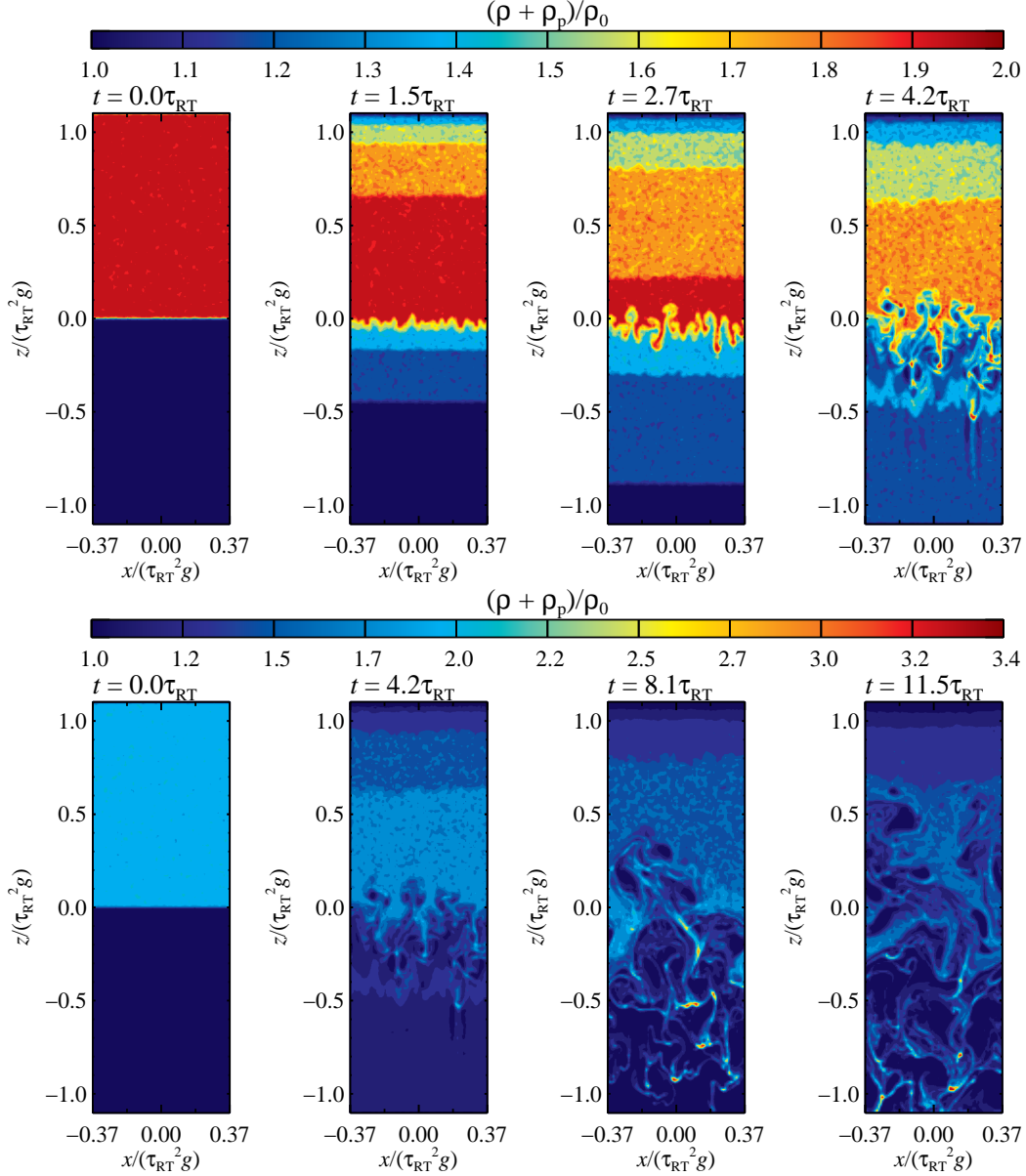
Figure 2.8 Snapshots of a sedimenting dust clump simulation with a poly-
disperse size distribution of particles.   The used friction times are $\tau_f =$
$\{0.0038, 0.012, 0.038, 0.12, 0.38\}\tau_{RT}$. The upper panel shows the initial evolution of the
Rayleigh-Taylor instability (RTI). The lower panel shows the non-linear development
in a different color scale. Even in a setup with particles of different sizes, the Rayleigh-
Taylor fingers are clearly visible in the upper row. The lower panels show the over-
densities in this simulation. The over-densities are quantitatively lower than before,
because every particle species has only a 5th of the dust density.

The snapshots in Figure 2.8 show run *2Drndall* with all five particle species. Particles with the longest friction time quickly fall through the simulation box, leaving those with shorter friction times behind. At $t = 1.5\tau_{RT}$ and $t = 2.7\tau_{RT}$ Rayleigh-Taylor fingers are clearly visible. At late simulation times, the streaming instability creates over-densities. The latter is not as effective, because the dust-to-gas ratio is effectively decreased for each particle species, since the initial dust-to-gas ratio $\epsilon_0 = 1$ is shared by 5 different size bins.

Table 2.2 Results

Run	τ_{RT}	τ_f	α_{mix}
(1)	(2)	(3)	(4)
2Dgas	2.2	0	0.096
3Dgas	2.2	0	0.096
2Dcos0.01	2.2	0.046	0.63
2Dcos0.1	2.2	0.46	0.29
3Dcos0.01	2.2	0.046	0.73
3Dcos0.1	2.2	0.46	0.28
2Drnd0.01	1.6	0.0063	0.075
2Drnd0.03	1.6	0.019	0.076
2Drnd0.1	1.5	0.066	0.071
2Drnd0.3	2.0	0.15	0.099
2Drnd1	2.0	0.50	0.00052
2Drnd0.1HR	1.6	0.064	0.084
2Drndall	2.6	0.0038, 0.012, 0.038, 0.12, 0.38	-
3Drnd0.01	1.6	0.0064	0.085
3Drnd0.1	1.5	0.069	0.063
3Drnd1	2.2	0.45	0.00038
3Drndall	2.4	0.0041, 0.012, 0.041, 0.12, 0.41	-

Notes. Column (1): name of run. Column (2): Rayleigh-Taylor time scale in units of code time t_{code}. Column (3): friction time in units of τ_{RT}. Column(4): mixing length scaling parameter.

Three-dimensional simulations

The three-dimensional structure of run *3Drnd0.1* at $t = 7.9\tau_{RT}$ is shown in Figures 2.9 and 2.10. A volume rendered iso-surface at $\rho_p = 0.5\rho_0$ is shown in Figure 2.9. The structures appear isotropic and homogeneous. This is also displayed in Figure 2.10. The cuts in the $x - z$-plane and the $y - z$-plane show that the wavelength of structures at the interface is the same in both planes.

This isotropy and homogeneity show that the PENCIL CODE is able to qualitatively simulate the RTI fingers properly. This enables a comparison with experiments to study the RTI fingers quantitatively.

$$\tau_{\mathrm{f}} = 0.069\tau_{\mathrm{RT}} \qquad\qquad t = 3.4\tau_{\mathrm{RT}}$$
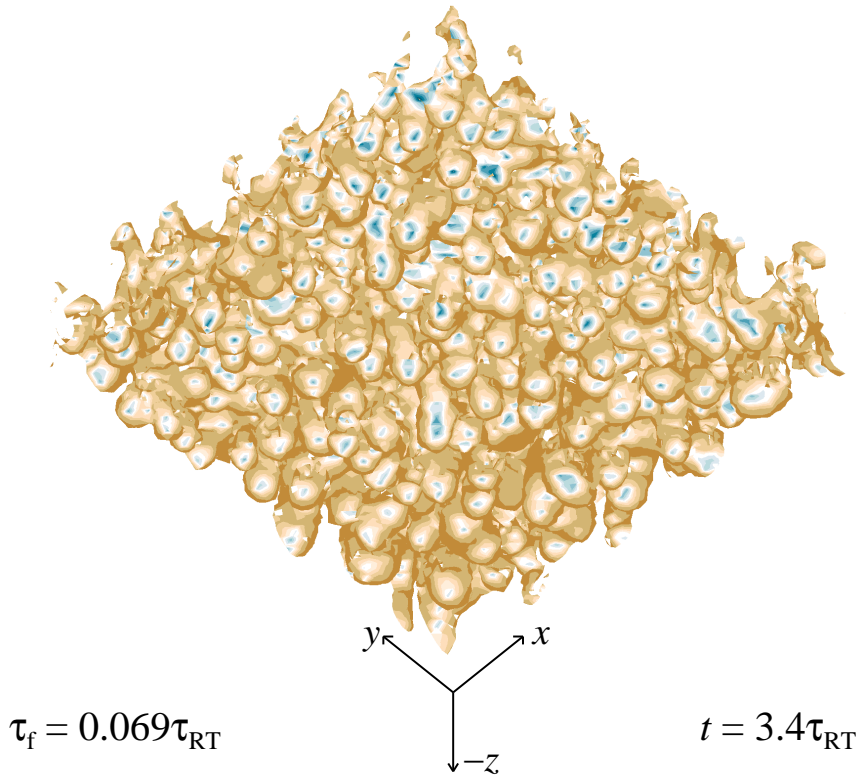
Figure 2.9 This volume-rendered snapshot from run *3Drnd0.1* was taken after $t = 3.4\tau_{\mathrm{RT}}$. It shows the iso-surface at a volume density of $\rho_p = 0.5\rho_0$. The view is from the bottom and inclined for better visibility. The structures appear homogeneous and isotropic.
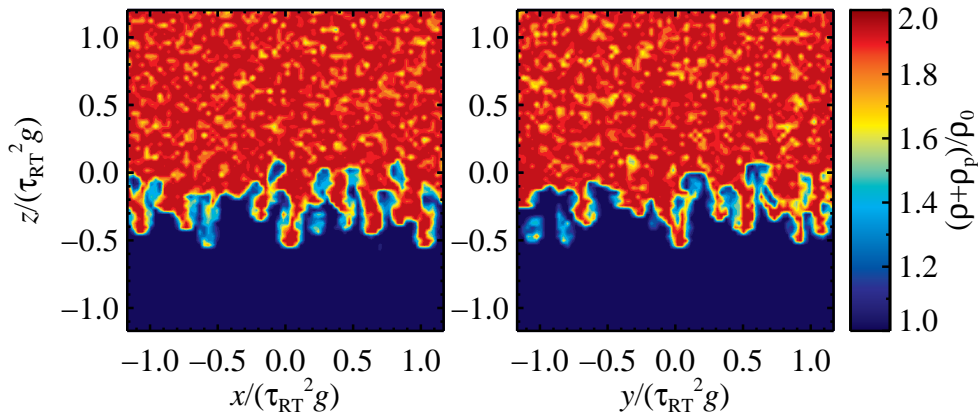
Figure 2.10 These panels show a cut at the simulation center of run *3Drnd0.1* after $t = 3.4\tau_{\mathrm{RT}}$. The left panel is a cut in the $x - z$-plane, the right panel shows a cut in the $y - z$-plane. Both panels only show the region around the interface between dust-laden fluid and dust-free fluid in the x-direction. The size of the structures is the same in both planes.

2.3.4 Mixing lengths

The mixing length h_{mix} in a RTI (Fermi and von Neumann, 1953) can be described by

$$\frac{\mathrm{d}h_{\mathrm{mix}}}{\mathrm{d}t} = 2\sqrt{\alpha_{\mathrm{mix}}\mathcal{A}gh_{\mathrm{mix}}}\,, \tag{2.13}$$

where α_{mix} is a dimensionless scaling parameter. Equation 2.13 can be derived from an energy argument (Cook et al., 2004). The solution to equation (2.13) is

$$h_{\mathrm{mix}}(t) = \alpha_{\mathrm{mix}}\mathcal{A}gt^2 + 2\sqrt{\alpha_{\mathrm{mix}}\mathcal{A}gh_{\mathrm{mix},0}}\cdot t + h_{\mathrm{mix},0}\,, \tag{2.14}$$

where $h_{\mathrm{mix},0} = h_{\mathrm{mix}}(t=0)$. The mixing length can be measured in my simulations and used to determine α_{mix}. Figure 2.11 shows the evolution of the mixing length in several simulations. Experiments and simulations (Youngs, 1984) report $\alpha_{\mathrm{mix}} \sim 0.04\ldots0.077$. My values for α_{mix} are summarized in Table 2.2. They have, with some exceptions, the same order of magnitude.
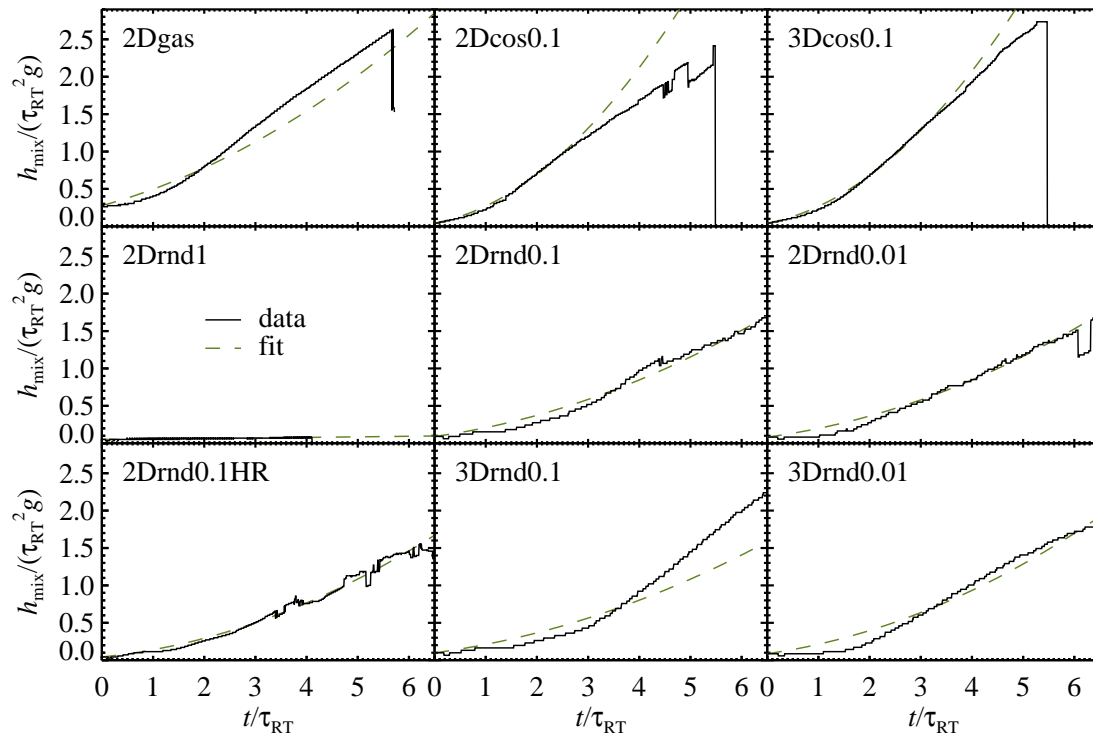
Figure 2.11 Evolution of the mixing lengths in several simulations are shown in solid black lines. The fits to the data are performed by using equation (2.14). The analytical shape of $h_{\mathrm{mix}}(t)$ describes the measured mixing length during the linear growth phase. At later times, the measured h_{mix} deviates from the expected behavior.

Chapter 3

Zonal Flows: Pressure Bumps, Particle Concentrations, and Collisions

This chapter describes the main part of my work. I measure zonal flow length and time scales and show particle capture by the resulting axisymmetric pressure bump. I compare results of different-sized local simulations with global simulations. I also alter the particle size to study their individual behavior.

This chapter is composed of my paper (Dittrich et al., 2013) and a draft for a paper about the corresponding collision velocities.

3.1 Magneto-Hydro -Dynamical Simulations

I simulate the standard ideal MHD equations in a local shearing box with vertical stratification. The simulation boxes are centered at an arbitrary distance R to the star. The radial direction is denoted by x, the azimuthal direction by y, and the vertical direction by z. The Keplerian frequency is Ω. I include dust particle dynamics, without back-reaction to the gas and without self-gravity. The dynamic equations for the gas phase and the magnetic fields are described in Section 3.1.1. The dust particle dynamics is laid out in Section 3.1.5.

3.1.1 MHD Equations

The gas velocity $\boldsymbol{u}$ relative to the Keplerian shear is evolved via the equation of motion

$$
\frac{\partial \boldsymbol{u}}{\partial t} + (\boldsymbol{u} \cdot \boldsymbol{\nabla}) \boldsymbol{u} + u_y^{(0)} \frac{\partial \boldsymbol{u}}{\partial y} = 2\Omega u_y \hat{\boldsymbol{x}} - \frac{1}{2}\Omega u_x \hat{\boldsymbol{y}} + \Omega^2 z \hat{\boldsymbol{z}}
$$

$$
+ \frac{1}{\rho} \boldsymbol{J} \times \boldsymbol{B} - \frac{1}{\rho} \boldsymbol{\nabla} P + \boldsymbol{f}_\nu (\boldsymbol{u}, \rho) . \tag{3.1}
$$

On the left-hand side of the equation the second and third term are the advection terms by the perturbed velocity and by shear flow respectively. The right-hand side contains the Coriolis force, the vertical component of the stellar gravity, the Lorentz force, the pressure gradient, and the viscosity term. Here $u_y^{(0)} = -(3/2)\Omega x$ is the Keplerian orbital velocity. The magnetic field B as well as the current density J are calculated from the vector potential A using $B = \nabla \times A$ and $J = \mu_0^{-1}\nabla \times (\nabla \times A)$ respectively. Here, μ_0 is the vacuum permeability. The viscosity term f_ν is explained in Section 3.1.2.

The magnetic potential is evolved with the uncurled induction equation

$$\frac{\partial A}{\partial t} + u_y^{(0)}\frac{\partial A}{\partial y} = u \times B + \frac{3}{2}\Omega A_y \hat{x} + f_\eta\left(A\right) . \tag{3.2}$$

The terms on the right-hand side express the electromotive force, the stretching (creation of azimuthal magnetic field from radial field) by Keplerian shear and the resistivity f_η (see Section 3.1.2).

The gas density is evolved with the continuity equation

$$\frac{\partial \rho}{\partial t} + (u \cdot \nabla)\rho + u_y^{(0)}\frac{\partial \rho}{\partial y} = -\rho\nabla \cdot u + f_D\left(\rho\right) , \tag{3.3}$$

where the last term on the right-hand side describes mass diffusion (see Section 3.1.2). The simulations use an isothermal equation of state $P = c_s^2\rho$, where the speed of sound is $c_s = H\Omega$; H is the gas pressure scale height.

3.1.2 Dissipation

Maxwell and Reynolds stresses as well as the MRI release kinetic and magnetic energy at large scales. This energy cascades down to small scales. Since numerical simulations have a finite resolution, this small-scale energy needs to be dissipated. Numerical dissipation is used in form of hyper- and shock viscosity, hyper-resistivity, and hyper- and shock diffusion.

Viscosity

The viscosity term f_ν in equation (3.1) is expressed by

$$\begin{aligned}
f_\nu &= \nu_3\left[\nabla^6 u + \left(S^{(3)} \cdot \nabla\ln\rho\right)\right] \\
&\quad + \nu_{\mathrm{sh}}\left[\nabla\nabla \cdot u + (\nabla \cdot u)\left(\nabla \cdot \ln\rho\right)\right] + (\nabla\nu_{\mathrm{sh}})\nabla \cdot u .
\end{aligned} \tag{3.4}$$

I restricted my models to hyper- (ν_3) and shock (ν_{sh}) viscosity. Thus, the regular Navier-Stokes viscosity term is neglected. The third-order rate-of-strain tensor $S^{(3)}$ is defined by

$$S_{ij}^{(3)} = \frac{\partial^5 u_i}{\partial x_j^5} . \tag{3.5}$$

The high-order Laplacian ∇^6 in equation (3.4) is expanded as $\nabla^6 = \partial^6/\partial x^6 + \partial^6/\partial y^6 + \partial^6/\partial z^6$. Furthermore, the shock viscosity is expressed by

$$\nu_{\text{sh}} = c_{\text{sh}} \langle \max\left[-\nabla \cdot \boldsymbol{u} \right]_+ \rangle \min\left(\delta x, \delta y, \delta z \right)^2 . \tag{3.6}$$

In the fashion of von Neumann and Richtmyer (1950) it is proportional to positive[1] flow convergence (compression). One takes the maximum over five zones, and smoothed it to the second order. As suggested by von Neumann and Richtmyer (1950), I set the shock viscosity coefficient to $c_{\text{sh}} = 1.0$ to dissipate energy in shocks at high z above the mid-plane of the disk.

Resitivity

The effects of resistivity are captured by the term

$$\boldsymbol{f}_\eta = \eta_3 \nabla^6 \boldsymbol{A} , \tag{3.7}$$

where η_3 is the hyper-resistivity.

Diffusion

Mass diffusion is computed with

$$f_D = D_3 \nabla^6 \rho + D_{\text{sh}} \nabla^2 \rho + \nabla D_{\text{sh}} \cdot \nabla \rho , \tag{3.8}$$

where D_3 is the hyper-diffusion parameter and D_{sh} is expanded as in equation (3.6).

3.1.3 Boundary Conditions

The simulations use shearing box boundary conditions in radial (shear-periodic) and azimuthal (periodic) directions. The vertical direction also has periodic boundary conditions. Although periodic boundary conditions in vertical direction are not physical, these boundary conditions conserve the average flux of the magnetic field. A simulation with outflow boundaries showed no considerable mass flux across the vertical boundary and did not change the average properties of the zonal flow.

3.1.4 Dimensions

I use the dimensionless unit system $c_{\text{s}} = \Omega = \mu_0 = \rho_0 = 1$. Velocity is measured in units of the local sound speed c_{s}. Gas velocities are always denoted by $\boldsymbol{u}$ whereas particle velocities are always denoted by $\boldsymbol{v}$. All velocities are differences to the Keplerian orbital velocity $\boldsymbol{v}_K = (0, u_y^{(0)}, 0)$, where $u_y^{(0)} = -(3/2)\Omega x$. Time is measured in units

---

[1]Symbolized by the plus sign in equation (3.6). I only apply shock viscosity where the velocity flow is converging. A positive convergence implies a negative divergence, i.e., compression.

of the local orbital time $T_{\mathrm{orb}} = 2\pi\Omega^{-1}$. Length measures are in units of the pressure scale height $H = c_{\mathrm{s}}\Omega^{-1}$. Density is stated in units of the initial mid-plane gas density ρ_0. Magnetic field strength is measured in units of $c_{\mathrm{s}}(\mu_0\rho_0)^{-1}$. Energy and stress are in units of the mean thermal pressure in the box $\langle P \rangle = c_{\mathrm{s}}^2\langle\rho\rangle$.

Since my simulations are dimensionless, they can be placed at any distance R to the star. Only by defining a global pressure gradient $\partial P_{global}/\partial R$, which balances the Coriolis force in

$$\frac{1}{\rho}\frac{\partial P_{\mathrm{global}}}{\partial R} = 2\Omega\Delta v_{\mathrm{p}}\,, \tag{3.9}$$

I restrict my simulations to a specific distance to the star where the chosen pressure gradient applies. The parameter $\Delta v_{\mathrm{p}} = u_y^{(0)} - u_y$ is the difference to the azimuthal Keplerian velocity. I fix $\Delta v_{\mathrm{p}} = 0.05c_{\mathrm{s}}$ (see also Section 3.1.6). Numerically, the global pressure gradient acts as an external force on gas and dust.

3.1.5   Particles in MHD Simulations

Dust particles are simulated as individual super-particles i with position x_i and velocity v_i. Each super-particle position is evolved with

$$\frac{d\boldsymbol{x}^{(i)}}{dt} = \boldsymbol{v}^{(i)} + u_y^{(0)}\hat{\boldsymbol{y}}\,. \tag{3.10}$$

The change of velocity for each particle is evolved through

$$\frac{d\boldsymbol{v}^{(i)}}{dt} = 2\Omega v_y^{(i)}\hat{\boldsymbol{x}} - \frac{1}{2}\Omega v_x^{(i)}\hat{\boldsymbol{y}} - \Omega^2 z\hat{\boldsymbol{z}} - \frac{1}{\tau_{\mathrm{f}}}\left[\boldsymbol{v}^{(i)} - \boldsymbol{u}(\boldsymbol{x}^{(i)})\right]\,, \tag{3.11}$$

where the first and second terms are due to the Coriolis force. The third term corresponds to the vertical gravity of the star. Particles only feel the gas drag (last term in equation 3.11) of nearby cells, but are not subjected to pressure or Lorentz forces. τ_{f} denotes the friction time, a measure for the size of the particles.

3.1.6   Initial Conditions

The gas density is set to an isothermal hydrostatic equilibrium $\rho(z) = \rho_0 \exp\left(-z^2/2H^2\right)$. I start with random noise fluctuations in the gas velocity with $\delta u = 10^{-3}c_{\mathrm{s}}$. The azimuthal component of the magnetic vector potential is initialized with $A_y = A_0 \cos(k_x x)\cos(k_y y)\cos(k_z z)$ where throughout $k_x = k_y = k_z = 4.76H^{-1}$ and $A_0 = 0.04c_{\mathrm{s}}(\mu_0\rho_0)^{-1}$.

Particles are released after the gas turbulence is saturated, after $20T_{\mathrm{orb}}$ for the largest runs. For convenience, I used the same saturation time for all my simulations. Particles have a Stokes number of $\mathrm{St} = \tau_{\mathrm{f}}\Omega = 1$, unless otherwise stated. The initial particle distribution is Gaussian in z and uniform in x and y. The particle velocity is initialized with the stationary solution (Nakagawa et al., 1986) for the radial and

azimuthal velocity

$$\frac{v}{c_s} = -\left(\frac{2\Delta v_p}{\tau_f\Omega + (\tau_f\Omega)^{-1}}, \frac{\Delta v_p}{1 + (\tau_f\Omega)^2}, 0\right).$$

(3.12)

One gets Δv_p from the solution of equation (3.9)

$$\frac{\Delta v_p}{c_s} = -\frac{1}{2}\left(\frac{H}{r}\right)^2 \frac{\partial \ln P}{\partial \ln R}.$$

(3.13)

I initialized $\Delta v_p = 0.05c_s$ for my simulations.

Simulation Parameters
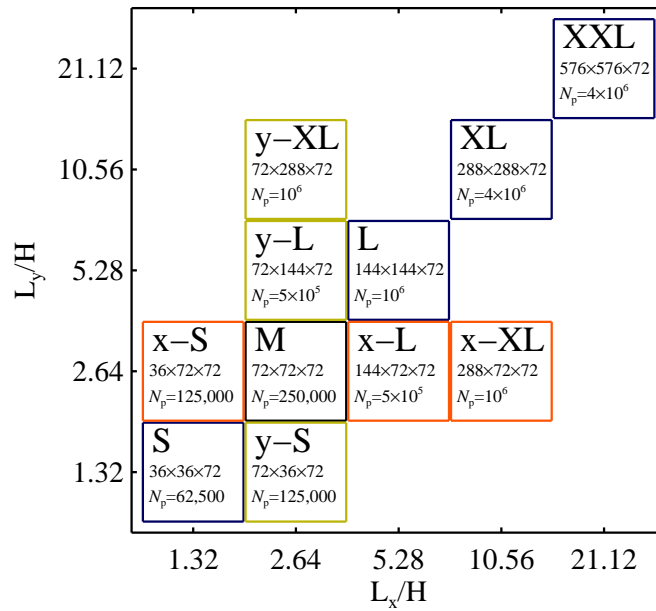
Figure 3.1 Parameter space of radial and azimuthal box sizes that was simulated for this work. Every simulation has a vertical extent of 2.64H. The first line in each box states the name of the run, the second line the number of grid cells used and the third line gives the number of simulated super-particles. More details on all simulations are found in Table 3.1.

The parameter space covered by my simulations is summarized in Figure 3.1. The vertical extent is always set to $L_z = 2.64H$.[2] One simulation set (A) covers the boxes with a squared base, i.e., radial and azimuthal extent are kept the same: $L_x = L_y = \{1.32, 2.64, 5.28, 10.56, 21.12\} H$. These are marked with blue boxes in Figure 3.1 and are called runs S, M, L, XL, and XXL. The deviation to the global density profile in the largest box can be quite severe at the inner and outer boundary of the largest simulation. Thus, the results from run XXL have to

---

[2]$L = 1.32$ has been chosen as the basic box size, because $L_x = 1.32$ approximately marks the transition from subsonic to supersonic Keplerian shear flow (Johansen et al., 2009a).

Table 3.1 Run parameters

Simulation Set (1)	Run (2)	$L_x \times L_y \times L_z$ (3)	$N_x \times N_y \times N_z$ (4)	$\nu_3 = \eta_3 = D_3$ (5)	$n_{\text{particles}}$ (6)	St (7)	Shear (8)	Δt (9)
A	S	$1.32 \times 1.32 \times 2.64$	$36 \times 36 \times 72$	4.0×10^{-10}	62,500	1.0	FDA	121
A,B,C	M	$2.64 \times 2.64 \times 2.64$	$72 \times 72 \times 72$	4.0×10^{-10}	250,000	1.0	FDA	121
A,E	L	$5.28 \times 5.28 \times 2.64$	$144 \times 144 \times 72$	4.0×10^{-10}	1,000,000	1.0	FDA	121
A,E	XL	$10.56 \times 10.56 \times 2.64$	$288 \times 288 \times 72$	4.0×10^{-10}	4,000,000	1.0	FDA	121
A	XXL	$21.12 \times 21.12 \times 2.64$	$576 \times 576 \times 72$	4.0×10^{-10}	4,000,000	1.0	FDA	121
B	x-S	$1.32 \times 2.64 \times 2.64$	$36 \times 72 \times 72$	4.0×10^{-10}	125,000	1.0	FDA	121
B	x-L	$5.28 \times 2.64 \times 2.64$	$144 \times 72 \times 72$	4.0×10^{-10}	500,000	1.0	FDA	121
B	x-XL	$10.56 \times 2.64 \times 2.64$	$288 \times 72 \times 72$	4.0×10^{-10}	1,000,000	1.0	FDA	121
C	y-S	$2.64 \times 1.32 \times 2.64$	$72 \times 36 \times 72$	4.0×10^{-10}	125,000	1.0	FDA	121
C	y-L	$2.64 \times 5.28 \times 2.64$	$72 \times 144 \times 72$	4.0×10^{-10}	500,000	1.0	FDA	121
C	y-XL	$2.64 \times 10.56 \times 2.64$	$72 \times 288 \times 72$	4.0×10^{-10}	1,000,000	1.0	FDA	121
D	LspecMR	$5.28 \times 5.28 \times 2.64$	$144 \times 144 \times 72$	4.0×10^{-10}	1,200,000	$0.01 \dots 100$	FDA	121
D	LspecHR	$5.28 \times 5.28 \times 2.64$	$256 \times 256 \times 128$	2.0×10^{-11}	120,000,000	$0.01 \dots 100$	FDA	121
D	LspecMRs	$5.28 \times 5.28 \times 2.64$	$144 \times 144 \times 72$	4.0×10^{-10}	14,000,000	$0.01 \dots 1.0$	FDA	121
D	MspecMRb	$2.64 \times 2.64 \times 2.64$	$72 \times 72 \times 72$	4.0×10^{-10}	6,000,000	$1.0 \dots 100$	FDA	223
E	L_SAFI	$5.28 \times 5.28 \times 2.64$	$144 \times 144 \times 72$	4.0×10^{-10}	1,000,000	1.0	SAFI	121
E	XL_SAFI	$10.56 \times 10.56 \times 2.64$	$288 \times 288 \times 72$	4.0×10^{-10}	4,000,000	1.0	SAFI	121

Notes. Column (1): Simulation set. Column (2): name of run. Column (3): box size in units of pressure scale heights. Column (4): grid resolution. Column (5): dissipation coefficients. Column (6): number of particles in simulation. Column (7): Stokes number $\text{St} = \tau_f \Omega$. Column (8): shear advection scheme. Column (9): total run time in orbits T_{orb}.

be treated with caution. Another set of simulations (*B*) varies the radial size of the box, $L_x = \{1.32, 2.64, 5.28, 10.56\}\, H$, with constant box size in azimuthal direction, $L_y = 2.64H$. This set is marked red in Figure 3.1 and includes runs *x-S*, *M*, *x-L*, and *x-XL*. The third set of simulations (*C*) varies the azimuthal extent, $L_y = \{1.32, 2.64, 5.28, 10.56\}\, H$, while the radial extent is kept constant, $L_x = 2.64H$. This set includes runs *y-S*, *M*, *y-L*, and *y-XL* (marked yellow in Figure 3.1). All simulations are stratified and have dust particles with different couplings to the gas. The simulations displayed in Figure 3.1 have particles with a Stokes number of $\text{St} = 1$.

Details on run parameters of those and six more simulations are found in Table 3.1. The first set of simulations (*A,B* and *C*) in Table 3.1 are the simulations with medium resolution, i.e., 36 grid cells[3] per 1.32 pressure scale heights. Simulation set *D* was carried out to investigate the behavior of different particle sizes in the presence of zonal flows. Run *LspecMR* is very much like run *L*, but with 12 different particle Stokes numbers. The run *LspecHR* has a resolution of 64 grid cells per 1.32*H*. Runs *LspecMR* and *LspecHR* have 12 different particle species, with Stokes numbers of $\text{St} = 0.01 \dots 100.0$. The runs *LspecMRs* and *MspecMRb* have particles with Stokes numbers of $\text{St} = 0.01 \dots 1.0$ and $\text{St} = 1.0 \dots 100.0$, respectively. These two simulations were carried out to study particle behavior with more particles per grid cell[4] at medium resolution. The corresponding sizes for different protoplanetary disk models are found in Section 3.7.2.

Simulation set *E* is a comparison of runs *L* and *XL* to the same runs (*L_SAFI* and

---

[3]I chose 36 grid cells instead of the usual 32 grid cells. That choice was done due to the architecture (12 CPUs per node) of the used cluster, THEO in the MPG computing center in Garching.

[4]~ 9 and ~ 16 particles per grid cell for runs *LspecMRs* and *MspecMRb* compared to ~ 0.8 particles per grid cell for run *LspecMR*.

XL_SAFI) with the Shear Advection by Fourier Interpolation (SAFI) scheme. Here, all variables $q(x, y, z)$ are transformed into Fourier space in the y-direction to get $\hat{q}(x, k_y, z)$. Then each Fourier mode is multiplied by $\exp\left[ik_y u_y^{(0)}(x)\delta t\right]$ to shift by $u_y^{(0)}(x)\delta t$ in real space and is inverse Fourier transformed to real space. This method reduces the advection error to the standard Finite Difference Advection (FDA) scheme in the PENCIL CODE (more details on FDA and SAFI are found in Johansen et al., 2009a).

Every simulation is run for 121 local orbits $T_{\mathrm{orb}} = 2\pi\Omega^{-1}$, except for *LspecMRb* which runs for $223 T_{\mathrm{orb}}$ in order to follow the evolution of the slowly settling large particles. After $20 T_{\mathrm{orb}}$, when the initial conditions are sufficiently forgotten and the turbulence saturated, the particles are started.

3.2 Excitation of Zonal Flows and Long-lived Axisymmetric Pressure Bumps

The origin of zonal flows is not yet fully understood, but a good idea on how they might form is presented in Johansen et al. (2009a). The argumentation goes as follows: Large scale fluctuations in the radial component of the magnetic field, B_x^2, are excited through non-linear turbulent terms. The radial magnetic field component is stretched with the Kepler-rotation and in turn excites large-scale fluctuations in the Maxwell stress, $-B_x B_y$. These fluctuations lead to a differential transport of momentum which separate the orbital flow into regions of faster and slower rotation. This may even increase the gas velocities to super-Keplerian speeds. These regions of increased and decreased azimuthal gas velocity are called zonal flows. They are long lived, on the order of tens of orbits (Dittrich et al., 2013; Johansen et al., 2009a). A simplified version of the dynamic equations can be used to get a model of the excitation of zonal flows. From the equation of motion I can obtain the geostrophic balance

$$0 = 2\Omega\hat{u}_y - \frac{c_s^2}{\rho_0}ik_0\hat{\rho} \tag{3.14}$$

and

$$\frac{\mathrm{d}\hat{u}_y}{\mathrm{d}t} = -\frac{1}{2}\Omega\hat{u}_x + \hat{T}. \tag{3.15}$$

In these equations $\hat{\rho}$, $\hat{u}_x$, and $\hat{u}_y$ are the Fourier transformed mass density and velocity components of the gas, k_0 is the largest mode in radial direction, ρ_0 is the initial mid-plane density, and $\hat{T}$ is the non-linear large scale magnetic tension. The continuity equation is simplified to

$$\frac{\mathrm{d}\hat{\rho}}{\mathrm{d}t} = -ik_0\rho_0\hat{u}_x - \frac{\hat{\rho}}{\tau_{\mathrm{mix}}}, \tag{3.16}$$

where $\hat{\rho}/\tau_{\mathrm{mix}}$ is the turbulent mass density diffusion with mixing time-scale τ_{mix}.

The equations (3.14)–(3.16) can be combined into a single evolution equation for the gas density,

$$\frac{\mathrm{d}\hat{\rho}}{\mathrm{d}t} = c_k\left(\hat{F} - \frac{\hat{\rho}(t)}{\tau_{\mathrm{mix}}}\right), \tag{3.17}$$
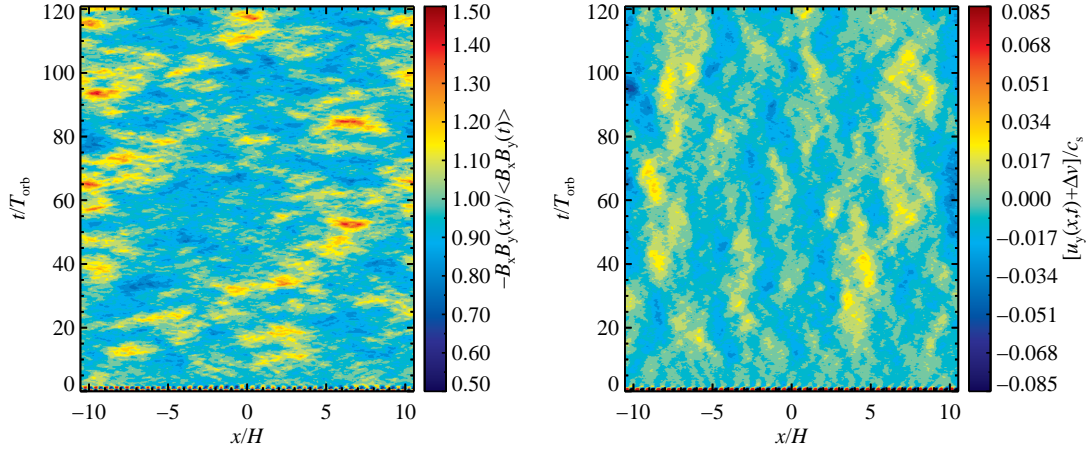
Figure 3.2 The left panel shows the evolution of the Maxwell stress in radial direction, while the right panel shows the evolution of the azimuthal gas velocity in radial direction. Both show the largest run *XXL*. Maxima in the azimuthal velocity appear when the Maxwell stress gives kicks to the gas. They have a phase shift of 90 degrees to each other (see also Johansen et al., 2009a). Also the Maxwell stress extrema have much shorter life-times than the gas velocity extrema. This shows that large scale magnetic fields give short uncorrelated kicks to the gas which stays in longer-lived stable arrangement and diffuses slowly.

where $c_{\mathrm{k}} = (1 + k_0^2 H^2)^{-1}$ is a pressure correction for small-scale modes and $\hat{F} = -2ik_0\rho_0\hat{T}/\Omega$ is the forcing term. The pressure correction decreases the amplitude of the forcing and also increases the effective damping time for small-scale modes. In Figure 3.2, the life-times and radial positions of the Maxwell stress are compared to those of the azimuthal gas velocity. The Maxwell stress gives short, uncorrelated kicks to the gas velocity and hence also to the gas density. The forcing time-scale τ_{for} of $\hat{F}$ is very short compared to the mixing time-scale τ_{mix}. Hence, equation (3.17) has to be modeled as a stochastic differential equation (Youdin and Lithwick, 2007). The solution, in presence of turbulent diffusion, tends to

$$\frac{\hat{\rho}_{\mathrm{eq}}}{\rho_0} = 2\sqrt{c_{\mathrm{k}}\tau_{\mathrm{for}}\tau_{\mathrm{mix}}}Hk_0\frac{\hat{T}}{c_{\mathrm{s}}} . \tag{3.18}$$

The correlation time of these zonal flows (see Section 3.3) are equal to the mixing time-scales, as predicted by the model. It further predicts that the density modes of $\hat{\rho}_{\mathrm{eq}}$ are proportional to k^{-2} for high modes $k_0H \gg 1$. The clearly sinusoidal shape in all zonal flow plots (see next section) is in very good agreement with that prediction

3.3   Dependence of Zonal Flows on Physical Simulation Box Size

Turbulence properties are summarized in Table 3.2. The kinetic and magnetic energy as well as the Reynolds and Maxwell stress almost doubles when increasing the box

Table 3.2 Turbulence properties

Run	$\langle\frac{1}{2}u_x^2\rangle$	$\langle\frac{1}{2}u_y^2\rangle$	$\langle\frac{1}{2}u_z^2\rangle$	$\langle\frac{1}{2}B_x^2\rangle$	$\langle\frac{1}{2}B_y^2\rangle$	$\langle\frac{1}{2}B_z^2\rangle$	$\langle\rho u_x u_y\rangle$	$\langle -B_x B_y\rangle$	α
(1)	(2)	(3)	(4)	(5)	(6)	(7)	(8)	(9)	(10)
S	2.1×10^{-3}	3.3×10^{-3}	1.5×10^{-3}	8.8×10^{-4}	6.4×10^{-3}	3.5×10^{-4}	7.7×10^{-4}	3.4×10^{-3}	2.8×10^{-3}
M	3.9×10^{-3}	5.2×10^{-3}	2.2×10^{-3}	1.9×10^{-3}	1.2×10^{-2}	7.6×10^{-4}	1.6×10^{-3}	6.6×10^{-3}	5.5×10^{-3}
L	5.0×10^{-3}	5.6×10^{-3}	2.3×10^{-3}	2.0×10^{-3}	8.0×10^{-4}	8.0×10^{-4}	1.9×10^{-3}	6.9×10^{-3}	5.9×10^{-3}
XL	5.2×10^{-3}	5.0×10^{-3}	2.1×10^{-3}	1.7×10^{-3}	1.1×10^{-2}	6.7×10^{-4}	1.8×10^{-3}	6.1×10^{-3}	5.2×10^{-3}
XXL	5.1×10^{-3}	4.6×10^{-3}	2.0×10^{-3}	1.6×10^{-3}	1.0×10^{-2}	6.2×10^{-4}	1.7×10^{-3}	5.7×10^{-3}	4.9×10^{-3}
x-S	4.0×10^{-3}	5.2×10^{-3}	2.4×10^{-3}	2.0×10^{-3}	1.3×10^{-2}	8.4×10^{-4}	1.7×10^{-3}	7.0×10^{-3}	5.8×10^{-3}
x-L	3.8×10^{-3}	5.2×10^{-3}	2.1×10^{-3}	1.7×10^{-3}	1.1×10^{-2}	6.9×10^{-4}	1.5×10^{-3}	6.1×10^{-3}	5.1×10^{-3}
x-XL	3.8×10^{-3}	5.0×10^{-3}	2.2×10^{-3}	1.8×10^{-3}	1.2×10^{-2}	7.1×10^{-4}	1.5×10^{-3}	6.2×10^{-3}	5.2×10^{-3}
y-S	2.3×10^{-3}	3.7×10^{-3}	1.6×10^{-3}	1.0×10^{-3}	7.1×10^{-3}	4.1×10^{-4}	8.6×10^{-4}	3.8×10^{-3}	3.1×10^{-3}
y-L	5.2×10^{-3}	5.7×10^{-3}	2.5×10^{-3}	2.2×10^{-3}	1.4×10^{-2}	8.8×10^{-4}	2.0×10^{-3}	7.5×10^{-3}	6.3×10^{-3}
y-XL	5.4×10^{-3}	5.0×10^{-3}	2.2×10^{-3}	1.8×10^{-3}	1.2×10^{-2}	7.2×10^{-4}	1.9×10^{-3}	6.4×10^{-3}	5.6×10^{-3}
LspecMR	4.8×10^{-3}	5.3×10^{-3}	2.2×10^{-3}	1.9×10^{-3}	1.2×10^{-2}	7.5×10^{-4}	1.8×10^{-3}	6.6×10^{-3}	5.6×10^{-3}
LspecHR	3.0×10^{-3}	4.2×10^{-3}	1.4×10^{-3}	1.3×10^{-3}	7.5×10^{-3}	5.4×10^{-4}	1.0×10^{-3}	4.2×10^{-3}	3.5×10^{-3}
LspecMRs	5.3×10^{-3}	6.2×10^{-3}	2.5×10^{-3}	2.2×10^{-3}	1.4×10^{-2}	9.2×10^{-4}	2.1×10^{-3}	7.7×10^{-3}	6.5×10^{-3}
MspecMRb	4.3×10^{-3}	5.7×10^{-3}	2.5×10^{-3}	2.1×10^{-3}	1.4×10^{-2}	8.7×10^{-4}	1.8×10^{-3}	7.2×10^{-3}	6.0×10^{-3}
L_SAFI	5.1×10^{-3}	5.8×10^{-3}	2.4×10^{-3}	2.1×10^{-3}	1.3×10^{-2}	8.4×10^{-4}	2.0×10^{-3}	7.2×10^{-3}	6.1×10^{-3}
XL_SAFI	5.4×10^{-3}	5.3×10^{-3}	2.2×10^{-3}	1.8×10^{-3}	1.2×10^{-2}	7.3×10^{-4}	1.9×10^{-3}	6.5×10^{-3}	5.6×10^{-3}

Notes. Column (1): name of run. Column (2-4): Kinetic energy. Column (5-7): Magnetic energy. Column (8): Reynolds stress. Column (9): Maxwell stress. Column (10): α-value, following equation (3.19). Stresses and energies have been normalized to the mean thermal pressure in the box, $\langle P\rangle = c_s^2\langle\rho\rangle$.

size from $(1.32H)^2 \times 2.64H$ (run *S*) to $(2.64H)^3$ (run *M*). Further increasing the box size does not change the resulting energies and stresses by much. The radially short box of run *x-S* with $1.32H \times (2.64H)^2$ has similar results on these values. However, the azimuthally short box of run *y-S* has turbulent energies and stresses comparable to run *S*. These measurements show that the turbulence parameters are saturated for boxes with an azimuthal extent of at least $2.64H$. This confirms the results from Fromang and Stone (2009) who found that the turbulence properties do not change when the box size is increased radially, if the azimuthal dimension is large enough. The α-value (Shakura and Sunyaev, 1973) in column (10) in Table 3.2 is calculated via

$$\alpha = \frac{2}{3}\frac{\left(\langle\rho u_x u_y\rangle - \langle B_x B_y\rangle\right)}{\langle P\rangle}, \tag{3.19}$$

where $\langle P\rangle = c_s^2\langle\rho\rangle$. The factor of 2/3 originates from the shear parameter $q = -d\ln\Omega/d\ln R$. I use $q = 3/2$, appropriate for a Keplerian disk. For further details see Brandenburg et al. (1995, page 748). The Maxwell stress is around 3 times higher than the Reynolds stress and thus dominates the α-value.

In order to verify that my numerical resolution is sufficient, I examined the quality factor as described in Simon et al. (2012):

$$Q_j = \frac{\overline{2\pi|v_{a,j}|}}{\Omega\Delta x_j}, \tag{3.20}$$

where the Alfven speed is defined as $|v_{a,j}|^2 = \langle B_j\rangle^2/\langle\rho\rangle$. The notation $\langle x\rangle$ denotes volume averaging, $\overline{x}$ shows a time average. Sorathia et al. (2012) show that $Q_z \gtrsim 10 - 15$ for poorly resolved azimuthal quality factors ($Q_y \sim 10$) is required to resolve the MRI. Larger values of the azimuthal quality factor ($Q_y \gtrsim 25$) allows for lower vertical quality factors. The azimuthal component of the magnetic field is very well

resolved ($Q_y \gtrsim 25$) for all simulations, but runs S and y-S. The vertical component has values between 6 and 8. I thus conclude that all simulations, but runs S and y-S have sufficient resolution for the MRI.

Table 3.3 Zonal flow properties

Run (1)	ρ_{rms} (2)	$\lvert\hat{\rho}(k_x=1)\rvert$ (3)	$\lvert\hat{\rho}(k_x=2)\rvert$ (4)	$\lvert\hat{\rho}(k_x=3)\rvert$ (5)	$\lvert\hat{\tilde{u}}_y(k_x=1)\rvert$ (6)	$\lvert\hat{\tilde{u}}_y(k_x=2)\rvert$ (7)	$\lvert\hat{\tilde{u}}_y(k_x=3)\rvert$ (8)	τ_{corr} (9)
S	6.1×10^{-3}	4.1×10^{-3}	7.5×10^{-4}	4.0×10^{-4}	9.9×10^{-3}	3.4×10^{-3}	2.1×10^{-3}	7.6
M	2.0×10^{-2}	1.0×10^{-2}	2.5×10^{-3}	1.6×10^{-3}	1.2×10^{-2}	5.2×10^{-3}	3.1×10^{-3}	11.2
L	3.9×10^{-2}	2.1×10^{-2}	5.6×10^{-3}	3.2×10^{-3}	1.3×10^{-2}	6.5×10^{-3}	3.7×10^{-3}	23.2
XL	4.3×10^{-2}	1.5×10^{-2}	1.1×10^{-2}	5.0×10^{-3}	4.6×10^{-3}	6.6×10^{-3}	4.3×10^{-3}	43.2
XXL	4.0×10^{-2}	5.0×10^{-3}	7.9×10^{-3}	7.9×10^{-3}	7.8×10^{-4}	2.4×10^{-3}	3.5×10^{-3}	47.3
x-S	1.6×10^{-2}	3.9×10^{-3}	1.7×10^{-3}	1.2×10^{-3}	8.0×10^{-3}	3.2×10^{-3}	2.0×10^{-3}	4.4
x-L	3.3×10^{-2}	2.3×10^{-2}	7.3×10^{-3}	2.7×10^{-3}	1.4×10^{-2}	8.8×10^{-3}	4.7×10^{-3}	37.6
x-XL	2.7×10^{-2}	1.2×10^{-2}	1.0×10^{-2}	6.4×10^{-3}	3.5×10^{-3}	6.2×10^{-3}	5.6×10^{-3}	20.2
y-S	1.2×10^{-2}	9.9×10^{-3}	2.4×10^{-3}	1.1×10^{-3}	1.2×10^{-2}	5.9×10^{-3}	4.1×10^{-3}	14.4
y-L	3.0×10^{-2}	6.9×10^{-3}	3.8×10^{-3}	3.1×10^{-3}	7.8×10^{-3}	3.7×10^{-3}	2.3×10^{-3}	10.8
y-XL	3.6×10^{-2}	5.6×10^{-3}	4.1×10^{-3}	3.3×10^{-3}	5.7×10^{-3}	2.6×10^{-3}	1.6×10^{-3}	10.3
LspecMR	3.7×10^{-2}	1.8×10^{-2}	5.5×10^{-3}	3.1×10^{-3}	1.1×10^{-2}	6.1×10^{-3}	3.6×10^{-3}	21.8
LspecHR	4.2×10^{-2}	9.8×10^{-3}	3.2×10^{-3}	2.0×10^{-3}	5.8×10^{-3}	3.6×10^{-3}	2.0×10^{-3}	23.4
LspecMRs	4.3×10^{-2}	2.4×10^{-2}	5.4×10^{-3}	3.2×10^{-3}	1.4×10^{-2}	6.1×10^{-3}	3.9×10^{-3}	10.9
MspecMRb	1.9×10^{-2}	8.6×10^{-3}	2.6×10^{-3}	1.6×10^{-3}	1.0×10^{-2}	5.3×10^{-3}	3.1×10^{-3}	26.4
L_SAFI	3.9×10^{-2}	2.1×10^{-2}	5.3×10^{-3}	3.2×10^{-3}	1.2×10^{-2}	6.1×10^{-3}	3.9×10^{-3}	25.6
XL_SAFI	4.8×10^{-2}	2.4×10^{-2}	1.0×10^{-2}	5.4×10^{-3}	7.0×10^{-3}	6.2×10^{-3}	4.8×10^{-3}	48.6

Notes. Column (1): name of run. Column (2): root mean square density $\rho_{rms} = \sqrt{\langle (\rho - \overline{\rho})^2 \rangle}$. Column (3-5): Fourier amplitude of radial density modes $k_x = 1 \ldots 3$, normalized by mean density in the box. Column (6-8): Fourier amplitude of azimuthal velocity modes $k_x = 1 \ldots 3$ with $\tilde{u}_y = u_y - \overline{u}_y$. Column (9): correlation time, in orbits $T = 2\pi\Omega^{-1}$, of the largest radial density mode.

In Figure 3.3 a snapshot of the runs y-XL, XL, M, and x-XL are shown in scale, giving a real size comparison of high and low pressure regions. The large-scale sinusoidal form of the dominant mode is observable in these plots. The higher modes are much shorter lived and seem to be non-axisymmetric density waves affected by the shear (Heinemann and Papaloizou, 2009). The amplitudes of the pressure differences are higher in azimuthally large boxes. Only the axisymmetric density waves are long lived and strong enough to make up a significant contribution to the pressure bump structure in an azimuthal as well as a temporal average over some local orbits. The azimuthal average of Figure 3.3 is seen in Figure 3.4. Here, the axisymmetric structure is clearly visible and a strong correlation between the particle location and a positive radial gradient of the gas density is seen. The black dots in Figures 3.3 and 3.4 show the radial and azimuthal position of every 100th particle. The particles are trapped by the axisymmetric pressure bumps. Also, the shapes of spiral density waves (Heinemann and Papaloizou, 2009) can be seen in the structures. The particle distribution with respect to the gas flow will be discussed in more detail in Section 3.4.1.

All of my simulations show signs of zonal flows. Strength and life time of the zonal flows and the associated pressure bumps differ very much with the physical box size. Space-time plots of all different simulation sizes are shown in Figure 3.5 and the upper left panel of Figure 3.6. The pressure bumps are generally more pronounced in simulations with a larger radial extent. Simulation set A strictly follows this general trend. Pressure bump features grow in strength and life-time with the physical box size, always staying at the largest radial scale. This rule applies to all but the largest runs XL, x-XL, and XXL. There, instead of the formerly predominant $k_x = 1$ ($\omega_x = 2\pi k_x / L_x$ in
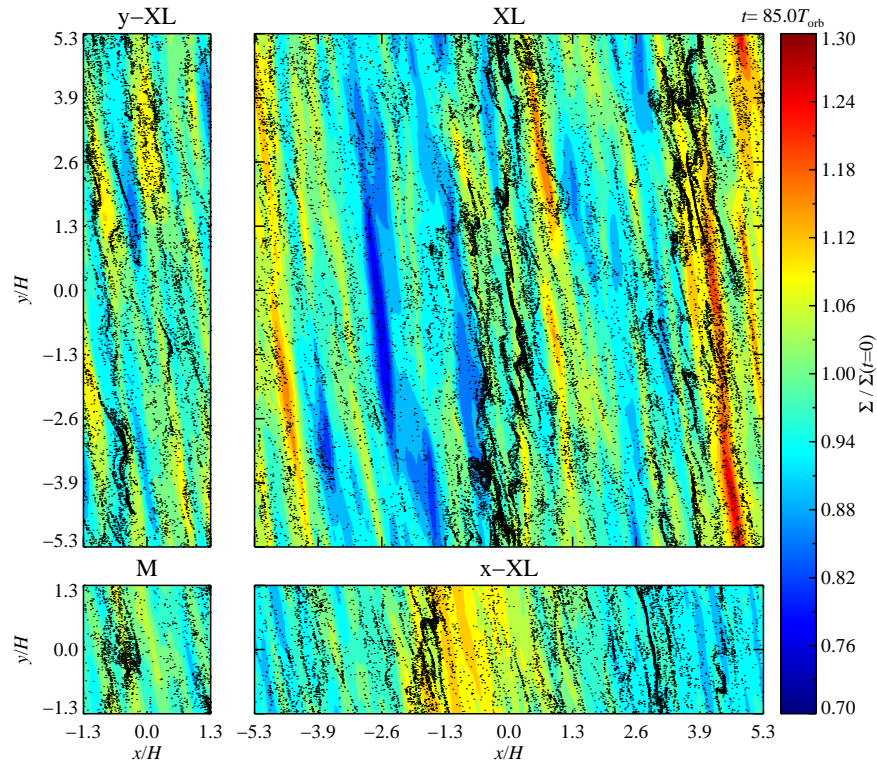
Figure 3.3 Collage of 4 gas surface density representations of the runs *y-XL*, *XL*, *M*, and *x-XL*. Each snapshot was taken after $85T_{\mathrm{orb}}$. These plots show that gas over-densities are most pronounced in the largest box. The non-axisymmetric structures have very short life-times – less than a tenth of an orbit. The pressure bump structures are more visible when the density is averaged over the azimuthal direction (Figure 3.4). The black dots represent the position of every 100th particle, integrated in vertical direction. The particles are trapped both in axisymmetric pressure bumps and in spiral density waves as described in Heinemann and Papaloizou (2009).

Fourier mode $\sin(\omega_x x)$) mode, the mode $k_x = 2$ (higher modes for run *XXL*) is occupied by the pressure bumps. In simulation set *B*, the strength and size of the pressure bumps converges for simulations with a radial extent larger than $5.28H$. The life-time of the pressure bumps even decreases for the largest simulation in this set. Simulation set *C* is qualitatively different from the other simulation sets. Strength, size and life-time of the pressure bumps seem to be inversely proportional to the azimuthal extent of the box, when the vertical and radial box sizes are kept constant. This effect was already seen in, e.g., Simon et al. (2012); Flock et al. (2012). Both groups show that the magnetic field consists of two components: a local turbulent component that is responsible for the zonal flows and a global azimuthal component. Since the total energy stays approximately constant, the local component gets weaker and consequently zonal flows as well as axisymmetric pressure bumps get weaker too.

Figure 3.6 additionally shows space-time plots of the azimuthal gas velocity and the radial gradients of gas density and azimuthal gas velocity of run *XXL*. In the right panels, the position of the highest dust density are shown as dots. Particles get clearly
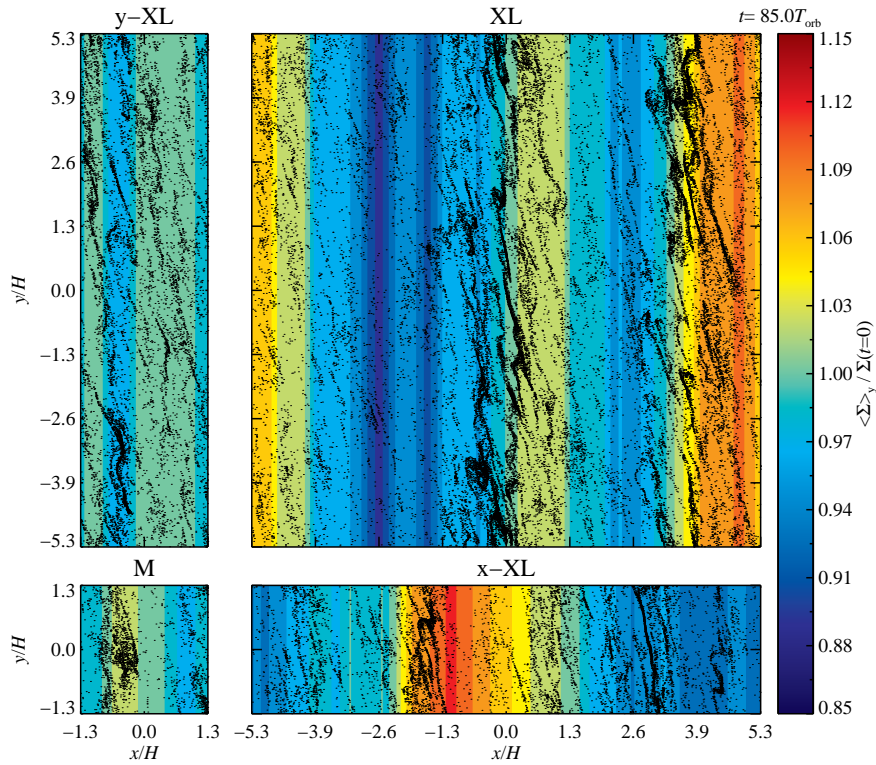
Figure 3.4 Surface density distribution of Figure 3.3, averaged in azimuthal direction and averaged over the mean surface density. This reveals axisymmetric pressure bumps and valleys. Particles are trapped on the inner side of the density maxima, at places with a positive density gradient to overcome the negative global pressure gradient. These pressure bumps are stable for many orbits (compare Figures 3.5 and 3.6).

slowed by the maxima of the azimuthal gas velocity, i.e., the large-scale maxima of the pressure gradients. The velocity has large-scale structures that are very similar to those of the density gradient, as expected in geostrophic balance. Thus, the structure of the velocity gradient can be approximated as the large-scale structure of the second derivative of the gas density. It is shown in the lower right panel that the particles get stopped at the minima of the radial derivative of the azimuthal gas velocity (and thus at minima of the second derivative of the gas density) as analytically predicted (see, e.g., Klahr and Lin, 2001).

I calculated the correlation time of the pressure bumps and the zonal flows in the same way as it was calculated in Johansen et al. (2009a): One uses the density ρ, averaged over azimuthal and vertical directions, at a given time t. Then, one averages over each point in radial direction the time it takes for the density at each point to change by a value corresponding to the standard deviation of the gas density. These measurements are taken for every local orbit. The measurements are averaged over the time between saturation of the turbulence and a time when the correlation does not extend the correlation time to the final time of the simulation. Finally, the averages are multiplied by two, in order to cover the full temporal extent of the correlated
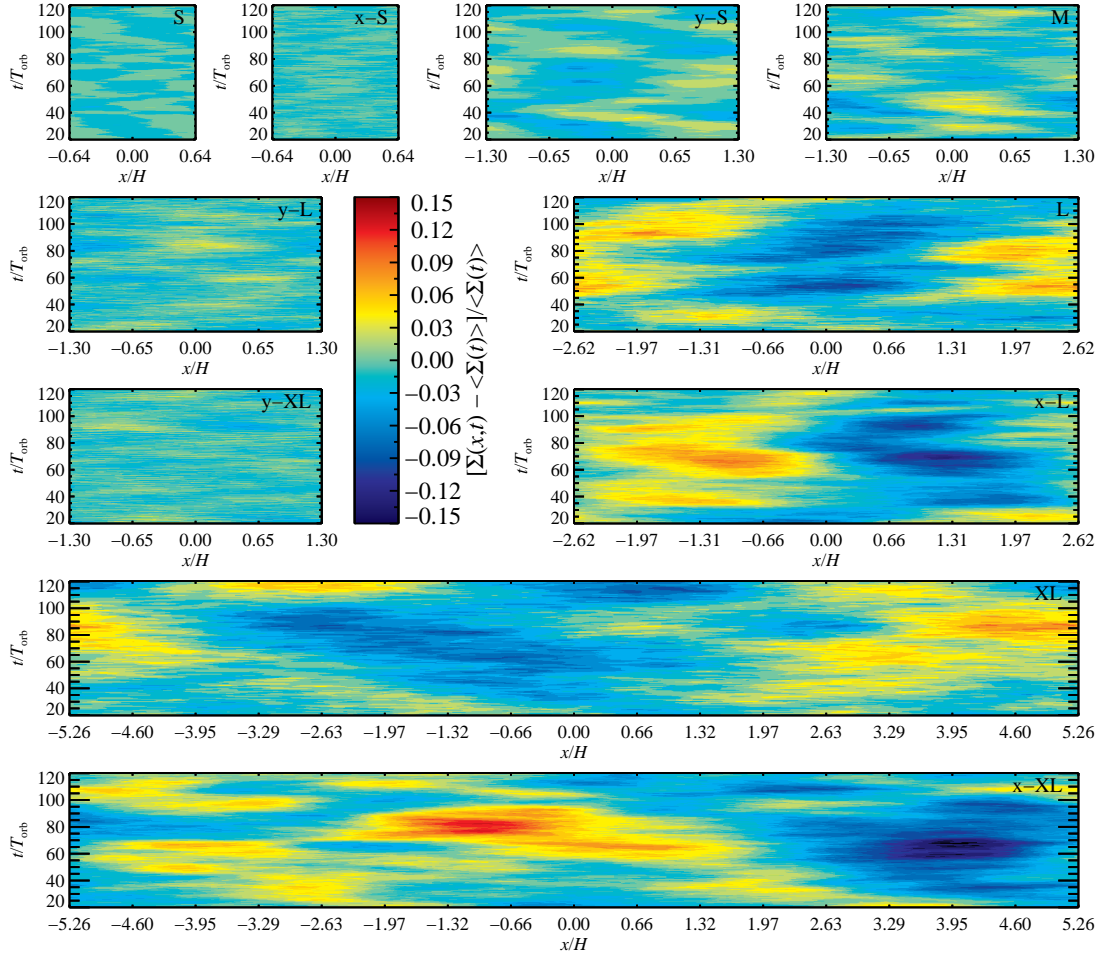
Figure 3.5 The evolution of the gas density perturbation of all runs from simulation sets *A*, *B*, and *C*. Run *XXL* is shown in Figure 3.6. The density is averaged in vertical and azimuthal direction and plotted in radial direction over time. The life-time, the size as well as the strength of the pressure bumps is clearly increasing with increasing box size in simulation set *A*, i.e., runs *S*, *M*, *L*, *XL*, and *XXL*. In simulation set *B*, i.e., runs *x-S*, *M*, *x-L*, and *x-XL*, I have the same increase of life-time, size and strength of the pressure bumps. Only for the very large simulation ($L_x = 10.56H$) there is no apparent difference in pressure bump size and strength to run *x-L*. For simulation set *C*, i.e., runs *y-S*, *M*, *y-L*, and *y-XL*, the strength of the pressure bumps is apparently constant throughout this set of simulations. Even the life-time decreases slightly with increasing box size.

structures. The correlation times measured in this fashion are in good agreement with the lifetime of the over-densities that is seen in Figures 3.5 and 3.6. However, a change of position of the structures, as seen in run *XL* (check Figure 3.5), is not accounted for. Thus, correlation times are more likely to be under- than overestimated. Also, one cannot be entirely sure whether this behavior is really drift or structure decay and reformation.
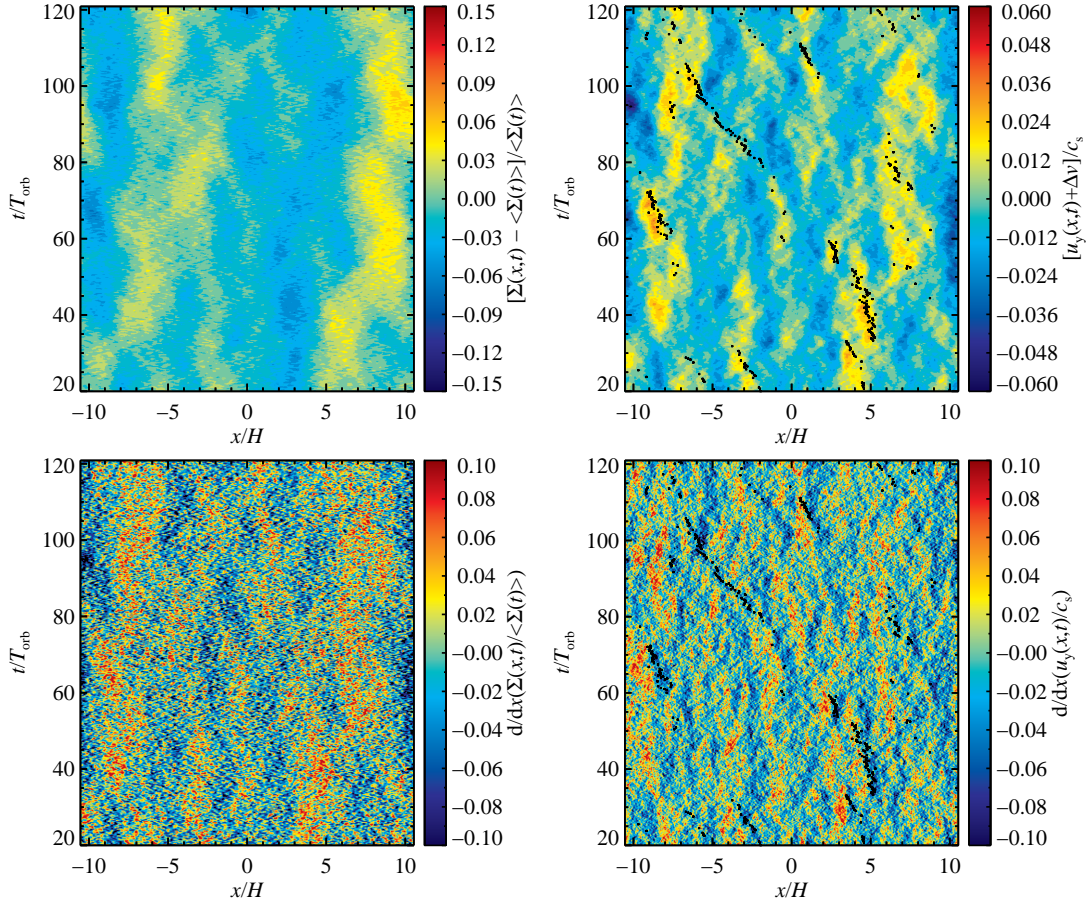
Figure 3.6 The top panels show the evolution of the gas density perturbation and the azimuthal gas velocity of run *XXL*, whereas the bottom row shows the radial derivative of these quantities. The derivatives are very speckled, since small scale fluctuations give stronger amplitudes to the derivatives. However, the underlying large scale structure is still visible. The azimuthal gas velocity follows the radial gas density gradient, as expected for a geostrophic balance. Hence, it is possible to interpret the radial derivative of the azimuthal gas velocity as the second derivative of the gas density. In the upper right panel, the black dots represent the position of the most massive particle clump in the simulation at each time. It is clearly shown that particles get trapped in regions of positive zonal flow downstream of pressure bumps.

The results of the correlation time determination are shown in Table 3.3 and in the upper panel of Figure 3.7. For the diagonal simulation set, (*A*), the correlation time increases with box size. It seems to saturate towards the largest box size. The trend to longer correlation times is also evident for simulation set *B*. Here only run *x-XL* has a shorter correlation time than expected. This might be an effect of the strongly stretched simulation box. The correlation time decreases slightly with an increasing azimuthal box size in simulation set *C* (not shown in the figure). The lower panel in Figure 3.7 shows a measurement for the physical size of the zonal flow features. I Fourier-transformed the vertically and azimuthally averaged gas density and az-
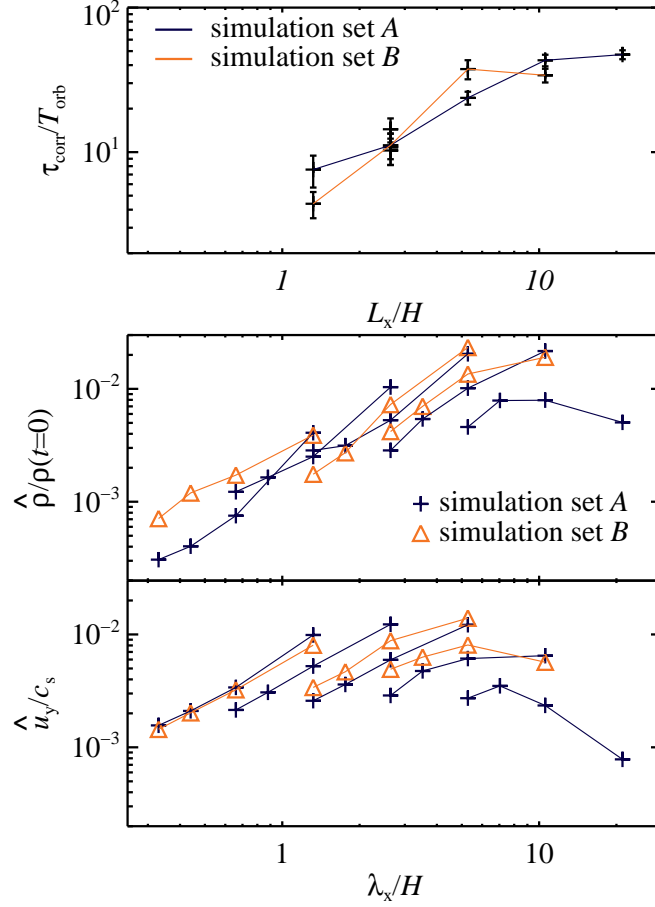
Figure 3.7 The upper plot shows the correlation times of the largest radial density mode against the radial box size. The lines correspond to the simulation sets A and B. The results from simulation set C are omitted for visibility. The correlation time τ_{corr} grows for boxes with a larger radial extent. Only run x-XL does not follow this trend. The large ratio L_x/L_y may prohibit formation of stable zonal flows. The two lower plots show the first four amplitudes of the radial Fourier modes of the gas density and the azimuthal gas velocity against their real size $\lambda_x = L_x/k_x$; k_x is the wave number of the corresponding Fourier mode, defined by $\omega_x = 2\pi k_x/L_x$ in the Fourier mode $\sin(\omega_x x)$. The lines connect the amplitudes of different Fourier modes for one simulation. Both quantities have most of their power in the largest modes. Only in the largest simulations, the power in the largest modes decreases. There the maximum is between $5H$ and $7H$.

imuthal gas velocity for each time step and averaged the amplitudes of the first four modes over the time of $20 \ldots 120$ local orbits. The length was normalized for the size of the simulation box, to get the physical size of the modes by $\lambda_x = L_x/k_x$ with the wave number k_x. The turbulence is always strongest at the largest modes for simulations with $L_x \lesssim 5H$. The highest amplitude for both quantities in the largest simulation domain is found between $5H$ and $7H$ (up to $10H$ for $\hat{\rho}$). These measurements are also found in Table 3.3.

The runs *L_SAFI* and *XL_SAFI* were carried out to compare the turbulence and zonal flow parameters with the runs *L* and *XL*. They were run to check that zonal flows are no effects from the shear advection scheme that was used in the PENCIL CODE. Comparing the values in Tables 3.2 and 3.3 shows that there is little change in the measured properties of the zonal flows and the associated pressure bumps. However, the computation time increases if one uses the SAFI scheme. Thus, this scheme was only used to confirm my results.

3.4   Dust Particles in Zonal Flows

Particle accumulations and planetesimal formation can occur in clumps and filaments of the over-densities in the dust. In my simulations no gravitational interaction between the particles is included. Thus, I only study the passively developed over-densities of the dust to see when and whether over-densities sufficient for the streaming instability can be reached. By not having explicit feedback one can retroactively study the concentration factor for various initial dust-to-gas ratios. Simulations including feedback are presented in Chapter 4. Figure 3.3 shows the position of every 100th particle in selected simulations. These plots clearly show the trend for particles to accumulate in the downstream of high pressure regions. Particles are pulled towards pressure gradient maxima independent on their absolute value or radial width (Klahr and Lin, 2001). In the upper right panel in Figure 3.3, a snapshot of run *XL* after 85 local orbits is shown. The particles clump up at positions just left of the maxima in the $k_x = 1$ mode of the gas density; these are the locations of positive zonal flows, i.e., regions where the azimuthal gas velocity is higher than the pressure-supported Keplerian flow.

3.4.1   Dust Concentration

In the upper right panel of Figure 3.6, the azimuthal gas velocity development of run *XXL* is shown, over-plotted with the position of the most massive clump for each time step. The azimuthal gas velocity coincides with the derivative of the gas density, but it is much easier to interpret. The speckled structure of the derivatives comes due to the high power in the smaller scales. However, the large-scale structure is still visible and the geostrophic correlation between the structures of $u_y(x, t)$ and $d/dx[\rho(x, t)]$ is directly observed. Since they have the same large-scale structure, the particle position is much easier interpreted at the azimuthal gas velocity plot than on the density gradient plot. Sometimes the radial displacement from one orbit to the next is too large to be explained by radial drift. That happens when another clumps becomes more massive than the previous one. These particles accumulate in regions with high azimuthal gas velocities (see upper right panel in Figure 3.6). The only time when this is not true is at times from 80 to 100 local orbits. In this period an inwards-drifting clump stayed coherent during the time of its drift. The drift velocity of the most massive particle clump is indirectly encrypted in this plot. Particles are drifting much slower when they are trapped by a pressure gradient. As all particles drift inwards

this leads to accumulation of particles in regions where the perturbed pressure gradient is positive.
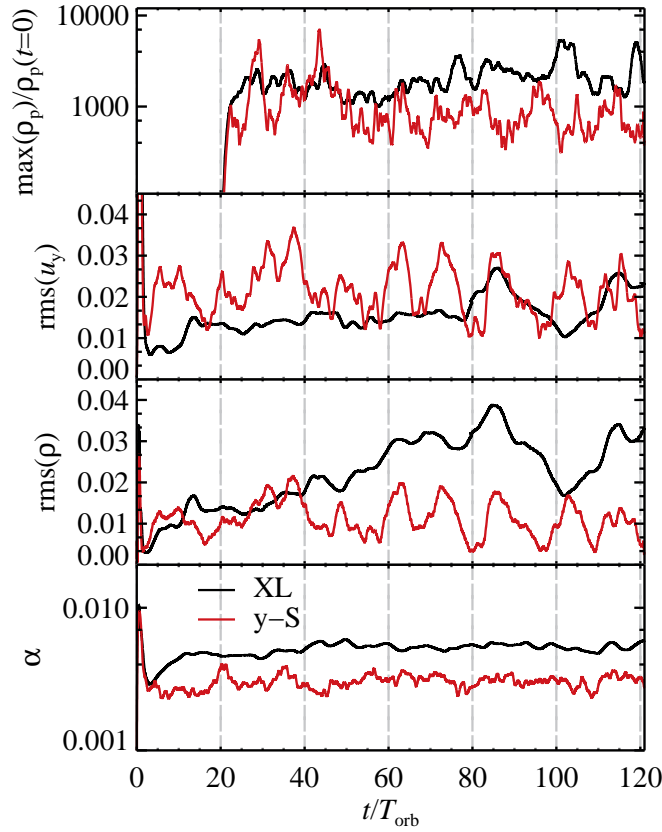
Figure 3.8 Time series of runs *XL* and *y-S*. The plots show (from top to bottom) the maximum of the dust density, the root mean square of the azimuthal gas velocity and the gas density, and the α-value (equation 3.19). The dust over-densities of run *XL* have a higher base than those of run *y-S*. The latter has some spikes in the beginning, but is lower for most time of the simulation. The two panels in the middle show that the azimuthal gas velocity and the gas density are correlated. Both plots show maxima and minima at the same time, while α is rather stable with time. The time-averaged α-values for all simulations can be found in Table 3.2.

The maximal accumulation of particles for runs *XL* and *y-S* are plotted in the top panel in Figure 3.8. The second panel shows the evolution of the quantity $\sqrt{\langle u_y - \langle u_y \rangle_{yz} \rangle_x^2}$, a measure for the strength of the zonal flows. The third panel in Figure 3.8 shows the evolution of the strength of the gas density enhancement as $\sqrt{\langle \rho - \langle \rho \rangle_{yz} \rangle_x^2}$. Comparing the second and third panel, one can see a clear correlation between the zonal flow strength and the gas density enhancements. The bottom panel in Figure 3.8 shows the evolution of the α-parameter, calculated as in equation (3.19).

The maximum of the dust over-density that occurs during one simulation is plotted against the box size in the left panel of Figure 3.9. The general trend shows that
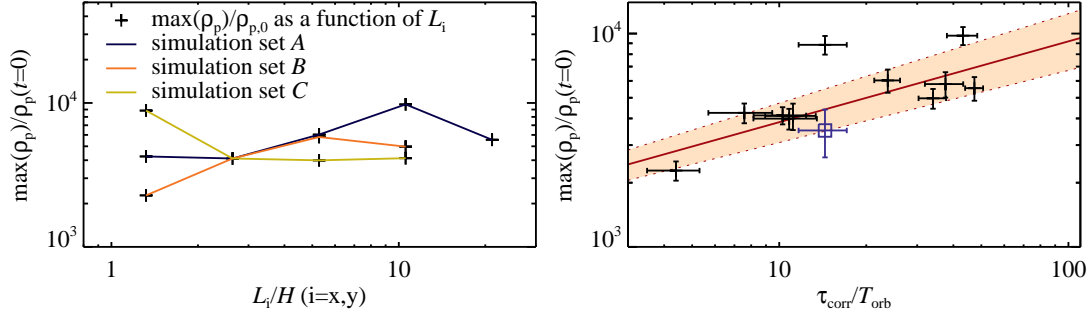
Figure 3.9 In the left panel, the highest peak in the time series of the dust over-density (top panel in Figure 3.8) is plotted against the size of the simulation box. The diagonal simulation set A is marked by the blue line. The dust over-density increases with box size, until it suddenly drops for the largest box. In simulation set B (red), the quantity saturates for boxes with a radial extent that is twice as large as the azimuthal extent or larger. When keeping the radial extent constant (simulation set C, yellow line), the maximum saturates for the cubic box case. Hence, the only in azimuthal direction extended boxes do not lead to an articifial enhancement of the dust over-densities. The very high over-density for run y-S seems to be a stochastic coincidence (compare top panel in Figure 3.8). The right panel shows the dust over-density against the correlation time. The measured points can be approximated with a power law (shown as a red solid line) with an exponent of 0.38 ± 0.05. The shaded region, with the dashed red lines as edges, gives the uncertainty of the fit. The one cross off the fit shows the results for run y-S. The blue square marks its position, if one neglects the two maxima shown in Figure 3.8. It overlaps well with the fit region.

radially larger boxes have higher particle concentrations. An increased azimuthal extent does not have an effect on the particle concentrations. The most surprising result is in run y-S. It shows a very high particle concentration that occurs early in the simulation (compare Figure 3.8). This is most likely a stochastic coincidence. The right panel in Figure 3.9 shows a plot of the maximum dust over-density against the correlation time of the zonal flows. The error margin are calculated with the standard deviation of the temporal evolution of the two quantities. There is a clear trend that denser particle accumulations develop with longer correlation times. The distribution can be fitted by a power law. This gives an exponent of $d \log \rho / d \log \tau_{\mathrm{corr}} = 0.38 \pm 0.05$. The one point that does not overlap with the error margins of the fit is from run y-S. If one takes the maximum of the top panel in Figure 3.8 after the two first maxima (i.e., after $45 T_{\mathrm{orb}}$) and plot this value again in the parameter space of Figure 3.9, one gets the position marked with the blue square. It agrees well with the error margins of the fit.

In isothermal geostrophic balance, $2\rho \Omega u_y = c_s^2 \partial \rho / \partial x$, the azimuthal gas velocity follows the radial density gradient. That this is true for large scales as shown in Figure 3.10. The upper left panel shows the evolution of the azimuthally and vertically averaged azimuthal component of the gas velocity. Over-plotted are the locations of the maxima in the dust density. In the upper right panel the dust density evolution of the same run L is plotted. In comparing the location and times of the maxima and minima on these two plots, one clearly sees that maxima in the dust density occur of-
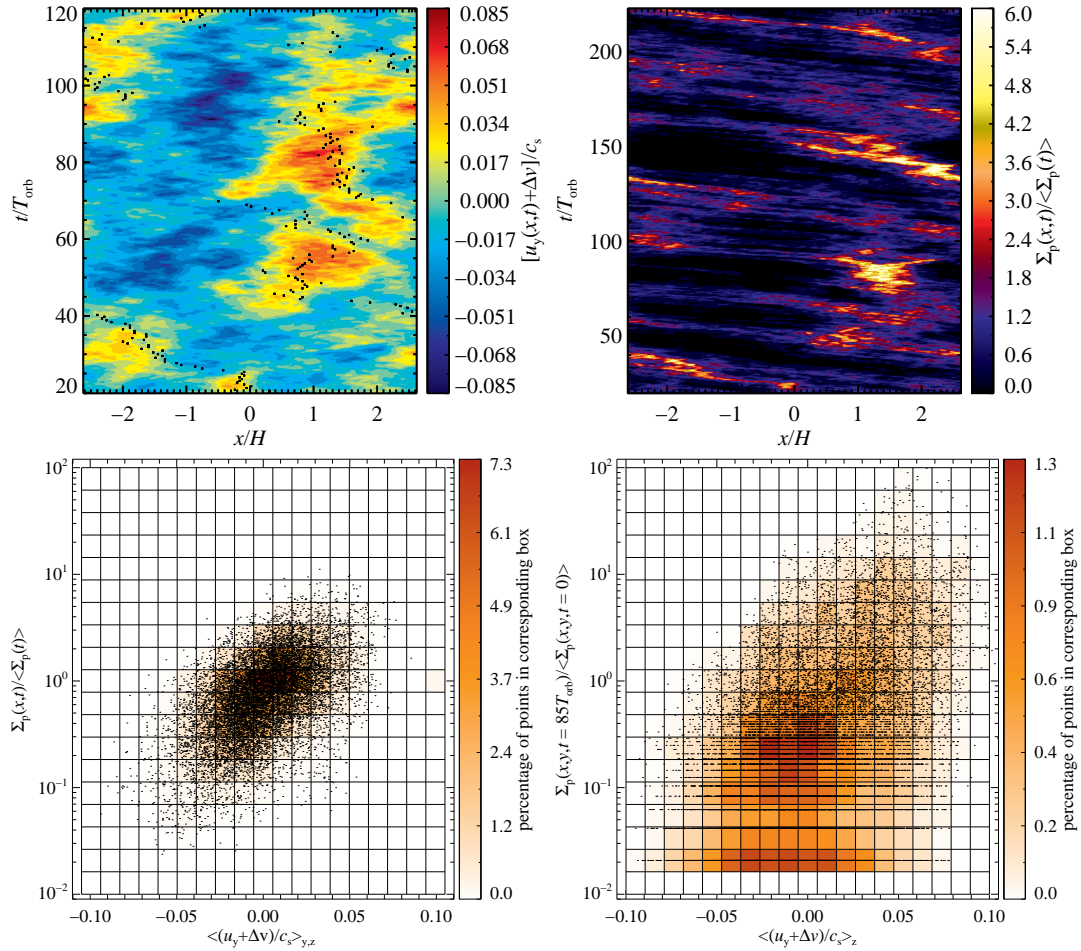
Figure 3.10 The top row shows the evolution of the azimuthal gas velocity and the dust density evolution of run L respectively. The quantities are averaged in vertical and azimuthal direction and plotted in radial direction over time. The black dots in the upper left panel show the position of the highest dust density at each orbit. This shows that the over-densities of the dust often appears at places and times where the azimuthal gas velocity is high. This relation shows that the zonal flows accumulate dust and are a possible venue of planetesimal formation. The bottom left panel shows a scatter plot of the dust density ρ_p against the azimuthal gas velocity, where both values are averaged in vertical and azimuthal direction, as in the upper panels. The bottom right panel shows a plot of the particle surface density $\rho_p(x, y, t)$ in relation to the azimuthal gas velocity, averaged in vertical direction, computed from a snapshot taken at $85T_{orb}$, the time when the maximum in the dust density occurs. Both plots show that it is more likely to find a high dust density at a location where the azimuthal gas velocity is high.

ten at times and locations where one finds maxima in the gas velocity. Two attempts to quantify this observation are shown in the lower row of Figure 3.10. In the left panel, the particle density and the azimuthal velocity from the two upper panels are plotted against each other, regardless of position and time. In the right panel, a snapshot of the

simulation (as in Figure 3.3) was taken at 85 local orbits, the time when the maximum dust density enhancement occurs. The particle density as well as the azimuthal gas velocity were integrated in vertical direction and plotted against each other, regardless of their radial or azimuthal position in the simulation, in this scatter plot. In order to visualize high densities of points in these plots, I computed a 2D-histogram of the scattered points. This is indicated by the color scale, showing the amount of points in each of the boxes in the scatter plot space. There is a clear trend for high dust density concentrations to appear at high gas velocities. Without radial drift particles would concentrate where $u_y = 0$, i.e., between the sub- and super-Keplerian flow. Due to the radial drift particles accumulate slightly downstream at the formed pressure bumps. Those happen to be at the maxima of the azimuthal gas velocity. With the geostrophic balance, high velocities are also regions of a high radial density gradient. These plots prove that the particles in the simulations are trapped by the long lived pressure gradients that occur due to stable zonal flows.

If the dust-to-gas ratio increases to values larger than unity, the streaming instability (SI; Youdin and Goodman, 2005; Johansen and Youdin, 2007; Youdin and Johansen, 2007) is triggered. This increases the dust density further on timescales shorter than an orbital period. To follow the SI development, the back-reaction of the dust particles to the gas phase must be considered in future numerical simulation. This effect was neglected in this set of simulations. Otherwise the initial dust-to-gas ratio would have been an additional free parameter to be studied. The SI is studied in Chapter 4.

3.4.2   Radial Drift

Radial drift velocities of the particles in the simulations with different box sizes are shown in Figure 3.11. The upper panel shows the measured and expected radial drift of two simulations (*M* and *XL*). They show that particles drift slower in turbulent simulations than they would in a laminar disk. However, the size of the simulation has little effect on the actual drift velocity, as shown in the lower panel of Figure 3.11. It shows a time average of the particle drift velocity plotted against the box size. The uncertainties are too large to reveal a trend. Thus, the reduction of the radial drift velocity apparently only depends on the amplitude of the zonal flow, but not on the correlation time. Looking at the largest run *XXL*, one can estimate that the radial drift gets reduced by about 28% (drop of the absolute value from $0.05c_s$ to $(0.036 \pm 0.003)c_s$).

3.4.3   Clustering

The clustering degree of the particle distribution can be estimated with the distribution of the dust surface density Σ_p (Pan et al., 2011). The initial distribution is represented by a Poisson distribution (see Figure 3.12).[5] For this plot, the measured dust surface density of a snapshot is binned and normalized to the amount of grid cells.

---

[5]Run *XXL* was not included in this figure, because the number of particles per grid cell was different to the other runs.
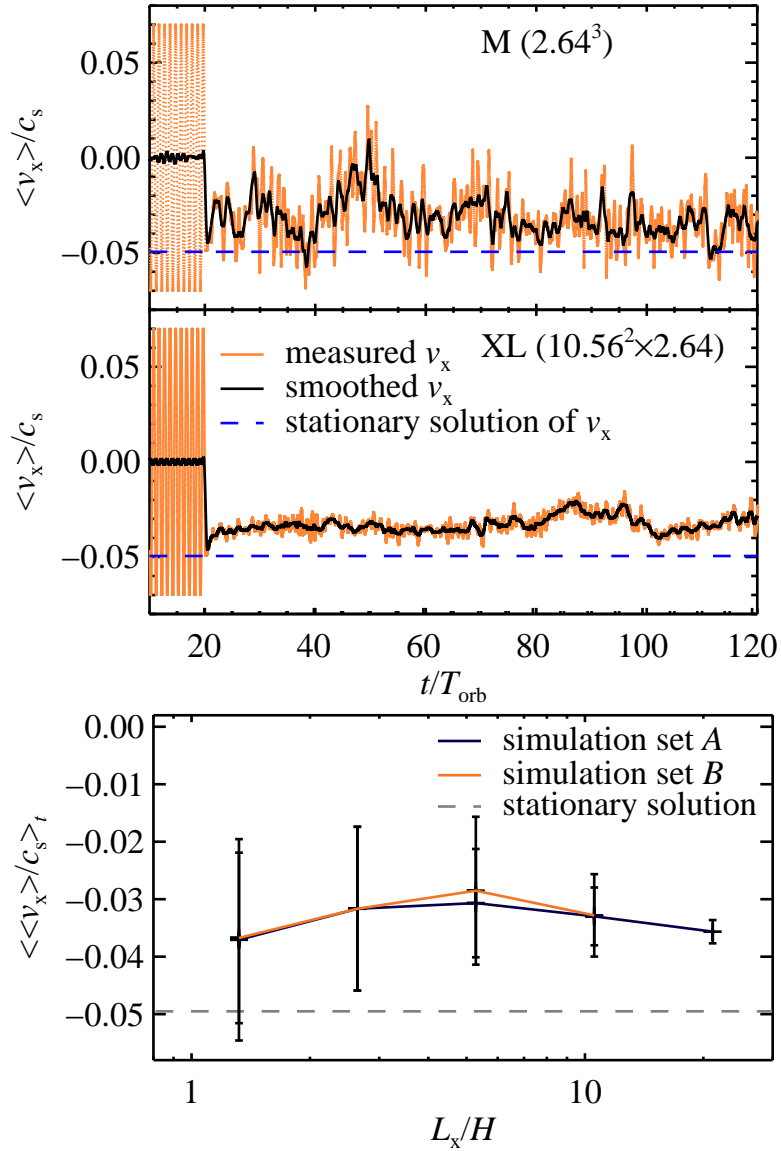
Figure 3.11 The radial drift velocity of the particles for two different simulations is shown in the upper panel. Particles in these simulations all have a Stokes number of $St = \tau_f\Omega = 1$. The orange lines are the exact measured radial velocities, averaged over all particles. The black line represents the same value smoothed over the time of one local orbit. The blue dashed line shows the analytical result in a stationary box for particles of $St = 1$ following equation (3.12). Particles in turbulent simulations generally drift slower than expected from the stationary solution, but the box size has little effect on the drift velocity. This is shown in the lower panel where the mean of the radial drift velocity is plotted against the box size. Simulation set *C* is omitted for visibility. There is a minimum in drift speed for run *L*. However, this minimum is within the error margins. The smallest errors are with run *XXL*; here the drift velocity drops by 28%.

About three local orbits after the particles feel the gas drag, the shape of the distribution function is saturated. I averaged the distribution over the time of $23 \ldots 121 T_{orb}$. The high density end of the distribution that higher densities develop in larger boxes due to the higher number of available particles. Thus, the clustering properties do not depend strongly on the strength or life-time of the zonal flows (compare Figure 3.9, bottom). Another way to show the clustering degree is presented in Section 3.5.2.
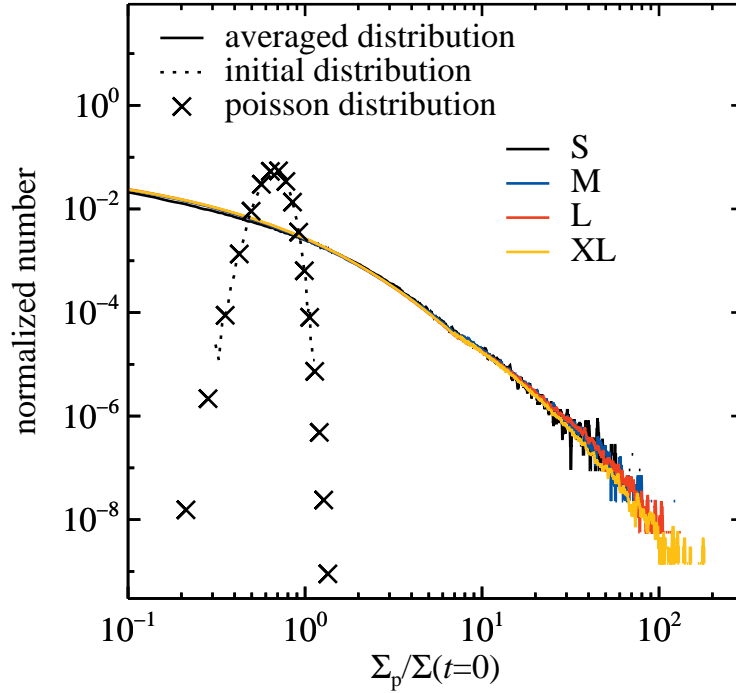
Figure 3.12 Distribution of the dust-to-gas ratio of the surface densities for runs *S*, *M*, *L*, and *XL*. For comparision a Poisson distribution is shown with crosses. The initial distribution of the numerical simulation (dotted line) fits very well to the normal distribution. The average strength of the clustering for the dust surface density does not depend on the simulation box size.

3.5   Collisions of Dust Particles

3.5.1   Method

Simulations cannot resolve both, the hydro-dynamical turbulence of sizes between the largest scales (l_p) and the smallest scales (l_d) and the dust grains of size $s \ll l_d$ interacting with it, at the same time. In protoplanetary disks the different scales span many orders of magnitude. Thus, direct measurement of the collision velocity is prohibited. One must study snapshots of the entire system and convert their particle number, pair separation, and relative velocities into global collision rates and collision velocities.

I assume that for any relative velocity Δv there is a size scale l_d, that is much smaller

than the smallest turbulence length l_ν and at the same time much larger than the dust grain size s. I further assume that in all spheres of radius $r < l_d$ constructed around target dust grains, the number density of dust grains with velocity Δv with respect to a target grain is constant. This assumption breaks down if two particles get very close to each other. Then new physics might emerge that have not been taken into account in my simulations. These new physics might manifest in gravitational or electrical interactions of the possibly charged dust grains. For too large particles, this assumption breaks down as well, since they might induce wakes in the gas that affect particle pair interactions. Both effects cannot happen in my set of simulations.

My simulations use the shearing box approximation; however, for the measurement of relative velocities I subtract the shearing velocity in the azimuthal velocity component. Firstly, the shear gives a known contribution to the relative velocity ($\sim |v_K(R^i) - v_K(R^j)|$ for particles i and j) and secondly, the shearing velocity contribution becomes negligible for very small distances. Since I am interested in relative velocities at small particle separation, I can safely neglect the shearing velocity.

Sampling Method

I take snapshots of the particles with a temporal separation $\Delta t = 0.5 T_{\text{orb}}$. The distance Δr and the relative velocity Δv in logarithmic bins. The bin boundaries are denoted by $v_{\min}$ ($r_{\min}$) and $v_{\max}$ ($r_{\max}$). The number of particle pairs p_1 and p_2 of distance Δr with a realtive velocity Δv at time t is $N(\Delta r, \Delta v, t)$. The particle pairs are sorted in this 2D-histogram for a snapshot taken at time t by $|x_1 - x_2| < r$, $\log(|v_1 - v_2|) \in \log(\Delta v) \pm \delta v/2$. Here, $\delta v = |\log(v_{\max}) - \log(v_{\min})|/n_{\text{bins},\Delta v}$ is the bin width in logarithmic values.

My sampling ensures that I achieve full coverage of all particle pairs up to a distance of $0.1H$. Since I use cubic boxes, the sampling also covers some particle pairs at slightly larger separations.

I further define the effective number density of particles at relative velocity Δv in spheres of radius r as seen by particles in the snapshot t by

$$n(r, \Delta v, t) \equiv \frac{N(r, \Delta v, t)}{n_p \left(4\pi/3 \times r^3\right)}, \tag{3.21}$$

similar to Hubbard (2013). For $N(r, \Delta v, t)$ as well as for $n(r, \Delta v, t)$, a dropped Δv implies summation over velocity bins while a dropped t implies averaging over snapshots. A dropped r implies a limit $r \to 0$ and is discussed below.

Sampling Rate

A particle pair can appear in multiple consecutive snapshots, if the relative velocity Δv is smaller than $2r/\Delta t$. Thus, regions of over and under-densities can get over-sampled. Hence, I choose the safe assumption that $\Delta t > 2r_{\max}/v_{\min}$ where $r_{\max}$ is the largest particle-particle separation considered and $v_{\min}$ is the smallest relative velocity considered.

The MRI turbulence generates significant structure in the particle distribution which are destroyed and reformed numerous times during my simulations. To smooth over these extrema, one will have to average over a long enough time interval. Additionally, particles with different stopping times are affected differently by the gas flow. Thus, I sample over different stopping times in run *LspecMR*.

One should examine the time series of $N(r, \Delta v, t)$ to verify that the particle population achieved a steady state. One further needs to assure that the sampling window is long enough to average over short-time and long-time fluctuations.

Sampling Radii

The drag force will significantly affect the relative motion of particle pairs within a separation Δr before they collide, if $\Delta r / \Delta v > \tau_f$. Thus, one can extract collisional information only from velocities larger than the minimum velocity $\Delta v \gtrsim \Delta r / \tau_f$. Particle relative velocities are expected to couple strongest to turbulence with turnover time $t_{l_p} = \Omega \simeq \tau_f$. Thus, the collisional sphere of the same size of that turbulence, $l_p = u_{l_p} t_{l_p}$, cannot resolve collision velocities of u_{l_p} or less. One needs to resolve particle separations much smaller than the turbulent length scale to be able to resolve collision rates and collision velocities for dust grains. This constraint is stronger for modest velocities as are expected for close pairs.

Limit of Small Radii

Particle pairs with a relative velocity $\Delta v > \tau_f \Delta r$ do not reach each other before their motion is affected by the turbulence. Thus, I have to take the limit $n(\Delta v_\star) = \lim_{r \to 0} n(r, \Delta v_\star)$ for all values of Δv where $\Delta v_\star \gg r_{min} / \tau_f$. For any further analysis I assume that $r < l_d$ is achieved.

3.5.2   Particle Clustering

I primarily show the results for the results of run L. The measured particle number density is shown in Figure 3.13. The dependence of relative velocity with particle separation gets weaker for small inter-particle separations.

The left panel of Figure 3.14 shows the effective particle number density within spheres of radius r, the clustering of particles, for run L. The density is higher for particle pairs with smaller separation. On very small scales, the resolution is preventing a further increase of $n(r)$. The largest scales show a slight decrease of density, because I have no longer full coverage of particle pairs with distance $r > 0.1H$. Between these two extrema $n(r) \propto r^\beta$ with $\beta = -0.90 \pm 0.05$. This clustering is stronger than all clustering from the isotropic turbulence runs in Hubbard (2012) or Pan and Padoan (2013), showing again the power in long-lived structures such as the axisymmetric pressure bumps in zonal flows.
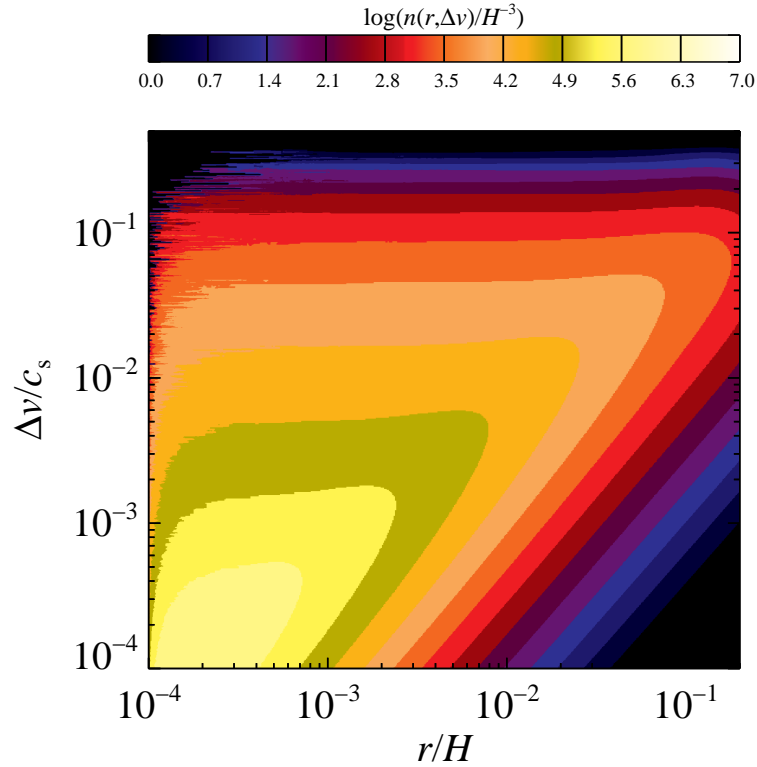
Figure 3.13 The time-averaged effective particle number density of collision pairs for run *L*. The number density does little depend on the distance to each other for velocities larger than $v = 10^{-3}c_s$ and distances shorter than $\Delta r = \Delta v \Omega$.

3.5.3 Velocity Distributions

The velocity distribution $n(\Delta v)$ for different radii is shown in the right panel in Figure 3.14. The colors show the radii at which the velocity distribution was measured. Solid lines show $n(\Delta v_\star)$, while dashed lines complete the velocity distribution. It shows that the maximum in the velocity distribution is lower than r_i / τ_f. These distributions can be used for coagulation models like Birnstiel et al. (2012); Windmark et al. (2012b). Figure 3.15 shows the result of a fit to the velocity distribution at $r = r_7$. I used the fit formulas from Hubbard (2013) of a quasi-Maxwellian

$$f_M = a_M \frac{2c_M}{\sqrt{\pi}} \left(2b_M c_M^2 + 1\right) \frac{\Delta v^2}{b_M + \Delta v^2} e^{-c_M^2 \Delta v^2} , \tag{3.22}$$

a quasi-exponential

$$f_E = a_E c_E \left(\frac{b_E c_E^2}{2} + 1\right) \frac{\Delta v^2}{b_E + \Delta v^2} e^{-c_E \Delta v} , \tag{3.23}$$

and a clustered function

$$f_C = a_C \frac{c_C^3 \Delta v^2}{2} e^{-c_C \Delta v} . \tag{3.24}$$
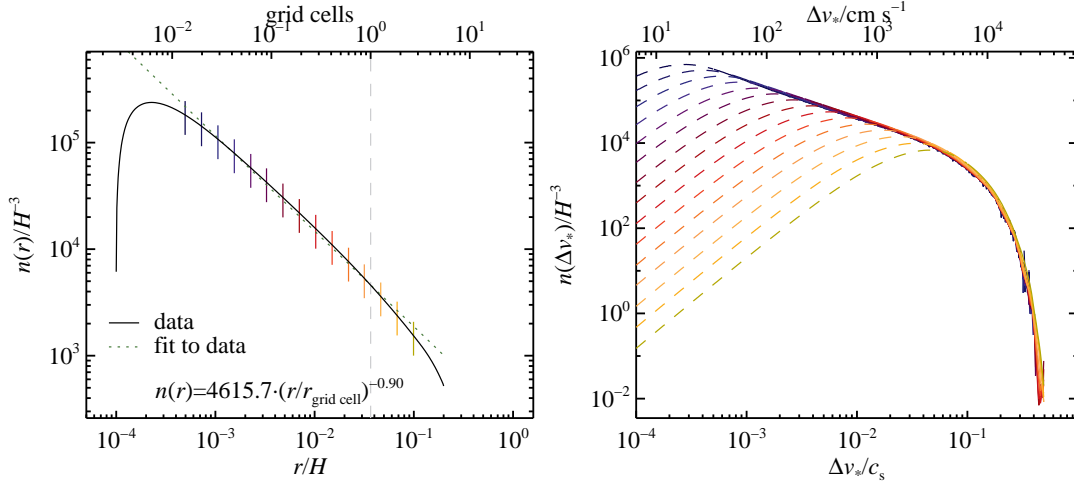
Figure 3.14 The left panel shows the effective particle number density within spheres of radius r of run L. Sampling radii r_i are shown as vertical lines. The dotted green line shows the fit of $n(r)$ for $r_1 < r < r_{15}$. This part follows a power law with the index -0.90 ± 0.05. The right panel shows the cuts through $n(r, \Delta v)$ at sampling radii r_i from run L. The colors correspond to the same colors as in the panels above. Solid lines show the part of the velocity distribution that is used further in calculating the rms collision velocity. Dashed lines complete the measured velocity distribution.

The full fit formula is composed as the sum of the three parts:

$$f(\Delta v) = f_M(\Delta v) + f_E(\Delta v) + f_C(\Delta v). \qquad (3.25)$$

Contrary to the findings[6] in Hubbard (2013), I find that the velocity distribution fits best if I allow all components. This may be due to the difference of a axisymmetric pressure bump and the resulting stronger clustering.

Rating $n(\Delta v_\star)$ with $\Delta v_\star$, I obtain the contribution of velocity bin $\Delta v_\star$ to the collision rate for a single particle. Summing over all velocity bins gives the total collision rate for a single particle $Z(r) = \sum_{\Delta v} \Delta v_\star n(\Delta v_\star, r)$.

3.5.4   Collision Velocities

In a velocity distribution one can obtain several typical speeds:

- the most probable speed $\Delta v_{\text{max(n)}} = \Delta v(\text{max}\,[n(\Delta v)])$,

- the mean speed $\langle \Delta v \rangle = \sum_{\Delta v} \Delta v n(\Delta v) / \sum_{\Delta v} n(\Delta v)$, and

- the rms speed $\Delta v_c^{\text{rms}} = \{[\sum_{\Delta v} \Delta v^2 n(\Delta v)] / [\sum_{\Delta v} n(\Delta v)]\}^{1/2}$.

---

[6]They recommend to fit the velocity distribution for equal-sized particles with $f = f_M + f_E$.
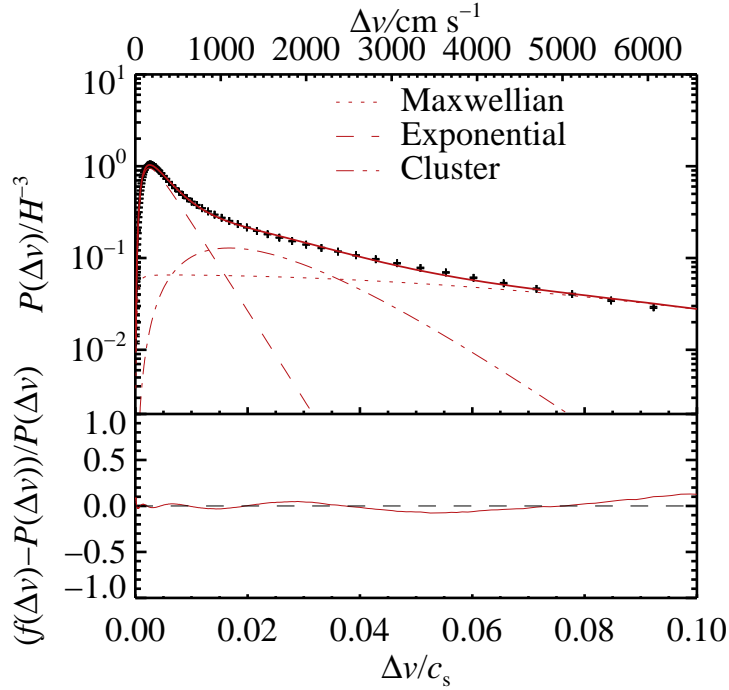
Figure 3.15 A fit to the velocity distribution of run L. The distribution is normalized with $P(v, r = r_7) = n(\Delta v, r = r_7)/Z(r = r_7)$.

Note that $\max [n(\Delta v)] < \langle \Delta v \rangle < \Delta v_c^{\mathrm{rms}}$. The latter can be rated by the collision energy, following

$$\Delta v_c^{\mathrm{rms}} = \sqrt{\frac{\sum_{\Delta v} \Delta v_\star^3 n(\Delta v_\star)}{\sum_{\Delta v} \Delta v_\star n(\Delta v_\star)}}. \tag{3.26}$$

The results for $\Delta v_c^{\mathrm{rms}}(r_i)$ are shown in Figure 3.16. The root mean squared collisional velocities as a function of separation follows a power law $\Delta v_c^{\mathrm{rms}}(R) = R^b + c$. The parameter c remains for $\Delta v_c^{\mathrm{rms}}(R \to 0)$. Thus, $c = \Delta v_c^{\mathrm{rms}}(r \to 0)$ gives an estimation for the collision velocity at zero separation. The lines in Figure 3.16 show comparisons to the measured gas root mean square velocity u^{rms} in my numerical simulation, the analytical approximation for the measured α (Shakura and Sunyaev, 1973), following Ormel and Cuzzi (2007), $u^{\mathrm{rms}} = \sqrt{\alpha} c_s$, and the resulting $\Delta v_c^{\mathrm{rms}}(r \to 0)$. According to Ormel and Cuzzi (2007) St $= 1$ particles have a ratio $\Delta v_c^{\mathrm{rms}}/u^{\mathrm{rms}} = 1$.

3.6 Dust Particle of Different Sizes

So far I only considered simulations with one particle species, i.e., St $= \tau_f \Omega = 1$. I take the simulation size that simulates one fully extended zonal flow and investigate 12 different particle species. The particle sizes range from St $= 0.01$ to St $= 100$. I choose run L with the dimensions $5.28H \times 5.28H \times 2.64H$ as simulation size for the last simulation set. For one simulation I used a smaller box, because the integration
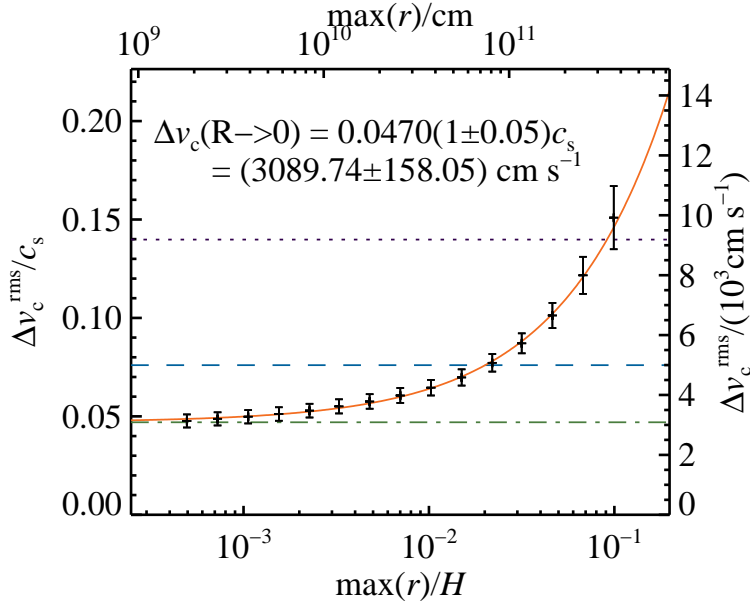
Figure 3.16 Root mean squared collisional velocities of particles at separations no larger than r in run L. Over-plotted in the solid read line is the fit to the data. The dotted purple line shows the gas rms-velocity. The dashed blue line is the Ormel and Cuzzi (2007) approximation $u^{\rm rms} = \sqrt{\bar{\alpha}}c_{\rm s}$ with the measured α (Shakura and Sunyaev, 1973) in this simulation. The dash-dotted green line shows the fit result $\Delta v_{\rm c}^{\rm rms}(r \to 0) = (0.34 \pm 0.02)u^{\rm rms}$.

time had to be increased be a factor of 2 to give the particles with the high Stokes numbers the opportunity to react on the pressure differences.

3.6.1 Drift Velocity and Particle Densities

The results are shown in Figures 3.17 and 3.18. The left panel in Figure 3.17 shows the negative of the radial velocity of the particles, averaged over all particles of a certain size and over time. The four different simulations match very well. The plot shows that particles with $St = 1$ drift fastest inwards, also with turbulence in the simulations. On both sides the inwards drift velocity decreases with similar slopes. The key to the different colors and symbols is in the lower right panel. Overplotted, in a dashed grey line, I find the analytical prediction (following equation 3.12) for the radial drift in a laminar disk. The difference to the prediction is shown in the lower sub-panel. Large particles generally drift slower according to the steady-state solution and their coupling to the gas is also much weaker. Hence their radial drift velocity is almost not affected by the turbulence and they do not show strong concentrations. Small particles with low Stokes numbers are stronger coupled to the gas and, thus, also drift very slow. Particles with $St \sim 1$ are concentrated most by the zonal flow and, thus, have a stronger decreased radial velocity. Thus, the accumulation of dust particles is expected to be strongest for particles with Stokes numbers around unity. For $St = 0.01$ particles, the drift velocity is strongly determined by the gas flow. This explains the
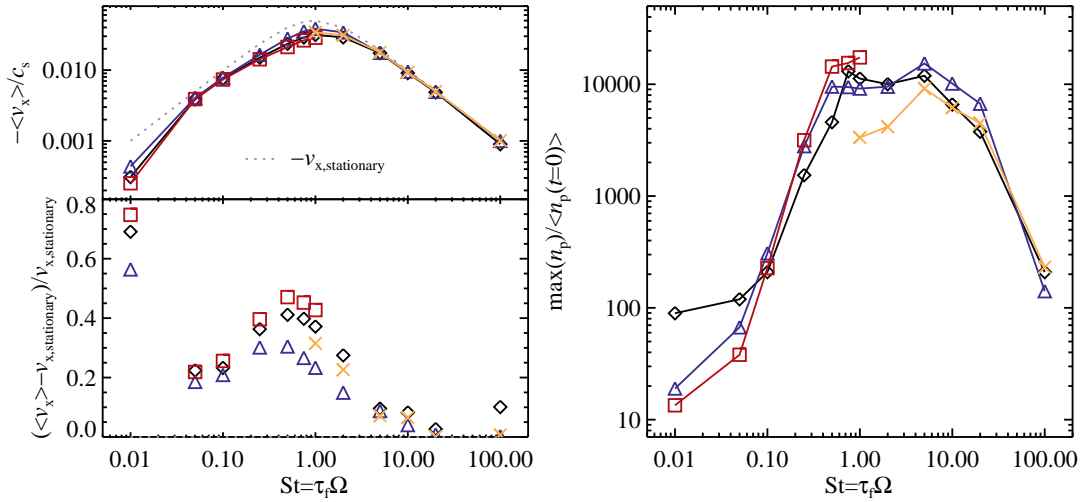
Figure 3.17 These panels show the behavior of particles with Stokes numbers from 0.01 to 100. The left panel shows the negative of the radial drift velocity and the relative difference between the measured and expected drift velocity. The dashed grey line shows the stationary solution for the radial drift, following equation (3.12). The highest drift velocities are obtained for particles with $St = 1$, but they are also slowed down strongest by the MRI-turbulence. The right panel shows the highest over-density that occurred for the specific particle size during the entire simulation. The slopes for the different simulations match very well, apart from a jump around $St = 1$ (for *LspecMRs* and *MspecMRb*) and an offset for run *LspecMR* at small particle sizes. The former can be explained with the usage of a smaller simulation box for run *MspecMRb* (2.64^3 with weaker zonal flows) than in the other simulations ($5.28^2 \times 2.64$ with stronger zonal flows). The offset showed that the number of particles per particle size was not sufficient in run *LspecMR* (10^5 particles in $\sim 1.5 \times 10^6$ grid cells leads with 5 particles in one grid cell to a result of $\max(n_p)/\langle n_p(t = 0)\rangle = 75$). The symbols in these plots are explained in Figure 3.18.

strong deviation from the expected drift velocity.

The right panel in Figure 3.17 shows the total particles over-density normalized to the initial particle number density. For run *LspecMR* (black diamonds), the smallest particles have higher concentrations than in the other simulations. This resulted from the choice of too few particles per grid cell. There only 100,000 particles per size bin were simulated. This results in over-estimation, because the number density is normalized with the initial number density n_0. For example, run *LspecMRs* (red squares) follows 2,000,000 particles per particle size bin. The highest concentrations were reached for particles of sizes $St = 0.75 \ldots 5$, as expected. However, the exact peak has a stochastic factor to it. Thus, the simulations peak at different particle sizes. The over-densities are more investigated in the lower row of panels.

The surface number density of the particles is shown in the left panel of Figure 3.18. Here, the particles were integrated in the vertical direction. The trend is similar to the upper right panel. I read from this plot that particles with $St = 0.1$ are concentrated about ten times the initial concentration. Together with the vertical over-density due
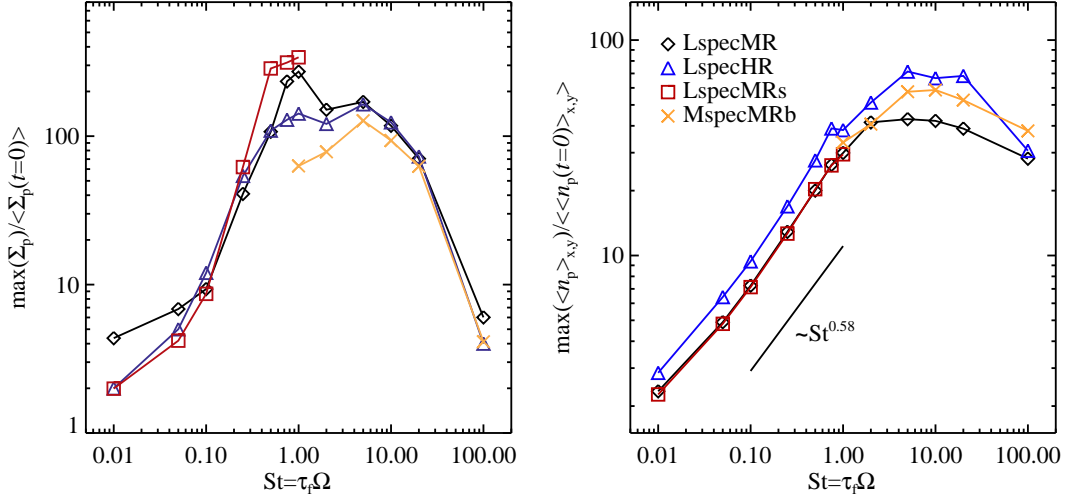
Figure 3.18 These panels show the behavior of particles with Stokes numbers from 0.01 to 100. The left panel shows the maximum of the column density for each particle size. It peaks at sizes of around $St = 1$. The right panel shows the maxima of the vertical distribution of particles. The curves (for $St = 0.01 \ldots 1$) follow a power law with the index of 0.58 ± 0.03. This is slightly steeper than the expected power law index of 0.5 (Dubrulle et al., 1995). In all four plots of Figure 3.17 and this figure, the results of particles with $St = 0.01$ are to be interpreted with caution, because the simulations lacked sufficient amount of super-particles for these size bins. Further, large particles ($St = 100$) did not have enough time to sediment to the mid-plane.

to sedimentation (right panel in Figure 3.18), a total over-density of about 100 is created for St = 0.1 particles.

The peaks in the vertical density structure of the particles are shown in the right panel of Figure 3.18. The Stokes number, St = $\tau_f\Omega$ defines the time scale after which the particles are settled down to the mid-plane. Particles with a high Stokes number, are not fully settled down to the mid plane, not even in the long-integration run *MspecMRb*. The resolution also limits this measurement for particles that are very close to the midplane. Smaller particles are not that strongly stratified. Thus, the vertical (Gaussian) structure is wider and shallower. This results in a lower value in this plot. The points for Stokes numbers 0.01 to 1 follow a power law with the index of 0.58 ± 0.03. The measured power law index is slightly higher than the expected value of 0.5 (Dubrulle et al., 1995). Most of the particles with St $\gtrsim 1$ sediment very close to the midplane. This prohibits a further increase in the vertical density. A higher resolution and a measurement of the dust scale height is achieved in the next section.

3.6.2   Dust Pressure Scale Height

With a stratified particle distribution I can test the vertical diffusion model (see, e.g., Carballido et al., 2006). The dust pressure scale height can be directly calculated from the vertical positions of the particles of the same size. It is approximately proportional to $St^{-0.5}$ in agreement with Carballido et al. (2006, 2011); Youdin and Lithwick (2007).
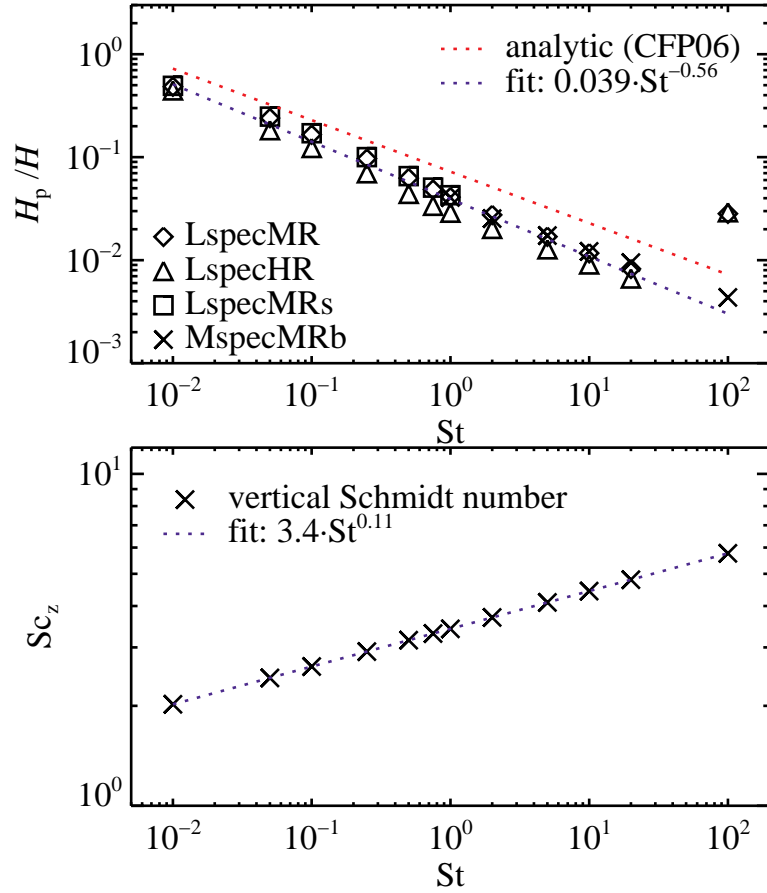
Figure 3.19 The dust scale height as a function of the Stokes number is shown in the upper panel. Different symbols depict the different simulations. The expected dust scale height is calculated after Carballido et al. (2006) and compared with the fitted function. This value is the vertical Schmidt number Sc_z, shown in the lower panel. Its dependence on the particle size is very weak.

The results are summarized in the upper panel of Figure 3.19. Since the analytical value was calculated with the α-value, the vertical Schmidt number

$$Sc_z = \frac{H_{p,\,\text{expected}}}{H_{p,\,\text{measured}}} \sim \left(\frac{\alpha}{D_T(\infty)}\right)^{\frac{1}{2}} \quad (3.27)$$

can be calculated. I measured the vertical Schmidt number to have a very weak dependence on the particle size. In the lower panel of Figure 3.19 I show that $Sc_z = 3.4 \cdot St^{0.11}$.

3.6.3 Collision Velocities

I also measured collision velocities for different sizes to compare my measurements better with analytical estimations. The run *LspecMR* has 12 different species from $St = 0.01$ up to $St = 100$. Results of that measurement are shown in Figure 3.20. Additionally, I performed one simulation (run *LspecMR2*) with 12 different particle

sizes from St $= 0.5$ up to St $= 2$. The measured rms collision speed is 2.6 ± 0.6 times lower than the analytical prediction from Ormel and Cuzzi (2007).[7] This is lower than the measured decrease of factor 4 in Hubbard (2012).
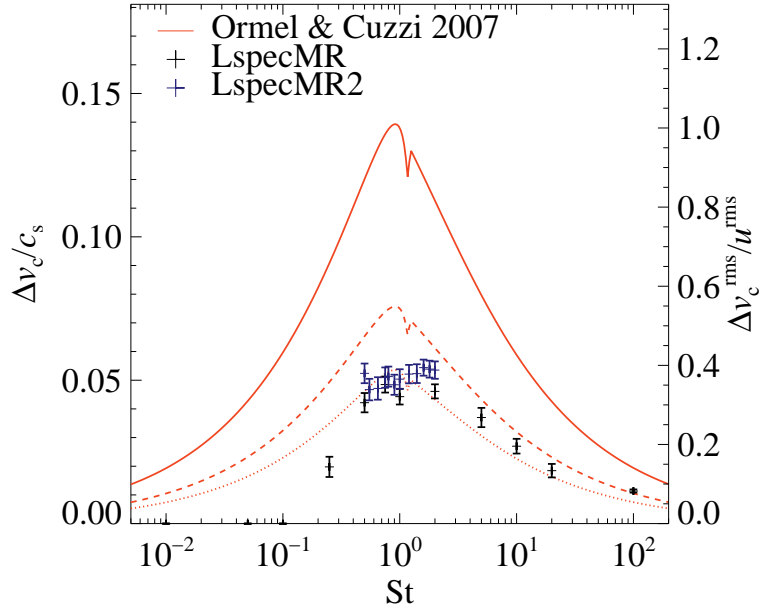
Figure 3.20 Here the comparison of collision velocities for different Stokes numbers is shown. The over-plotted red lines shows the analytical results following Ormel and Cuzzi (2007) using the measured u^{rms} (solid line), the analytical estimation $u^{rms} = \sqrt{\alpha}c_s$ (dashed line). The dotted line shows a by 2.6 devided result from the analytical predictions.

In my low-resolution simulations, I am not able to measure a reliable rms collision velocity for particles smaller than St $= 0.5$. One needs to investigate high-resolution simulations for the study of smaller particles. Additionally the collision velocities for particles with large St are probably not completely converged, because the simulation ran only 2π times their friction time $\tau_f = 100\Omega^{-1}$.

3.7   Discussion and Conclusions

3.7.1   Zonal Flows and Axisymmetric Pressure Bumps

My simulations have dimensionless units. This allows to interpret my results many-fold. One can pick the distance to the star in a certain range. In Section 3.1.4 I defined the global pressure gradient to be $\Delta v_p = 0.05c_s$. In the MMSN model one can choose the distance to the star to be between 0.35 and 40 AU (Hayashi, 1981). For this discussion, I pick $R = 5$ AU. In a thin disk model one gets a ratio for

---

[7]This corresponds to the analytical estimations using the measured u^{rms}. The factor between the analytical estimations using $u^{rms} = \sqrt{\alpha}c_s$ is 1.4 ± 0.3.

$H/R \sim 0.033(5\,\text{AU}/\text{AU})^{1/4} \sim 0.05$; this defines me $H = 0.25\,\text{AU}$. The isothermal sound speed is $c_\text{s} = H\Omega \sim 66{,}000\,\text{cm/s}$. Thus, turbulent velocities (u_rms) are about $9{,}000\,\text{cm/s}$ ($\sim 7{,}000\,\text{cm/s}$ for the high resolution run *LspecHR*).
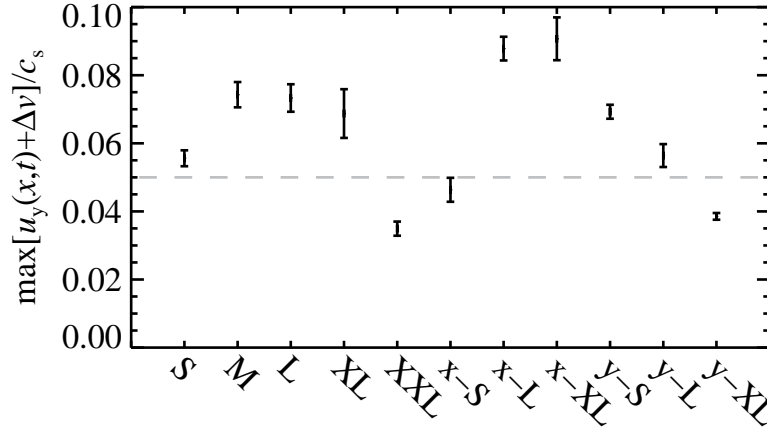
Figure 3.21 Measured highest azimuthal velocity of all box size simulated. The grey dashed line shows the threshold to Keplerian velocity. Only runs *XXL* and *y-XL* do never get super-Keplerian. Simulation *x-S* does get super-Keplerian at some time, but not often enough to be significant.

Figure 3.21 shows the highest azimuthal velocity for all simulation sizes. I averaged over several maxima of $u_y(x,t)$ for every simulation to smooth over outliers. The zonal flows are super-Keplerian for all but runs *XXL*, *x-S*, and *y-XL*. In the largest box the flow only reaches slightly sub-Keplerian velocities. However, particles still get captured in the resulting axisymmetric pressure bumps. The speeds measured in the largest simulation match those measured in Flock et al. (2011).

I measured the radial size of the axisymmetric pressure bumps to be between 5 and 7H (see Figure 3.7). At a distance of 5 AU to the star, this size corresponds to $\sim 1.25 \ldots 1.75\,\text{AU}$ radial size for zonal flows, i.e., the distance between peaks of $\langle \rho \rangle_{yz}$. This measurement agrees well with Simon et al. (2012) who measured the radial size of their zonal flows to be 6H. Further studies with varying box size in smaller steps could potentially narrow down the radial scale.

I measured the life times of the zonal flows up to 50T_orb. This agrees well with earlier stated life times (Johansen et al., 2009a; Uribe et al., 2011). The strength of the density bump reaches 15% and goes down to about 10% in the largest simulation. The lower amplitude is consistent with the results from global simulations (private communication with Mario Flock about the simulations from Flock et al., 2011, 2012) who measured a density enhancement of slightly less than 10%. Some works (e.g., Uribe et al., 2011; Simon et al., 2012) measure stronger density enhancements. A possible explanation is that their α values are higher than in this work. Further studies on the dependence of volume average quantities to strength of zonal flows would be interesting.

3.7.2   Dust in Zonal Flows

Particles get trapped downstream of pressure bumps and build up over-densities. To compare my dimensionless particle sizes with collision experiments and observations one has to assume a distance to the star and pick a solar system model. This allows to discuss my results in context to recent experiments.
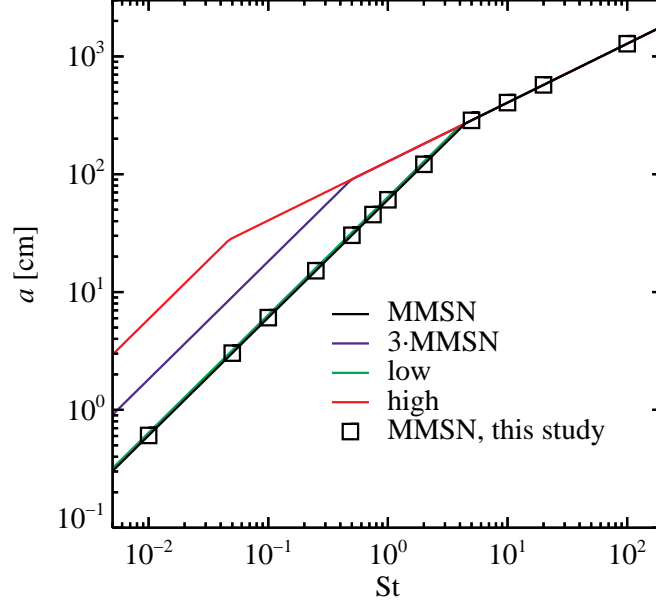
Figure 3.22 Particle sizes as a function of the dimensionless Stokes number for the four discussed models at 5 AU. The black squares show the used Stokes numbers and their corresponding size in the case of the Minimum Mass Solar Model.

By choosing a model for the solar system, one can convert the dimensionless Stokes number $\text{St} = \tau_f \Omega$ to a real particle size. The friction time τ_f correlates to the particle radius s with

$$s = \frac{\tau_f^{(\text{Ep})} \Omega \Sigma}{\sqrt{2\pi} \rho_\bullet} \, , \tag{3.28}$$

for Epstein drag and

$$s = \sqrt{\frac{9 \tau_f^{(\text{St})} \Omega \mu H}{4 \rho_\bullet \sigma_{\text{mol}}}} \, , \tag{3.29}$$

for Stokes drag (see supplementary info for Johansen et al., 2007). Here Σ is the column density of the gas, $\rho_\bullet$ the density of solid material, $\mu = 3.9 \times 10^{-24}$ g is the mean molecular weight and $\sigma_{\text{mol}} = 2 \times 10^{-15}$ cm^2 is the molecular cross section of molecular hydrogen (Nakagawa et al., 1986; Chapman and Cowling, 1970).

The Epstein regime applies, if the particle radius a does not exceed $(9/4)$ (Weidenschilling, 1977a) of the gas mean free path

$$\lambda_{\text{mfp}} = \frac{\mu}{\rho \sigma_{\text{mol}}} = \frac{\sqrt{2\pi} \mu H}{\Sigma} \sigma_{\text{mol}} \, . \tag{3.30}$$

The gas density, and hence also the particle size for a given Stokes number $St = \tau_f \Omega$ depends very much on the used model. Figure 3.22 overviews four different models. The minimum mass solar nebula model (MMSN, Weidenschilling, 1977b; Hayashi, 1981) was calculated from the mass of the existing planets, neglecting migration. Because this model allows no mass loss through accretion, often $3 \cdot$MMSN is used to account for some accretion. A low density model was published by Brauer et al. (2008). This model is adopted from measurements that indicate a shallow surface density profile for protoplanetary disks (Andrews et al., 2010). The high density model was adopted from Desch (2007), who introduced a "revised MMSN model" by using the starting positions in the Nice model of planetary dynamics (Tsiganis et al., 2005). This model also takes planetary migration into account. The equations used to calculate the particle sizes in Figure 3.22 are

$$\Sigma_{\mathrm{gas}} = \begin{cases} 1700 \frac{\mathrm{g}}{\mathrm{cm}^2} \left(\frac{r}{\mathrm{AU}}\right)^{-1.5} \text{ (MMSN)} \\ 5100 \frac{\mathrm{g}}{\mathrm{cm}^2} \left(\frac{r}{\mathrm{AU}}\right)^{-1.5} \text{ } (3 \cdot \text{MMSN}) \\ 683 \frac{\mathrm{g}}{\mathrm{cm}^2} \left(\frac{r}{\mathrm{AU}}\right)^{-0.9} \text{ (low density)} \\ 51{,}000 \frac{\mathrm{g}}{\mathrm{cm}^2} \left(\frac{r}{\mathrm{AU}}\right)^{-2.2} \text{ (high density)}. \end{cases} \tag{3.31}$$

Throughout the discussion I assume the MMSN model at 5 AU distance to the star for size reference for my test-particles. This choice affects only the translation from the Stokes number St to a size, not the dynamics in my models.

If the local dust density exceeds the Roche density, a clump is gravitationally bound against shear. The Roche density can be approximated (Kopal, 1989) by

$$\rho_{\mathrm{Roche}}(R = 5\,\mathrm{AU}) = \frac{9}{4\pi} \frac{\Omega^2}{G(R = 5\,\mathrm{AU})} \sim 100\rho(R = 5\,\mathrm{AU}), \tag{3.32}$$

for a MMSN. G is the gravitational constant. The streaming instability (Youdin and Johansen, 2007; Johansen and Youdin, 2007) starts to act at dust-to-gas ratios of order unity. I started all my simulations with $\epsilon_0 = \rho_p(t = 0)/\rho = 0.01$. Thus, a concentration of $\max(n_p)/\langle n_0 \rangle = 100$ corresponds to $\epsilon_{\mathrm{streaming}} = 1$. The Roche density at 5 AU in a MMSN can be expressed as $\epsilon_{\mathrm{Roche}} = \rho_{\mathrm{Roche}}/\rho \sim 100$. One can see that objects of several decimeters up to some meters reach $\epsilon_{\mathrm{Roche}}$, while pebbles of some centimeters up to a decimeter reach $\epsilon_{\mathrm{streaming}}$ from combining Figures 3.17 and 3.22. The concentration factors of run *LspecHR* in the right panel of Figure 3.17 show me that with an initial dust-to-gas ratio of $\epsilon_0 = 10^{-2}$ particles of sizes $St = 0.5 \ldots 10$ $(St = 0.1 \ldots 0.25)$ reach a dust-to-gas ratio of 100 $(\gtrsim 1)$. These sizes translate to $30 \ldots 400\,\mathrm{cm}$ $(6 \ldots 15\,\mathrm{cm})$ in a MMSN at a 5 AU orbit using Figure 3.22. Considering back-reaction from the dust to the gas would allow the streaming instability to act. This will be subject of a future study. In my simulations, I see that the density of $15 \ldots 600\,\mathrm{cm}$ sized icy boulders increases several thousand times over the equilibrium density, even without streaming instability and self-gravity of the particles. Sedimentation to the mid-plane leads to over-densities of around 40, while the contribution from the turbulence concentrates the boulders several hundred times.

Since I do not study the influence of the back-reaction from particles to the gas, I was able to study several particle sizes in one simulation. That also means that the initial dust-to-gas ratio (ϵ_0) can be set arbitrary. One can interpret my results in

the light of different metalicities. Particles with St $\geq$ 0.5 will trigger the streaming instability even with $\epsilon_0 = 10^{-4}$, while St $= 0.1$ particles need $\epsilon_0 = 10^{-2}$.

At the assumed distance in this discussion, the resulting rings of trapped dust are not observable with current telescopes. If zonal flows form at larger distances to the star and dust rings form at an observable size, they could potentially be observable with ALMA. For an analysis one would have to adjust the parameter Δv_p to account for the steeper pressure gradient. A preliminary study showed that particles of about 10 cm in size can get capture for a short amount of time at 100 AU distance. However, this question goes beyond the scope of this work and should be addressed in a future study.

Chapter 4

Particle Clouds in Zonal Flows

In the previous chapter I have shown that zonal flows are able to trap dust particles efficiently. This chapter focuses on the interaction of the formed dust particle clouds and the ambient gas. I performed three high-resolution simulations with back-reaction from the particles to the gas. In one of them, I additionally turned on self-gravity to follow the formation of planetesimals and measure an initial mass function. I chose to use the already converged run L ($5.28H \times 5.28H \times 2.64H$). This choice is a trade-off between simulation box size and computational expense.

4.1 Simulation Setup

I used the standard ideal magneto-hydro dynamics (MHD) equations (compare Section 3.1) with the two following additions. For the back-reaction from the particles to the gas, the term $\epsilon / \tau_f [v^{(i)} - u(x^{(i)})]$ is included to the equation of motion (equation (3.1)). Self-gravity is added with the term $-\nabla \Phi$ in the equation of motion and $-\nabla \Phi(x^{(i)})$ in the dust particle equation of motion (equation (3.11)). The gravitational potential Φ is calculated by using the Poisson equation

$$\nabla^2 \Phi = 4\pi G(\rho + \rho_p),\tag{4.1}$$

where G is the gravitational constant.

Thus, the full equation of motion for the gas in the simulations in this chapter is

$$
\begin{aligned}
\frac{\partial u}{\partial t} + (u \cdot \nabla) u + u_y^{(0)} \frac{\partial u}{\partial y} &= 2\Omega u_y \hat{x} - \frac{1}{2}\Omega u_x \hat{y} + \Omega^2 z \hat{z} + \frac{1}{\rho} J \times B - \frac{1}{\rho}\nabla P \\
&\quad - \nabla\Phi - \frac{\epsilon}{\tau_f}\left[u(x^{(i)}) - v^{(i)}\right] + f_\nu(u, \rho).
\end{aligned}\tag{4.2}
$$

The continuity equation (equation (3.3)), the induction equation (equation (3.2)), the equation of state $P = \rho c_s^2$, and the dissipation equations (equations (3.4)–(3.8)) are unchanged from Section 3.1. The velocity of the dust particles is advanced as

$$\frac{dv^{(i)}}{dt} = 2\Omega v_y^{(i)}\hat{x} - \frac{1}{2}\Omega v_x^{(i)}\hat{y} - \Omega^2 z\hat{z} - \nabla\Phi - \frac{1}{\tau_f}\left[v^{(i)} - u(x^{(i)})\right].\tag{4.3}$$

59

Table 4.1 Run parameters

Run	$L_x \times L_y \times L_z$	$N_x \times N_y \times N_z$	$\nu_3 = \eta_3 = D_3$	$n_{\text{particles}}$	St	ϵ_0	Δt
(1)	(2)	(3)	(4)	(5)	(6)	(7)	(8)
HRsolar	$5.28 \times 5.28 \times 2.64$	$512 \times 512 \times 256$	7.0×10^{-13}	44,949,246	0.1	0.01	68
HR0.1solar	$5.28 \times 5.28 \times 2.64$	$512 \times 512 \times 256$	7.0×10^{-13}	44,949,246	0.1	0.001	48
HRSG	$5.28 \times 5.28 \times 5.28$	$512 \times 512 \times 512$	1.0×10^{-12}	150,000,000	0.1	0.01	51

Notes. Column (1): name of run. Column (2): box size in units of pressure scale heights. Column (3): grid resolution. Column (4): dissipation coefficients. Column (5): number of particles in simulation. Column (6): Stokes number St $= \tau_f \Omega$. Column (7): initial dust-to-gas ratio. Column (8): total run time in orbits T_{orb}.

The particle position is evolved as before (equation (3.10)).

The simulations use the same shear-periodic boundary conditions (Section 3.1.3) and units (Section 3.1.4) as before. The initial conditions are like in Section 3.1.6, while particle feedback to the gas and (if applied) self-gravity start after $20T_{\text{orb}}$.

The run parameters are summarized in Table 4.1. All simulations were performed at the JUQUEEN supercomputer in Jülich. The runs *HRsolar* and *HR0.1solar* used 4,096 computer cores and run *HRSG*[1] used 8,192 CPUs.

4.2 Zonal flows

In the high resolution simulations of this chapter the zonal flows and the resulting pressure bumps are present. This is evident in the space time contour plots in the left panel of Figure 4.1. The radial size of the axisymmetric pressure bump is $\sim 5H$ as in Chapter 3. The amplitude of the pressure bump is strongest for run *HRSG*. It seems that the high dust-to-gas ratios do not effect the pressure bumps. However, the runs are not yet very far evolved. Thus, any estimation for the life-time of the zonal flows in these simulation is not meaningful. Turbulence parameters such as kinetic energy or the turbulent $\alpha = 2/3 \left(\langle \rho u_x u_y \rangle - \langle B_x B_y \rangle \right) / \langle P \rangle$ are shown in Table 4.2.

Table 4.2 Turbulence properties

Run	$\langle \frac{1}{2} u_x^2 \rangle$	$\langle \frac{1}{2} u_y^2 \rangle$	$\langle \frac{1}{2} u_z^2 \rangle$	$\langle \frac{1}{2} B_x^2 \rangle$	$\langle \frac{1}{2} B_y^2 \rangle$	$\langle \frac{1}{2} B_z^2 \rangle$	$2/3 \langle \rho u_x u_y \rangle$	$2/3 \langle -B_x B_y \rangle$	α
(1)	(2)	(3)	(4)	(5)	(6)	(7)	(8)	(9)	(10)
HRsolar	1.8×10^{-3}	3.6×10^{-3}	9.6×10^{-4}	8.7×10^{-4}	4.7×10^{-3}	4.0×10^{-4}	3.8×10^{-4}	1.7×10^{-3}	2.1×10^{-3}
HR0.1solar	1.9×10^{-3}	3.9×10^{-3}	9.5×10^{-4}	8.6×10^{-4}	4.5×10^{-3}	3.9×10^{-4}	3.9×10^{-4}	1.7×10^{-3}	2.1×10^{-3}
HRSG	1.1×10^{-2}	2.2×10^{-2}	6.6×10^{-3}	1.9×10^{-3}	9.7×10^{-3}	1.0×10^{-3}	6.4×10^{-4}	3.2×10^{-3}	3.9×10^{-3}

Notes. Column (1): name of run. Column (2-4): Kinetic energy. Column (5-7): Magnetic energy. Column (8): Reynolds stress. Column (9): Maxwell stress. Column (10): α-value, following equation (3.19). Stresses and energies have been normalized to the mean thermal pressure in the box, $\langle P \rangle = c_s^2 \langle \rho \rangle$.

---

[1]*HR* is short for high resolution; *solar* and *0.1solar* refer to solar metalicity and 10% of the solar metalicity respectively; *SG* is short for self-gravity.
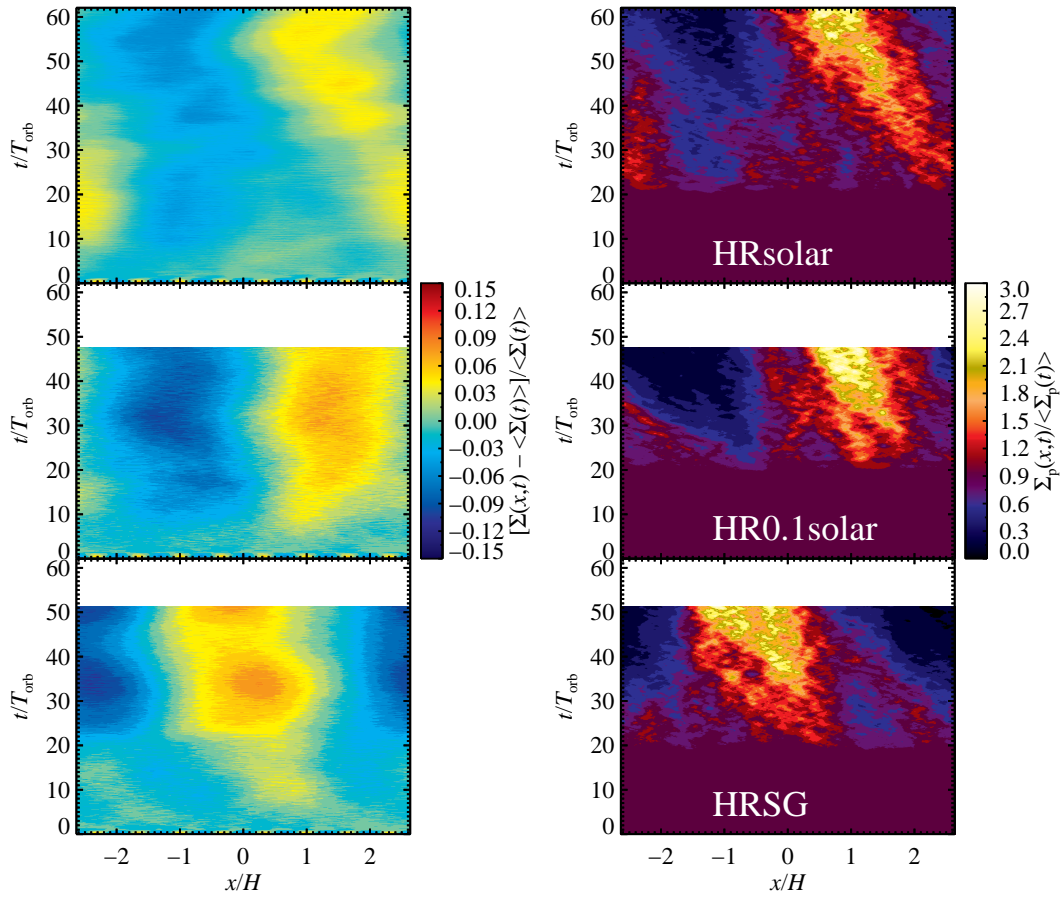
Figure 4.1 The left panels show the azimuthally and vertically averaged deviation from the mean gas density from all runs in this chapter as a function of time. The right panels display the dust density, averaged in azimuthal and vertical direction as a function of time for the same simulations. The white parts in runs *HR0.1solar* and *HRSG* show not yet executed times of the simulations. The dust density gets enhanced at the position of the pressure bump for all simulations.

4.3 Secondary Instabilities

In simulations with particle feedback on the gas one expects to trigger the streaming instability if the dust-to-gas ratio can be locally enhanced to order unity (Johansen and Youdin, 2007). The results from my simulations are discussed in Section 4.3.1. Gravitational collapse can happen if the particle density gets higher than the Roche density (equation (3.32)), the cloud will collapse to bound objects. The corresponding results are in Section 4.3.2.

4.3.1   Streaming Instability

The right coloumn of panels shows the dust density averaged in vertical and azimuthal direction of the same simulation. The density gets enhanced in the region of the pressure bump as evidence of particle capture. In these units the runs *HRsolar* and *HR0.1solar* have similar values, since they are normalized to the initial particle density.
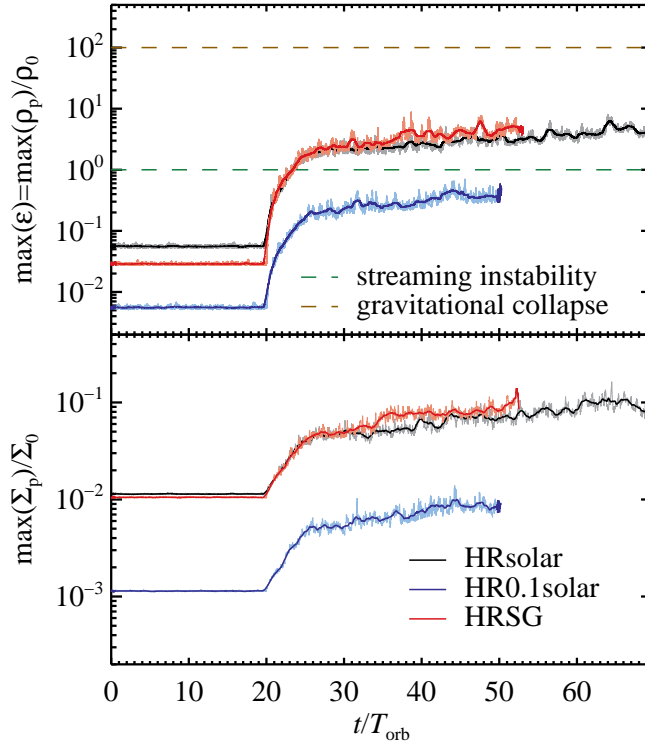
Figure 4.2 The upper panel shows the maximum of the dust-to-gas ratio ϵ in run *HRsolar* (black), run *HR0.1solar* (blue), and run *HRSG* (red) as a function of time. The lower plot shows the maximum of the dust surface density as a function of time. The light lines show the measurement at a higher time resolution, while the dark line show a temporal average over one orbit each. In all runs, particles are turned on after $20 T_{\mathrm{orb}}$. In runs *HRsolar* and *HRSG* ϵ gets larger than 1 and reaches similar densities like Johansen and Youdin (2007) in their 3D runs.

The streaming instability will start to act efficiently at a dust-to-gas ratio (ϵ) around unity (Johansen and Youdin, 2007). The maximum measured ϵ is shown in Figure 4.2. The particles settle to the midplane and are captured by the pressure bumps. In run *HRSG* the $\max \epsilon$ starts at a slightly lower value than in run *HRsolar* because the domain is more extended in the vertical direction. The dust-to-gas ratios gets well above 1 for runs *HRsolar* and *HRSG* and reaches values similar to run *AB-3D* in Johansen and Youdin (2007). In run *HR0.1solar* ϵ gets close to unity, but likely never triggers the SI. The dust-to-gas ratio in run *HR0.1solar* never gets larger than 1 and the streaming instability is not triggered.
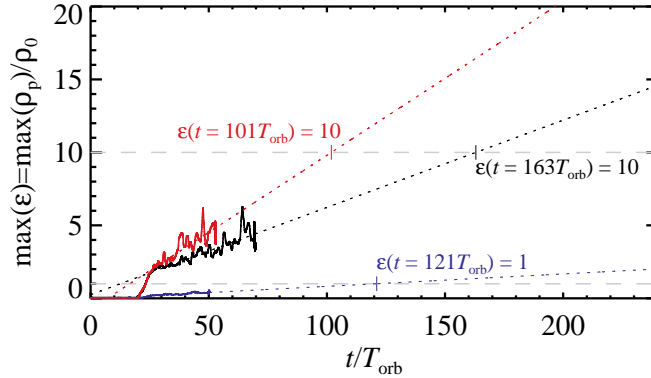
Figure 4.3 This plot shows the dust-to-gas ratio of all runs with the same color key as before (Figure 4.2). The grey lines show $\epsilon = 1$ as the trigger for SI and $\epsilon = 10$ to guide to eye. The function $\epsilon(t)$ is extrapolated, assuming a constant slope. With this extrapolation, one can assume that in run *HR0.1solar* the SI will trigger after $\sim 120 T_{orb}$.

Figure 4.2 suggests that $\max(\epsilon)$ has not converged in any of my simulations. Thus, one can fit their evolution after the sedimentation, i.e., $\sim 25 T_{orb}$, and extrapolate further development of $\max(\epsilon)$. This extrapolation is shown in Figure 4.3. For the sake of the argument, I assume the SI will only be triggered at $\epsilon = 1$ and the slope of $\max(\epsilon)$ does not change. The SI will trigger after $\sim 120 T_{orb}$ in run *HR0.1solar*. Figure 4.3 also shows that run *HRSG* with self-gravity grows faster than run *HRsolar* without self-gravity.

4.3.2 Gravitational Collapse

According to Kopal (1989), gravitational collapse happens when the local dust-to-gas ratio $\epsilon = \rho_p/\rho$ exceeds $\epsilon_{Roche} = 100$ at $R = 5\,\text{AU}$. The maximum to the local dust-to-gas ratio in run *HRSG* is shown as the red line in Figure 4.2. The value for $\max(\epsilon)$ reaches values up to ~ 5, well below ϵ_{Roche}. The extrapolation in Figure 4.3 would reach ϵ_{Roche} after $\sim 950 T_{orb}$ for run *HRSG*.

The dust surface density at $t = 52.3 T_{orb}$ in run *HRSG* is shown in Figure 4.4. It shows clearly that the dust particles get concentrated where the pressure bump is expected to capture the dust (compare with the lower left panel in Figure 4.1). The dust gets concentrated to more than 10 times its initial surface density. The clumps formed look similar to bound clumps in snapshots, but are sheared apart very quickly.

The main reason why there is no collapse is the low resolution compared to streaming instability studies in, e.g., Johansen et al. (2009b). In the next chapter, I will increase the resolution and take a simplified version of the clumps that formed in run *HRSG*. I investigate what happens when a sphere of dust particles with different initial dust-to-gas ratios experiences shear, friction with gas, and self-gravity.
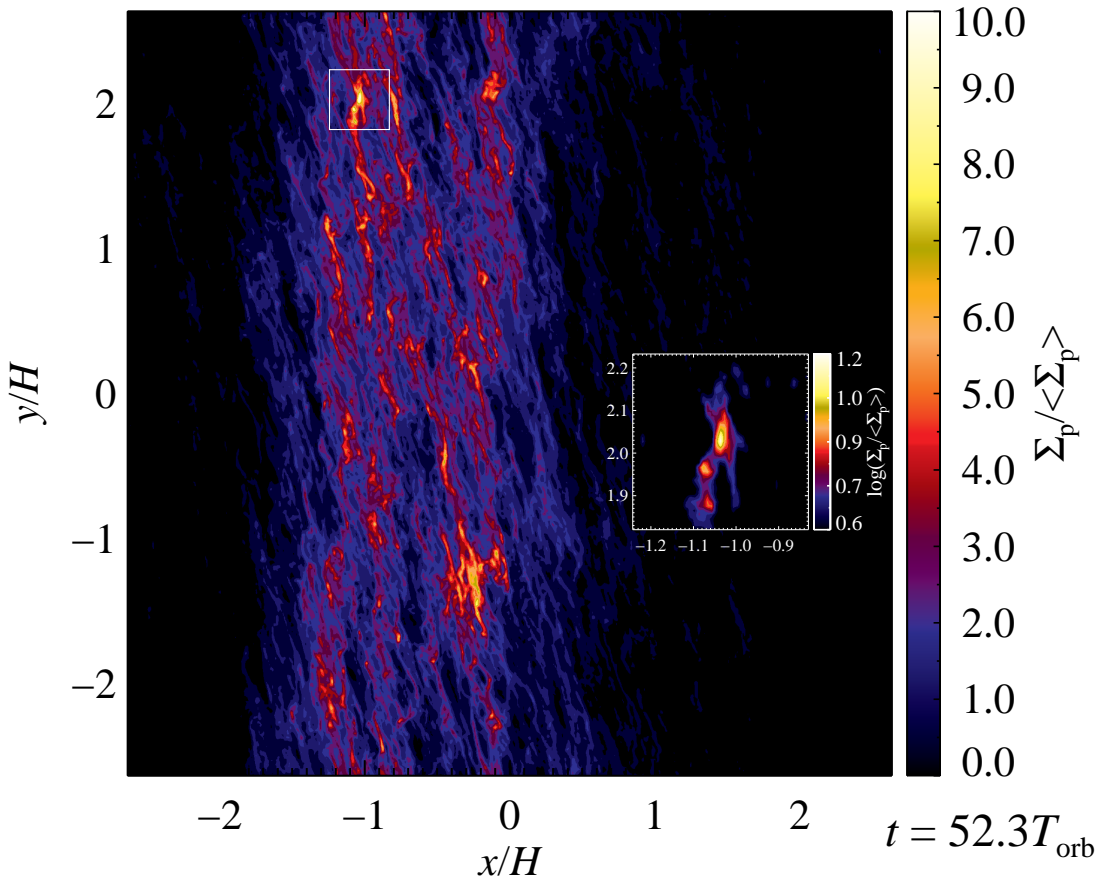
Figure 4.4 The main panel shows the dust surface density of run *HRSG* at $t = 52.3T_{\mathrm{orb}}$ in a linear scale. The inset panel shows the boxed region in a logarithmic scale around the highest density grid cell. The dust concentrates in the region of the axisymmetric pressure bump (compare bottom left panel in Figure 4.1). The dust surface density gets enhanced up to a factor of around 10. The clumps are well below the Roche density ($\epsilon_{\mathrm{Roche}} = 100$) and are likely not bound.

Chapter 5

Detailed study of Cloud Collapse

In order to simulate zonal flows, one has to increase the domain size compared to previous works (e.g., Johansen et al., 2007, 2011). This caused a strong decrease of resolution. One cannot hope to achieve a similar resolution and still use a box size that is necessary to fully simulate zonal flows. Thus, I perform simulations of a spherical dust cloud in a gaseous environment. The contents in this chapter are partly taken from a paper draft.

5.1 Simulation Setup

The simulations in this chapter use all gas and particle interactions that were introduced before. The magnetic field is neglected, because the dynamic is dominated by the dust particle and their interaction with the gas.

The runs are simulating the gas with the momentum equation as in equation (4.2) and the continuity equation as in equation (3.3) with the dissipation terms as in Section 3.1.2. Particles as super-particles are simulated as in equation (3.10) and

$$
\begin{aligned}
\frac{d\boldsymbol{v}^{(i)}}{dt} &= 2\Omega v_y^{(i)}\hat{\boldsymbol{x}} - \frac{1}{2}\Omega v_x^{(i)}\hat{\boldsymbol{y}} - \Omega^2 z\hat{\boldsymbol{z}} - \boldsymbol{\nabla}\Phi - \frac{1}{\tau_f}\left[\boldsymbol{v}^{(i)} - \boldsymbol{u}(\boldsymbol{x}^{(i)})\right] \\
&\quad - \frac{1 - C_{\text{res}}}{\tau_{\text{coll}}}\left(\boldsymbol{v}^{(i)} - \bar{\boldsymbol{v}}^{(m)}\right),
\end{aligned}
\tag{5.1}
$$

similar to equation (4.3). The last term in equation (5.1) describes the decrease of the velocity of particle i by collisional cooling (supplementary information of Johansen et al., 2007) in grid cell m with the mean particle velocity $\bar{v}^{(m)}$. The coefficient of restitution $C_{\text{res}} = 0.1$ is chosen, as in Johansen et al. (2007), to account that 90% of the relative velocity is lost in a typical collision between solid objects (Hartmann, 1985). The collisional time-scale

$$
\tau_{\text{coll}} = \frac{\tau_f}{(c_p/c_s)\,(\rho_p/\rho)},
\tag{5.2}
$$

where c_p is the velocity dispersion of the particles, follows a scaling with the Epstein friction time τ_f as in Johansen et al. (2007).

Table 5.1 Run parameters

Run	Back-reaction	Cooling	$\rho_p/\rho_{\mathrm{Roche}}$	ϵ_0	St	m
(1)	(2)	(3)	(4)	(5)	(6)	(7)
AA	x	x	1	100	1	13.279
AB	x	x	1	100	0.1	13.279
BA	x	x	0.1	10	1	1.328
BAHR	x	x	0.1	10	1	1.328
BB	x	x	0.1	10	0.1	1.328
BB1	-	x	0.1	10	0.1	1.328
BB2	-	-	0.1	10	0.1	1.328
BAB	x	x	0.1	10	1, 0.1	1.328
CA	x	x	0.01	1	1	0.133
DA	x	x	0.001	0.1	1	0.013

Notes. Column (1): name of run. Column (2): indication whether back-reaction is turned on (x) or off (-). Column (3): indication whether collisional cooling is turned on (x) or off (-). Column (4): initial dust density in the particle sphere in terms of Roche density $\rho_{\mathrm{Roche}} = 100\rho_0$ at $R = 5\,\mathrm{AU}$. Column (5): initial dust-to-gas ratio in the particle sphere. Column (6): Stokes number $\mathrm{St} = \tau_f\Omega$. Column (7): total dust mass in units of the mass of the dwarf planet Ceres M_{Ceres}.

The equation of state is isothermal, i.e., $P = \rho c_s^2$. The boundary conditions are shear-periodic in radial direction and periodic in the azimuthal and vertical direction. All simulation boxes have a size of $(0.4H)^3$ and most are simulated with 288^3 grid cells. The resolution is $L_x/N_x = 1.4 \times 10^{-3}$[1] is an order of magnitude higher than the resolutions in the previous chapter. The high resolution run *BAHR* uses 576^3 grid cells and has a resolution of $L_x/N_x = 6.9 \times 10^{-4}$.

In the Poisson equation, $\nabla^2\Phi = 4\pi G(\rho + \rho_p)$, the gravitational constant G can be set in the PENCIL CODE by setting the parameter $c_{\mathrm{RHS}} = 4\pi G \cdot \Omega^2/\rho_0$. By setting c_{RHS}, one defines the density ρ_0. Also, because $\rho_0 = \Sigma_0(R)/(\sqrt{2\pi}H(R))$ it defines the distance to the star R and along with the used model for the protoplanetary disk. I used the parameter $c_{\mathrm{RHS}} = 0.1$. Thus, one can define the distance to the star if one assumes a disk model. For this chapter, I assume a 2.3·MMSN at $R = 5\mathrm{AU}$ distance to the star.

The gas density is uniform initially and the initial gas velocity is 0. Dust particle positions are initialized as a sphere of uniform density centered around the center of the simulation box. The sphere has a radius $r = 0.025H$. The initial particle velocity is $\boldsymbol{v} = (0, u_y^{(0)}(x), 0) + \boldsymbol{v}_{\mathrm{random}}(\Delta v_0)$, where the last term adds a random velocity with $\Delta v_0 = 0.01c_s$. Since the density in the particle sphere is changed while its size is kept constant, the total mass in the simulation changes. The initial dust density, the Stokes number of the particles, the total dust mass and whether back-reaction from dust to gas and collisional cooling are used is shown in the performed simulations are summarized in Table 5.1.

---

[1]This corresponds to a resolution of $\sim 50,000\,\mathrm{km}$ per grid cell.

Runs *AA* and *AB* show that the PENCIL CODE can simulate the gravitational collapse, when the dust density is about the Roche density $\epsilon_0 = \epsilon_{\text{Roche}} = 100$. The runs starting with *B* are simulations with $\epsilon_0 = 0.1\epsilon_{\text{Roche}} = 10$, a dust-to-gas ratio close to what was achieved in the last chapter. The two simulations were performed to check which ϵ is required to trigger a collapse to bound objects.

5.2 Results

5.2.1 Collapse to Bound Clumps

If the initial dust-to-gas ratio ϵ_0 is larger than $\epsilon_{\text{Roche}} \sim 100$ then the entire sphere should collapse into a single object. This is shown in Figure 5.1 for run *AA*. All particles collapse to a bound object with a size of one grid cell. The collapse seems to happen faster than one free fall time τ_{ff} because the grid resolution does not allow to follow the final collapse phase.
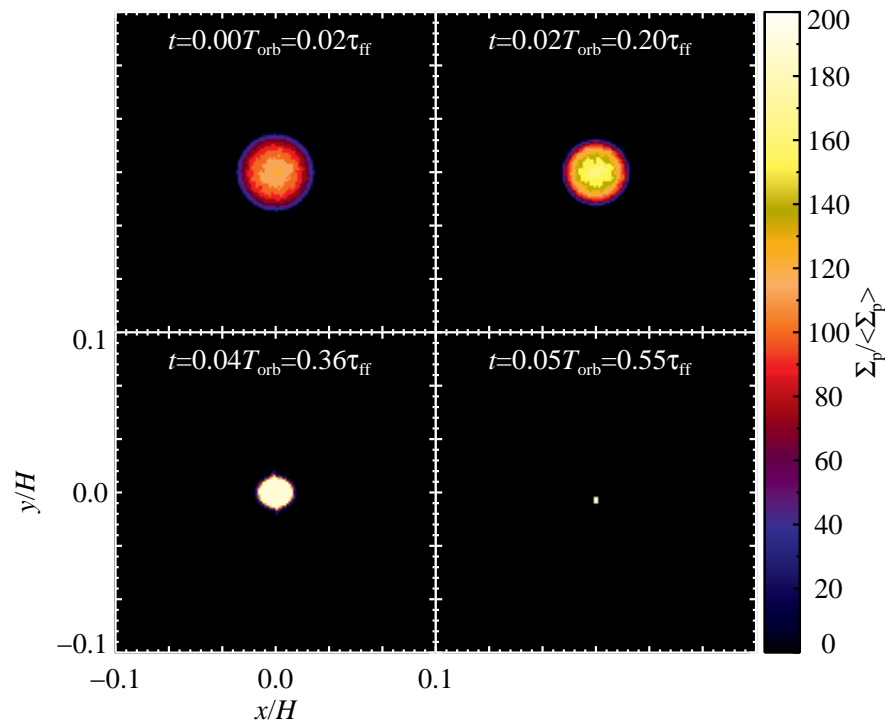
Figure 5.1 Dust surface density snapshots of run *AA* with $\rho_{\text{p}}(t = 0) = \rho_{\text{Roche}}$ and St = 1. All dust in this simulation collapses into a single planetesimal. The collapse time scale is much shorter than an orbital time scale. The collapse in run *AB* happens on a similar time scale.

Reducing the initial dust-to-gas ratio ϵ_0 to $0.1\epsilon_{\text{Roche}}$ does lead to fragmentation of the dust sphere. Figures 5.2, 5.4, and 5.6 show the evolution of the dust surface density for runs *BB1*, *BB2*, and *BAB* respectively.
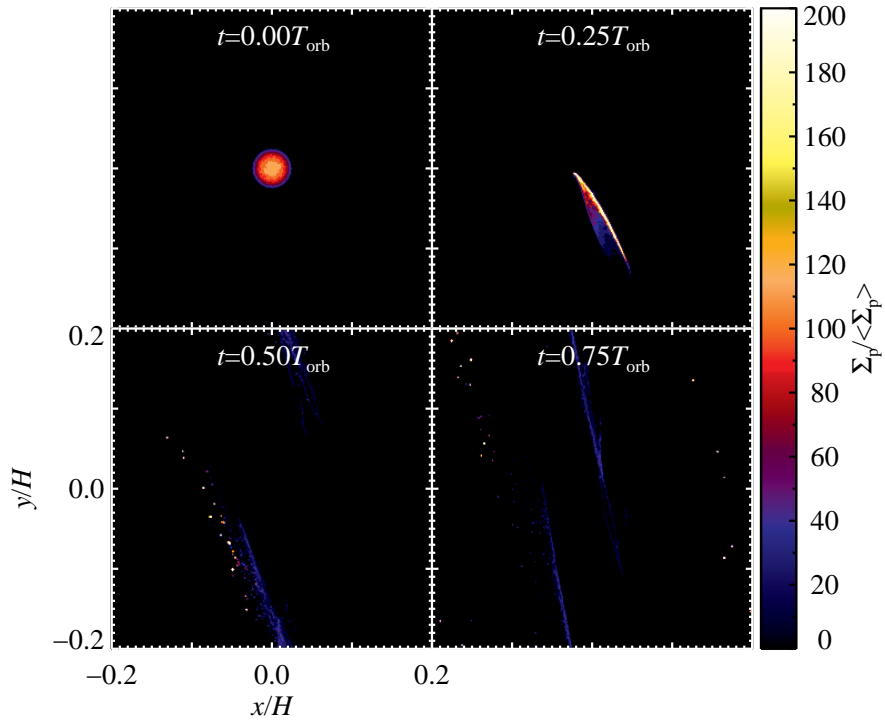
Figure 5.2 Dust surface density snapshots of run *BB1* with $\rho_{\mathrm{p}}(t=0) = 0.1\rho_{\mathrm{Roche}}$ and $\mathrm{St} = 0.1$. The back-reaction from the dust drag to the gas density is neglected for this run. The streaming instability cannot be triggered and some mass gets stripped from the sphere. At late times, clumps begin to form.
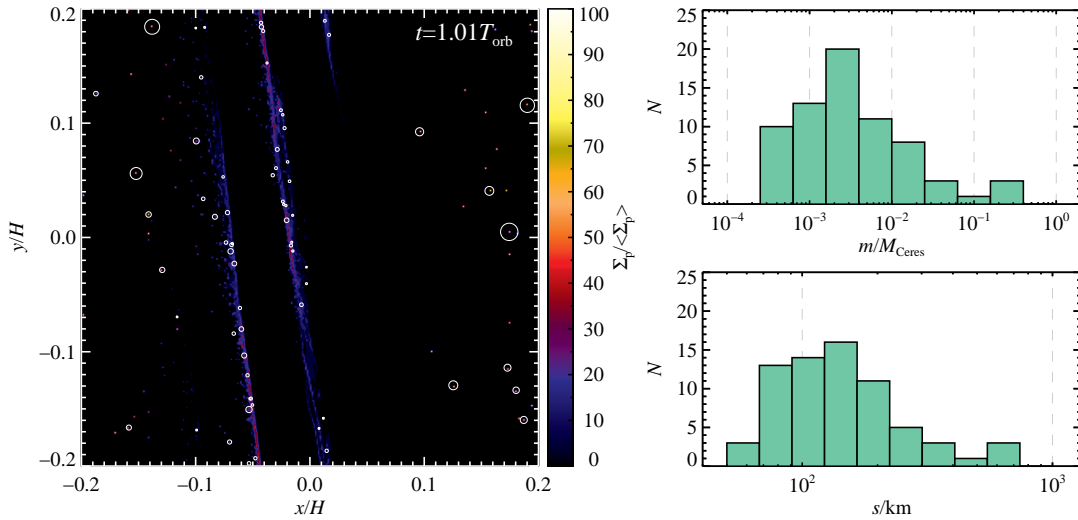
Figure 5.3 Dust surface density snapshot at the end of run *BB1*. This plot shows all 69 bound clumps and their hill spheres. The right panel shows the mass (top) and planetesimal size (bottom) distribution. The size distribution is calculated from the mass, using the density of the dwarf-planet Ceres.
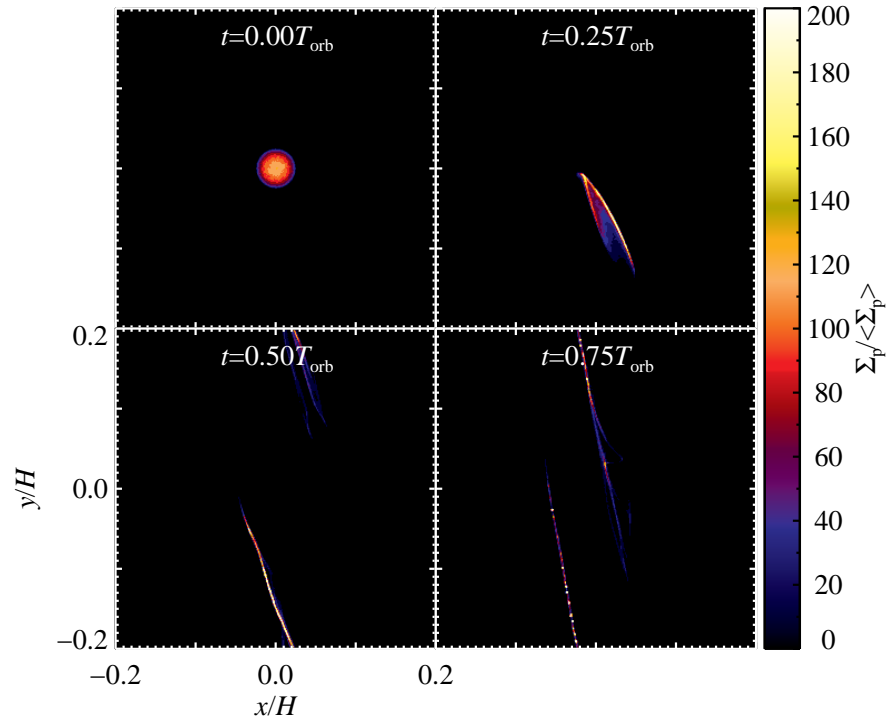
Figure 5.4 Dust surface density snapshots of run *BB2* with $\rho_\mathrm{p}(t=0) = 0.1\rho_\mathrm{Roche}$ and St $= 0.1$. The back-reaction from the dust drag to the gas density and collisional cooling are turned off in this run. The sphere gets stretched, but the forming clumps do not get separated from the density sheet.
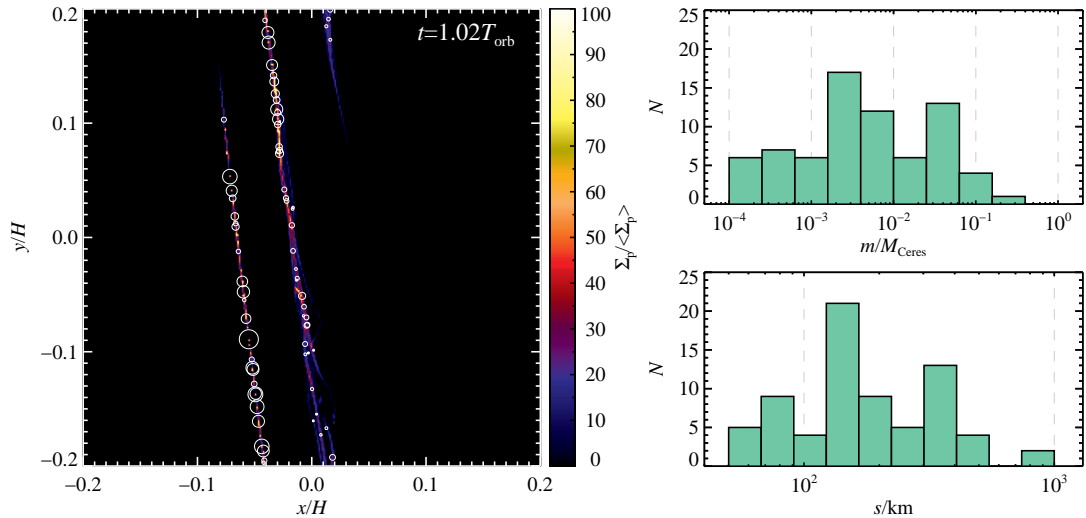
Figure 5.5 Dust surface density snapshot at the end of run *BB2*. This plot shows all 72 bound clumps and their hill spheres. The right panel shows the mass (top) and planetesimal size (bottom) distribution. The size distribution is calculated from the mass, using the density of the dwarf-planet Ceres.
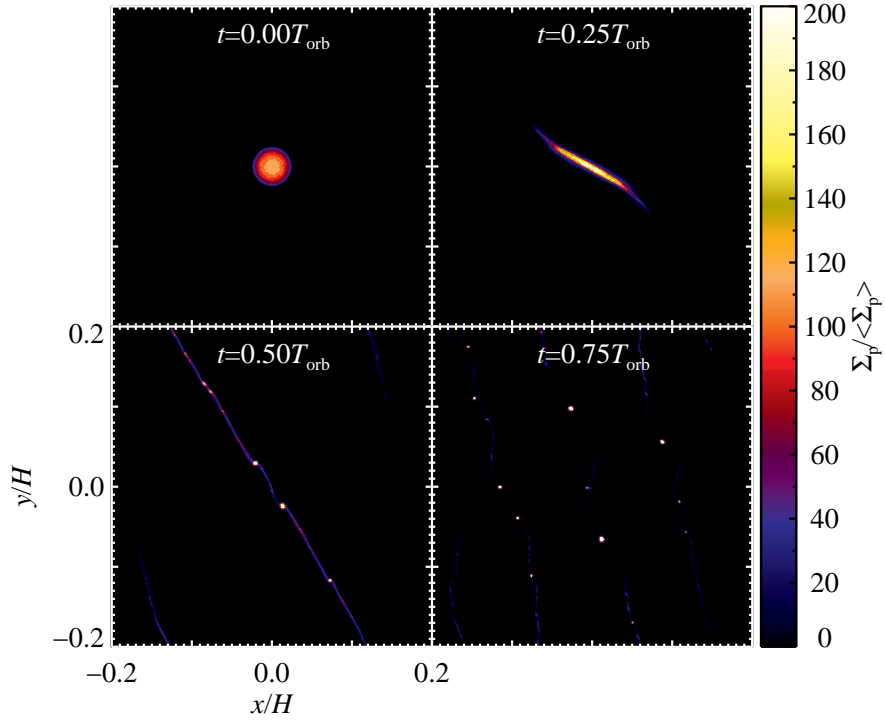
Figure 5.6 Dust surface density snapshots of run *BAB* with $\rho_p(t=0) = 0.1\rho_{\text{Roche}}$ and two different particle species: St $= \{1, 0.1\}$. The surface density shows both particle species. The clumps formed are initially similar to those in runs *BA* and *BB*, but the interaction between the particles of different sizes changes the late-time development.
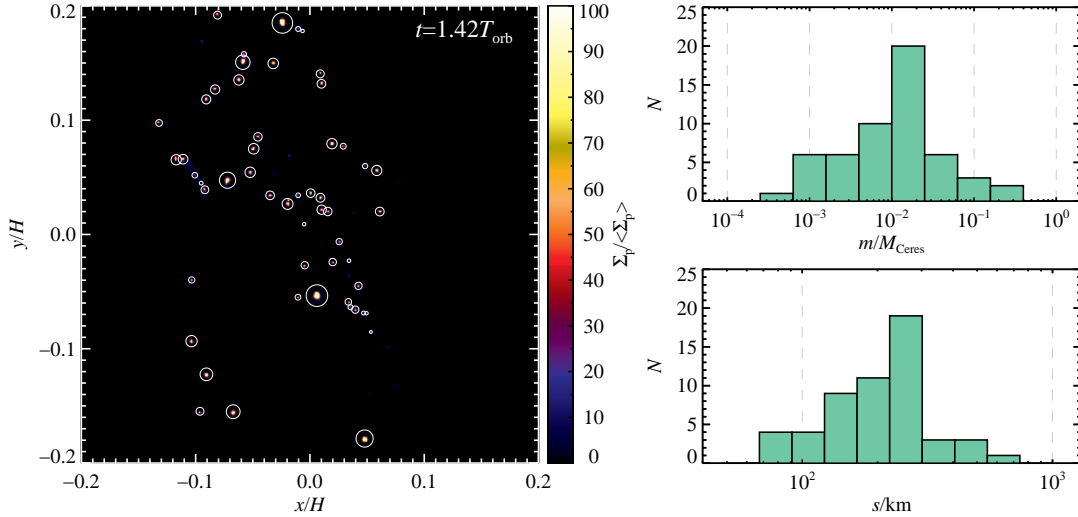
Figure 5.7 Dust surface density snapshot at the end of run *BAB*. This plot shows all 54 bound clumps and their hill spheres. The right panel shows the mass (top) and planetesimal size (bottom) distribution. The size distribution is calculated from the mass, using the density of the dwarf-planet Ceres.
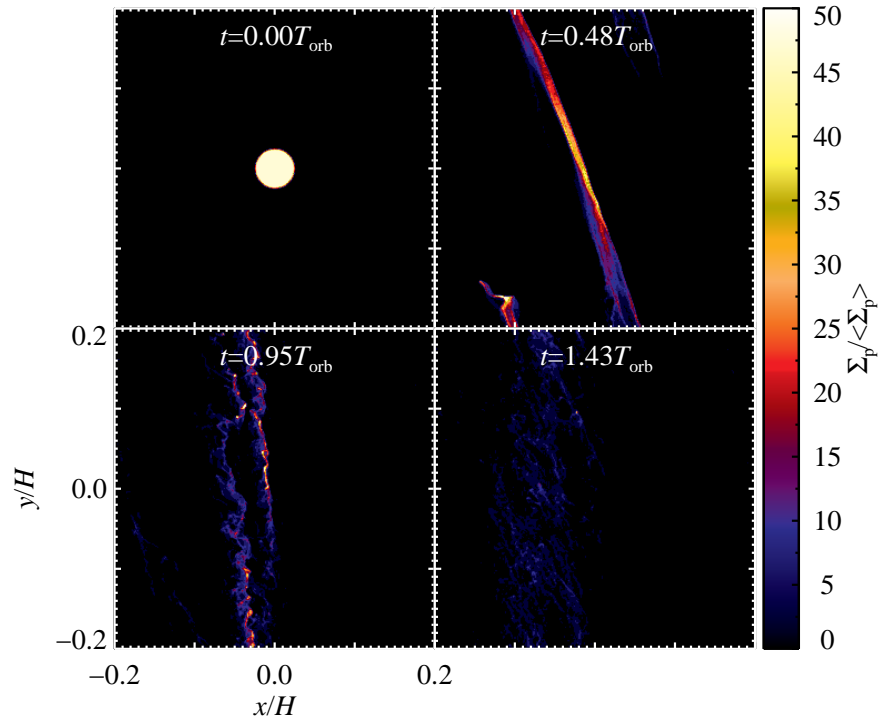
Figure 5.8 Dust surface density snapshots of run *CA* with $\rho_p(t=0) = 0.01\rho_{\text{Roche}}$ and St $= 1$. Note the different color scale to all previous dust surface density figures. Dust particles are distributed throughout the box. The sphere gets disrupted by shearing forces and the dust density drops well below its initial value.

Figure 5.2 (run *BB1*) shows the evolution of the dust surface density when the back-reaction from the dust particles to the gas is turned off. The sphere gets stripped of some mass, but most mass can be bound in small objects. A snapshot of the dust surface density after $1.01T_{\text{orb}}$ is shown in the left panel of Figure 5.3. Over-plotted are the hill spheres of all bound clumps. The right panels in Figure 5.3 show a mass and a size distribution of those clumps. The size here refers to the size these objects will have after their final collapse using the measured mass and the mean density of the dwarf-planet Ceres $\rho_{\text{Ceres}} = 2.077\,\text{g}\,\text{cm}^{-3}$ (Thomas et al., 2005). The mass distribution peaks between $10^{-3}M_{\text{Ceres}}$ and $10^{-2}M_{\text{Ceres}}$. Small objects are more common than larger ones. Clearly, the smallest objects are not resolved in the simulation.

The dust surface density evolution of run *BB2* is shown in Figure 5.4. Here, the back-reaction and collisional cooling are turned off. As in run *BB1* the sphere gets stretched into an elongated shape that eventually fragments and forms bound objects. The formed clumps and their mass and size distribution are shown in Figure 5.5. The distributions are much broader than the distribution for run *BB1* and there is no typical size for the formed objects. This shows that a proper treatment of collisions is important to reproduce a typical size for asteroids, as is observed.

Figure 5.6 shows the dust surface density evolution for run *BAB*, combining the dust sizes in runs *BA* and *BB*. The evolution is similar to any of the two runs with

one dust species. The last snapshot and the mass and size distribution are shown in Figure 5.7. The objects have a preferred mass of a few $10^{-2} M_{\text{Ceres}}$ and a preferred size of $\sim 250\,\text{km}$.

The objects with the lowest mass the simulations can resolve have

$$m_{\text{min}} \sim \left(\frac{L_x}{N_x} \right)^3 \rho_{\text{Roche}} = 5 \cdot 10^{-4} M_{\text{Ceres}} \,. \tag{5.3}$$

Thus, the mass distribution drops for masses below m_{min}. This corresponds to a final collapse size of $s_{\text{min}} \sim 80\,\text{km}$. The typical final collapse size of objects in my simulations is about a factor of 2 higher than s_{min}. Thus, the typical size is determined rather by a physical process than numerical resolution.

If the initial dust-to-gas ratio ϵ_0 gets decreased to unity (run *CA*) and below (run *DA*), the dust sphere gets disrupted by tidal forces. The dust surface density evolution is shown in Figure 5.8. The resulting sheets of dust never reach densities high enough to form bound objects.

5.2.2 Towards an Initial Size Distribution
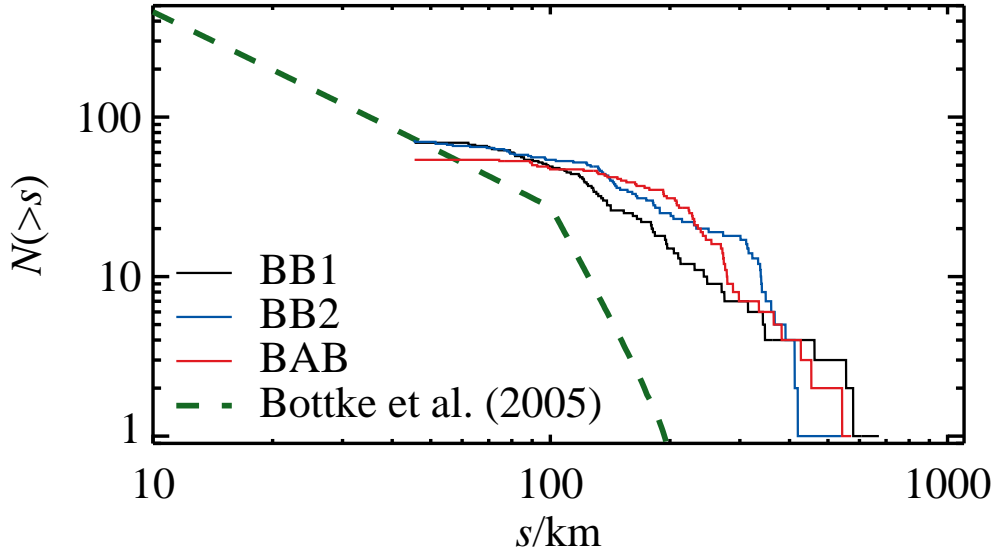
Figure 5.9 Cumulative size (diameter) distribution of the clumps in my simulations. The size distribution for run *BAB* has a knee at $s \sim 200\,\text{km}$. For comparison I show the initial cumulative size distribution of asteroids (Bottke et al., 2005) scaled to the number of objects in my simulations. The distributions are qualitatively similar in terms of slope for large objects and the presence of a knee in the distribution at a typical size.

In all simulations where fragmentation occurred, I measured the mass and size distribution of the bound objects. This distribution can be directly compared to observational data of the asteroid belt and the Kuiper belt. A comparison of the cumulative size distribution from my simulations and the observed one from Bottke et al.

(2005) is shown in Figure 5.9. Qualitatively, the distributions from my simulations and the observed distribution are similar in terms of slope and shape, i.e., both have a steep power law for high-mass objects and a shallow power law for low mass objects; run *BAB* also has a knee. The quantitative agreement in characteristic size is within a factor of 2. Future studies will have to show how this typical size depends on initial particle size distribution, gas density versus Roche density, and initial clump size and mass. Of course, my simulations lack completeness for the smaller objects, but the closest representation of the observed cumulative size distribution gives run *BAB*.

5.3 Conclusion

The results in this chapter show that it is possible to form bound objects of typical masses and final collapsed sizes similar to the observed masses and sizes in Kuiper and asteroid belt, as long as the particle density of the initial cloud is about $0.1\rho_{\mathrm{Roche}}$. Larger densities lead to a single large planetesimal consuming all available mass and a lower density does not lead to gravitational collapse. The simulations appear to be numerically resolved as the typical planetesimal mass is two orders of magnitude above the mass resolution of the numerical scheme. These simulations are numerically very expensive and it has not yet been possible to scan the parameter space in terms of particle size distributions, gas density versus Roche density, and initial clump size and mass. Nevertheless, the preliminary results are very promising and further studies are under way.

In order to simulate the collapse down to the final collapse size, one has to increase the resolution. Simulations using 2048^3 grid cells are possible on clusters such as JUQUEEN. One would need to start the simulation with a smaller dust cloud of $m = M_{\mathrm{Ceres}}$ and $r = R_{\mathrm{Hill}} = 5.8 \times 10^{-4} H$. The initial dust density can then be changed by initializing the radius of the dust sphere with factors of R_{Hill}. At asteroid belt location 2.5 AU this simulation would have a resolution of $\sim 17\,\mathrm{km}$ per grid cell.

Chapter 6

Discussion and Conclusion

This thesis studies numerically the formation of planetesimals in the gravoturbulent formation scenario. Methodological progress has been achieved in several ways:

- Possible code verification: by simulating typical laboratory setups of particle-gas mixtures I obtained data for future comparison with experiments, helping to understand the validity of our numerical approach.

- In contrast to previous work larger computational domains have been used, leading to a convergence of radial extent and life-time for particle concentrating zonal flows.

- Detailed high resolution runs on collapsing particle clouds allowed to study initial size distributions for planetesimals.

By these methods I was able to refine the gravoturbulent formation scenario in several ways.

- Even low abundances of small particles below the drift and fragmentation barrier can get concentrated sufficiently in zonal flows to trigger streaming instability and gravitational collapse.

- Typical concentration in large scale simulations, limited in resolution, lead to particle densities of $0.1\rho_{\mathrm{Roche}}$.

- Whereas concentrations at $\rho_{\mathrm{p}} = \rho_{\mathrm{Roche}}$ would lead to one single massive planetesimal and densities $\rho_{\mathrm{p}} \leq 0.01\rho_{\mathrm{Roche}}$ do not fragment at all, the observed density of $\rho_{\mathrm{p}} = 0.1\rho_{\mathrm{Roche}}$ leads to a narrow size distribution of many small planetesimals in the 100 km range.

6.1   Rayleigh-Taylor Instability in Dust-laden Fluids

During my thesis work, I studied the Rayleigh-Taylor instability (RTI) of a dust-laden fluid (Chapter 2). I verified that particles in the PENCIL CODE can sufficiently reproduce the typical velocities and length scales from the classical RTI. In order to follow

this in the simulated domain, one needs to use the appropriate particles friction times (that represent particle sizes) and resolution. The number of super-particles in the simulation need to exceed number of grid cells by about an order of magnitude in order to resolve structures such as RTI fingers.

The simulations with a random initial particle velocity can be compared with experiments and astronomical observations. The late-time evolution of the simulations can be compared to experiments of dust particles in a funnel flow.

6.2 Zonal Flows as Trigger for Planetesimal Formation

In Chapter 3 I performed numerical simulations of MRI-driven turbulence in shearing boxes, covering the parameter space for radial and azimuthal box sizes up to $21.12H$. Further, I followed the reaction of the dust particle density to the turbulence. My major findings are as follows.

1. Turbulent energy and stresses double when increasing the azimuthal size of the simulation from 1.32 to 2.64 pressure scale heights. Turbulence parameters in radially small box sizes stay approximately constant. This confirms the results in Fromang and Stone (2009). In larger boxes, turbulent fluctuations and stresses are observed to remain constant against changes in the box size (see also Johansen et al., 2009a). This rapid convergence was also observed in Simon et al. (2012).

2. Surface density fluctuations grow to large scales in the box and have life-times of up to 50 orbits. The scales of these pressure bumps increase with increasing radial box size, until it saturates at approximately 5 to 7 pressure scale heights. The scales are decreased when the azimuthal box size is much more increased than the radial box size. The radial scales of the pressure bumps are consistent with the length scales measured in local (e.g., Johansen et al., 2009a; Simon et al., 2012) and global (e.g., Lyra et al., 2008; Uribe et al., 2011) simulations. This might be the natural size of these over-densities. The pressure bumps are in geostrophic balance with sub- and super-Keplerian zonal flows. At 5 astronomical units distance to the star $6H$ correspond to ~ 1.5 AU. The amplitude of the density bump reaches 15% and goes down to about 10% in the largest simulation.

3. Particles with $\mathrm{St} = \tau_\mathrm{f}\Omega = 1$ are getting trapped efficiently by the axisymmetric pressure bumps. They accumulate in regions of minima in the second derivative of the gas density as predicted analytically (e.g., Klahr and Lin, 2001). The concentration factor correlates with the correlation time of the zonal flows. Hence, the first two steps of planetesimal formation[1] in protoplanetary disk with an acting MRI are: vertical settling via sedimentation and radial concentration by trapping of dust in axisymmetric pressure bumps. Further concentration comes likely from stochastic processes. Clustering properties do not depend strongly on strength or life-time of the zonal flows.

---

[1]After coagulation from μm-sized particles to $\mathrm{St} = 0.1, 1$.

4. My simulations reach dust-to-gas ratios of 50 to 100. These densities are of the order of the Roche density at 5 AU in a MMSN. The dust over-densities scale with the life-time of the zonal flow structures by a power law with an exponent of 0.38 ± 0.05 (see Figure 3.9). To what degree these high dust-to-gas ratios disturb the axisymmetric pressure bumps that developed in the zonal flows has to be investigated in further studies with back-reaction to the gas.

5. Particles of only a few centimeters in size (at 5 AU in a MMSN, St = 0.1) accumulate in over-densities that are increased by a factor of ~ 100, leading to a dust-to-gas ratio of 1 in the mid-plane, thus triggering the streaming instability. Without MRI and zonal flows St = 0.1 particles do not clump strongly and cannot trigger the streaming instability for solar metalicity $Z = \epsilon_0 = 0.01$ (Johansen et al., 2009b).

6. Measuring collision velocities for particles larger than St = 0.5 is possible in low-resolution numerical simulations. I measured the distribution of relative velocities and distances between particle pairs to estimate the collision velocity. I estimate the velocity distribution with a sum of a quasi-Maxwellian, a quasi-exponential, and a cluster function. The measured collision velocities are a factor 2.6 lower than the analytical estimation from Ormel and Cuzzi (2007). This factor is slightly lower than the factor 4 measured in Hubbard (2012).

This first work on the effect from large-scale zonal flows on dust particles in a MHD simulation was published in Dittrich et al. (2013). Dust gets trapped downstream of long-lived high-pressure regions and achieves over-densities that have the potential to generate streaming instability and to become gravitationally unstable.

Planetesimal formation in large boxes was investigated in simulations with particle feedback on the gas and self-gravitating particles in Chapter 4. I focused on one model and studied two different initial dust-to-gas ratios. The simulations showed, that dust particles with St = 0.1 gets concentrated sufficiently high to trigger the streaming instability if the initial dust-to-gas ratio is of solar metallicity. In a simulation with a lower (10% of the solar metallicity) initial dust-to-gas ratio, the dust density did not reach high enough values to trigger the streaming instability. However, the evolution of $\max\left(\rho_\mathrm{p}\right)$ for all simulations in Chapter 4 are not yet converged and the projected time at which also the low-metallicity simulation should converge is after $t = 121 T_\mathrm{orb}$. Clumps formed in the simulation with self-gravity, but they never reached densities higher than the Roche density. The typical over-densities were of order $0.1 \rho_\mathrm{Roche}$.

6.3 Initial Mass Function

In the last project (Chapter 5), I studied the gravitational collapse of a spherical dust cloud. The resolution in these simulations was an order of magnitude higher than in all other simulations in my work. My simulations showed that the collapse of spherical dust clouds with various initial dust-to-gas ratios up to bound clumps can be simulated with the current version of the PENCIL CODE.

I showed that the mass and size distribution depends on the initial dust-to-gas ratio of the dust spheres, on the consideration of physical effects such as back-reaction from the dust particles to the gas or the dynamical cooling of dust particles through collisions, and to a small degree on the size of the particles involved in the collapse. The last point needs to be investigated further in future studies. Here, one should consider a wider range of particle sizes and investigate the degree of interaction between particles of different sizes.

The simulated initial cumulative size distribution was compared with the observed cumulative size distribution of objects in the asteroid belt (Bottke et al., 2005). The distributions are very similar for large objects, while smaller objects cannot be resolved in my simulations.

6.4 Outlook

The study I intended for Chapter 4 was to cover the parameter range of particle sizes ($St = 0.1 \ldots 1$) and initial dust-to-gas ratio ($\epsilon_0 = 0.001 \ldots 0.01$) more thoroughly. The limited computation time and technical difficulties permitted no such study. Instead I could only perform the three simulations presented in this work. This set of simulations would provide more insight what initial dust-to-gas ratio and maximum particle size is sufficient to trigger streaming instability and gravitational collapse in a zonal flow simulation setup.

Resolution and its effects on the physical interpretation is always an issue with numerical simulations. However, the final collapse of a particle cloud to bound objects will soon be studied in simulations that resolve the internal structure of these objects. The resolution in my simulations is $\sim 50{,}000$ km per grid cell. Simulations using 2048^3 grid cells that start with a smaller dust cloud of $m = M_{\mathrm{Ceres}}$ and $r = R_H = 5.8 \times 10^{-4} H$ at asteroid belt location 2.5 AU have a resolution of 17 km. A test run with 1024^3 on JUQUEEN showed that such a simulation is possible. The PENCIL CODE will have to be adjusted by a pressure term for the dust particles to create solid structures. In a simulation with this resolution one could compare the internal structure of asteroids with numerical simulations.

6.5 Conclusive Remarks

From my results of the local numerical simulations, I propose the following steps from dust with a size distribution similar to Birnstiel et al. (2012) to gravitationally bound planetesimals of several kilometers in size.

1. Concentration in the vertical direction via sedimentation. Small dust particles are well distributed in the vertical direction. As they grow through collisional sticking, the bigger dust particles sediment to the mid plane. See the upper panel in Figure 3.19 for dust scale heights of different sized particles.

2. Concentration in the radial direction via zonal flows. In Chapter 3, I show that radially drifting dust particles get trapped by axisymmetric pressure bumps. The ring of high dust density can be very narrow and trigger further instabilities like the streaming instability (Section 4.3.1).

3. Concentration in the azimuthal direction via the non-axisymmetric modes of the streaming instability and stochastic processes. In all simulations I saw that thin high-density sheets of dust collide. These chance encounters caused very high dust densities, sufficient to trigger gravitational collapse. The simulations in Chapter 5 showed that densities lower than Roche density can lead to the formation of gravitationally bound planetesimals of typical size $\sim 200 \, \text{km}$.

In conclusion the result of this thesis is further support for the two-stage planetesimal formation scenario where coagulation produces the needed $\text{St} = 0.1$ particles and gravoturbulent fragmentation the observed abundance of 100 km-sized planetesimals.

Appendix A

Acronyms

This list of acronyms is sorted by the first appearance of the acronym.

Akronym	Explanation
RTI	**R**ayleigh-**T**aylor **i**nstability
UV	**U**ltra-**v**iolet
IR	**I**nfra-**r**ed
MRI	**M**agneto-**r**otational **i**nstability
WKB	**W**entzel, **K**ramers, and **B**rillouin
3D	**Three**-**d**imensional
MHD	**M**agneto-**h**ydro**d**ynamics
SI	**S**treaming **i**nstability
MPI	**M**essage **p**assing **i**nterface
2D	**Tow**-**d**imensional
KHI	**K**elvin-**H**elmholtz **i**nstability
FDA	**F**inite **d**ifference **a**dvection
SAFI	**S**hear **a**dvection by **F**ourier **i**nterpolation
MMSN	**M**inimum **m**ass **s**olar **n**ebula

Appendix B

Variables and Symbols

This list of variables and symbols is sorted by the first appearance of the variable and symbol.

Variable or Symbol	Explanation
T_{orb}	Local orbital time
Ω	Orbital frequency
τ_{f}	Friction time
ρ_{Roche}	Roche density
ν_{t}	Turbulent viscosity
α	Dimensionless parameter for α-disk models
c_{s}	Speed of sound
H	Gas pressure scale height
R	Radial distance to the star
R_{Hill}	Hill radius
m	Mass
$M_{\odot}$	Mass of the sun
a	Semi-major axis of orbit
e	Eccentricity of orbit
$\boldsymbol{B} = (B_x, B_y, B_z)$	Magnetic field vector and its components
$\hat{\boldsymbol{x}}, \hat{\boldsymbol{y}}, \hat{\boldsymbol{z}}$	Unit vectors in a Cartesian coordinate system
$\hat{\boldsymbol{\xi}} = (\xi_R, \xi_\phi)$	Displacement vector and its components
$\hat{\boldsymbol{R}}, \hat{\boldsymbol{\phi}}, \hat{\boldsymbol{z}}$	Unit vectors in a cylindrical coordinate system
$\boldsymbol{k} = (k_x, k_y, k_z)$	Wave vector and its components
ω	Oscillation frequency
$\boldsymbol{u} = (u_x, u_y, u_z)$	Gas velocity vector and its components
ρ	Gas volume density
$\boldsymbol{c}_{\mathrm{a}} = (v_{\mathrm{a},x}, v_{\mathrm{a},y}, v_{\mathrm{a},z})$	Alfvén velocity and its components
G	Gravitational constant
K	Spring constant
T	Tension
t	Time
K	Spring constant

Table B.1 – *Continued from previous page*

Variable or Symbol	Explanation
k_{MRI}	Wave number at which the MRI is active
λ_{MRI}	Wave length at which the MRI is active
L_x, L_y, L_z	Simulation box length
A	Amplitude of a sinusoidal density perturbation
λ	Wave length of a sinusoidal density perturbation
Δv_{HW}	Head wind
$\boldsymbol{v}_{\text{K}} = (0, u_y^{(0)}, 0)$	Keplerian velocity vector and its components
v_ϕ	Azimuthal particle velocity
$\boldsymbol{g} = (0, 0, -g)$	Gravitational acceleration vector and its components
D	Diameter
k_{RT}	Wave number of the most unstable wave length λ_{RT}
$\mathcal{A}$	Atwood number
λ_{RT}	Most unstable wave length in the RTI
ρ_1 or ρ_{top}	Density of the upper fluid in the RTI
ρ_2 or ρ_{bottom}	Density of the lower fluid in the RTI
τ_{RT}	RTI time-scale
$f_{\text{D}}(\rho)$	Mass diffusion function
P	Gas pressure
γ	Adiabatic index
ϵ	Dust-to-gas ratio
$\boldsymbol{x}^{(i)} = (x^{(i)}, y^{(i)}, z^{(i)})$	Position of particle i
$\boldsymbol{v}^{(i)} = (v_x^{(i)}, v_y^{(i)}, v_z^{(i)})$	Velocity of particle i
$\boldsymbol{f}_\nu(\boldsymbol{u}, \rho)$	Viscosity function
ρ_{P}	Dust volume density
ν_1	Constant viscosity coefficient for regular Navier-Stokes viscosity
$\boldsymbol{S}^{(1)}$	First-order rate-of-strain tensor
ν_3	Constant viscosity coefficient for regular hyper-viscosity
$\boldsymbol{S}^{(3)}$	Third-order rate-of-strain tensor
ν_{sh}	Variable viscosity coefficient for shock viscosity
c_{sh}	Constant viscosity coefficient for shock viscosity
ϵ_0	Initial dust-to-gas ratio
l_{code}	Length in code units
N_x, N_y, N_z	Grid resolution in x, y, z direction
$n_{\text{particles}}$ or N_{P}	Number of particles in a simulation
t_{code}	Time in code units
u_{max}	Maximum of the gas velocity $u = |\boldsymbol{u}|$
α_{mix}	Mixing length scaling paramter
h_{mix}	Mixing length
$\boldsymbol{J}$	Current density vector
$\boldsymbol{A} = (A_x, A_y, A_z)$	Magnetic vector potential and its components
μ_0	Vacuum permeability
$\boldsymbol{f}_\eta(\boldsymbol{A})$	Resistivity function
η_3	Constant hyper-resistivity coefficient

Table B.1 – *Continued from previous page*

Variable or Symbol	Explanation
D_3	Constant hyper-diffusion coefficient
D_{sh}	Variable diffusion coefficient for shock diffusion
ρ_0	Initial gas volume density
Δv_p	Pressure gradient velocity parameter
St	Stokes number
$q(x,y,z)$	Represents any scalar or vector field that depends on x, y, and z
$q(x,k_y,z)$	In y-direction Fourier transformed $q(x,y,z)$
$\hat{T}$	Non-linear large scale magnetic tension (in Fourier space)
τ_{mix}	Mixing time-scale
c_k	Pressure correction for small-scale modes
$\hat{F}$	Forcing term
τ_{for}	Forcing time-scale
q	Shear parameter
Q_x, Q_y, Q_z	Quality factor
τ_{corr}	Correlation time
Σ	Gas surface density
Σ_p	Dust surface density
l_p	Largest scales
l_d	Smallest scales
s	Dust grain size
Δv	Relative velocity of two particles
l_ν	Smallest turbulence length
r	Radius of spheres (around particles)
Δr	Separation of two particles
v_{min}	Lower boundary of relative velocity binning
r_{min}	Lower boundary of separation binning
v_{max}	Upper boundary of relative velocity binning
r_{max}	Upper boundary of separation binning
p_1	Particle 1
p_2	Particle 2
$N(\Delta r, \Delta v, t)$	Number of particle pairs
δv	Width of relative velocity bins in logarithmic values
$n_{bins,\Delta v}$	Number of relative velocity bins
$\Delta v_\star$	Relative velocity larger than r_{min}/τ_f
β	Power law index
$f_M(\Delta v)$	Quasi-Maxwellian fit function for velocity distributions
$f_E(\Delta v)$	Quasi-exponential fit function for velocity distributions
$f_C(\Delta v)$	Cluster fit function for velocity distributions
$f(\Delta v)$	Sum of fit function for velocity distributions
$Z(r)$	Collision rate for a single particle
Δv_c^{rms}	Root-mean-square of the relative velocity
u^{rms}	Root-mean-square of the gas velocity
H_p	Dust pressure scale height
Sc_z	Vertical Schmidt number

Table B.1 – *Continued from previous page*

Variable or Symbol	Explanation
$\rho_\bullet$	Volume density of solid material
μ	Mean molecular weight
σ_{mol}	Molecular cross section of molecular hydrogen
λ_{mfp}	Gas mean free path
$\epsilon_{\mathrm{streaming}}$	Dust-to-gas ratio at which the SI is triggered
$\epsilon_{\mathrm{Roche}}$	Dust-to-gas ratio at Roche density
Φ	Gravitational potential
C_{res}	Coefficient of restitution
τ_{coll}	Collisional time-scale
$\bar{v}(\boldsymbol{m})$	Mean particle velocity in grid cell at position $\boldsymbol{m}$
$\boldsymbol{m}$	Vector position of a grid cell
c_{p}	Velocity dispersion of the particles
M_{Ceres}	Mass of the dwarf-planet Ceres
c_{RHS}	Right-hand side parameter in Poisson equation
$v_{\mathrm{random}}(\Delta v_0)$	Random velocity uniformly distributed between 0 and Δv_0
τ_{ff}	Free fall time
ρ_{Ceres}	Mean density of the dwarf-planet Ceres
m_{min}	Lowest mass resolved in collapse simulations
s_{min}	Lowest size resolved in collapse simulations

Bibliography

Andrews, S. M., Wilner, D. J., Hughes, A. M., Qi, C., and Dullemond, C. P. (2010). Protoplanetary Disk Structures in Ophiuchus. II. Extension to Fainter Sources. ApJ, 723:1241–1254.

Balbus, S. A. and Hawley, J. F. (1991). A powerful local shear instability in weakly magnetized disks. I - Linear analysis. II - Nonlinear evolution. ApJ, 376:214–233.

Balbus, S. A. and Hawley, J. F. (1992). A Powerful Local Shear Instability in Weakly Magnetized Disks. IV. Nonaxisymmetric Perturbations. ApJ, 400:610–621.

Balbus, S. A. and Hawley, J. F. (1998). Instability, turbulence, and enhanced transport in accretion disks. *Reviews of Modern Physics*, 70:1–53.

Beitz, E., Güttler, C., Blum, J., Meisner, T., Teiser, J., and Wurm, G. (2011). Low-velocity Collisions of Centimeter-sized Dust Aggregates. ApJ, 736:34.

Bell, C. P. M., Naylor, T., Mayne, N. J., Jeffries, R. D., and Littlefair, S. P. (2013). Pre-main-sequence isochrones - II. Revising star and planet formation time-scales. MN-RAS.

Birnstiel, T., Klahr, H., and Ercolano, B. (2012). A simple model for the evolution of the dust population in protoplanetary disks. A&A, 539:A148.

Blum, J. and Wurm, G. (2008). The Growth Mechanisms of Macroscopic Bodies in Protoplanetary Disks. ARA&A, 46:21–56.

Bottke, W. F., Durda, D. D., Nesvorný, D., Jedicke, R., Morbidelli, A., Vokrouhlický, D., and Levison, H. F. (2005). Linking the collisional history of the main asteroid belt to its dynamical excitation and depletion. Icarus, 179:63–94.

Brandenburg, A., Nordlund, A., Stein, R. F., and Torkelsson, U. (1995). Dynamo-generated Turbulence and Large-Scale Magnetic Fields in a Keplerian Shear Flow. ApJ, 446:741.

Brauer, F., Dullemond, C. P., and Henning, T. (2008). Coagulation, fragmentation and radial motion of solid particles in protoplanetary disks. A&A, 480:859–877.

Cameron, A. G. W. (1962). The formation of the sun and planets. Icarus, 1:13–69.

Carballido, A., Bai, X.-N., and Cuzzi, J. N. (2011). Turbulent diffusion of large solids in a protoplanetary disc. MNRAS, 415:93–102.

Carballido, A., Fromang, S., and Papaloizou, J. (2006). Mid-plane sedimentation of large solid bodies in turbulent protoplanetary discs. MNRAS, 373:1633–1640.

Cassen, P. and Moosman, A. (1981). On the formation of protostellar disks. Icarus, 48:353–376.

Chamberlin, T. C. (1901). On a Possible Function of Disruptive Approach in the Formation of Meteorites, Comets, and Nebulae. ApJ, 14:17.

Chamberlin, T. C. (1916). The Planetesimal Hypothesis. JRASC, 10:473.

Chandarsekhar, S. (1955). The character of the equilibrium of an incompressible heavy viscous fluid of variable density. *Proc. Camb. Phil. Soc.*, 51:161–178.

Chapman, S. and Cowling, T. G. (1970). *The mathematical theory of non-uniform gases. an account of the kinetic theory of viscosity, thermal conduction and diffusion in gases*.

Cook, A. W., Cabot, W., and Miller, P. L. (2004). The mixing transition in Rayleigh-Taylor instability. *J. Fluid Mech.*, 511:333–362.

Copernicus, N. (1543). *D revolutionibus orbium coelestium*.

Cuzzi, J. N., Hogan, R. C., and Shariff, K. (2008). Toward Planetesimals: Dense Chondrule Clumps in the Protoplanetary Nebula. ApJ, 687:1432–1447.

Desch, S. J. (2007). Mass Distribution and Planet Formation in the Solar Nebula. ApJ, 671:878–893.

Dittrich, K., Klahr, H., and Johansen, A. (2013). Gravoturbulent Planetesimal Formation: The Positive Effect of Long-lived Zonal Flows. ApJ, 763:117.

Dominik, C., Blum, J., Cuzzi, J. N., and Wurm, G. (2007). Growth of Dust as the Initial Step Toward Planet Formation. *Protostars and Planets V*, pages 783–800.

Dubrulle, B., Morfill, G., and Sterzik, M. (1995). The dust subdisk in the protoplanetary nebula. Icarus, 114:237–246.

Dzyurkevich, N., Flock, M., Turner, N. J., Klahr, H., and Henning, T. (2010). Trapping solids at the inner edge of the dead zone: 3-D global MHD simulations. A&A, 515:A70.

Fedele, D., van den Ancker, M. E., Henning, T., Jayawardhana, R., and Oliveira, J. M. (2010). Timescale of mass accretion in pre-main-sequence stars. A&A, 510:A72.

Fermi, E. and von Neumann, J. (1953). Taylor instability of incompressible liquids. Part 1. Taylor instability of incompressible liquids. Part 2. Taylor instability at the boundary of two incompressible liquids. Technical Report AECU-2979, Los Alamos Scientific Laboratory.

Fleck, Jr., R. C. (1980). Turbulence and the stability of molecular clouds. ApJ, 242:1019–1022.

Flock, M., Dzyurkevich, N., Klahr, H., Turner, N., and Henning, T. (2012). Large-scale Azimuthal Structures of Turbulence in Accretion Disks: Dynamo Triggered Variability of Accretion. ApJ, 744:144.

Flock, M., Dzyurkevich, N., Klahr, H., Turner, N. J., and Henning, T. (2011). Turbulence and Steady Flows in Three-dimensional Global Stratified Magnetohydrodynamic Simulations of Accretion Disks. ApJ, 735:122.

Fromang, S. and Stone, J. M. (2009). Turbulent resistivity driven by the magnetorotational instability. A&A, 507:19–28.

Galilei, G., Kepler, J., Foscarini, P. A., and Bernegger, M. (1663). *Systema cosmicvm*.

Guan, X., Gammie, C. F., Simon, J. B., and Johnson, B. M. (2009). Locality of MHD Turbulence in Isothermal Disks. ApJ, 694:1010–1018.

Hamilton, D. P. and Burns, J. A. (1992). Orbital stability zones about asteroids. II - The destabilizing effects of eccentric orbits and of solar radiation. Icarus, 96:43–64.

Hartmann, W. K. (1985). Impact experiments. I - Ejecta velocity distributions and related results from regolith targets. Icarus, 63:69–98.

Hawley, J. F. and Balbus, S. A. (1991). A Powerful Local Shear Instability in Weakly Magnetized Disks. II. Nonlinear Evolution. ApJ, 376:223.

Hawley, J. F. and Balbus, S. A. (1992). A powerful local shear instability in weakly magnetized disks. III - Long-term evolution in a shearing sheet. ApJ, 400:595–609.

Hayashi, C. (1981). Structure of the Solar Nebula, Growth and Decay of Magnetic Fields and Effects of Magnetic and Turbulent Viscosities on the Nebula. *Progress of Theoretical Physics Supplement*, 70:35–53.

Heinemann, T. and Papaloizou, J. C. B. (2009). The excitation of spiral density waves through turbulent fluctuations in accretion discs - II. Numerical simulations with MRI-driven turbulence. MNRAS, 397:64–74.

Hester, J. J., Stone, J. M., Scowen, P. A., Jun, B.-I., Gallagher, III, J. S., Norman, M. L., Ballester, G. E., Burrows, C. J., Casertano, S., Clarke, J. T., Crisp, D., Griffiths, R. E., Hoessel, J. G., Holtzman, J. A., Krist, J., Mould, J. R., Sankrit, R., Stapelfeldt, K. R., Trauger, J. T., Watson, A., and Westphal, J. A. (1996). WFPC2 Studies of the Crab Nebula. III. Magnetic Rayleigh-Taylor Instabilities and the Origin of the Filaments. ApJ, 456:225.

Hillier, A., Berger, T., Isobe, H., and Shibata, K. (2012). Numerical Simulations of the Magnetic Rayleigh-Taylor Instability in the Kippenhahn-Schlüter Prominence Model. I. Formation of Upflows. ApJ, 746:120.

Hoyle, F. (1960). The Origin of the Solar Nebula. QJRAS, 1:28.

Hubbard, A. (2012). Turbulence-induced collisional velocities and density enhancements: large inertial range results from shell models. MNRAS, 426:784–795.

Hubbard, A. (2013). Turbulence-induced collision velocities and rates between differ-ent sized dust grains. MNRAS, 432:1274–1284.

Ida, S., Guillot, T., and Morbidelli, A. (2008). Accretion and Destruction of Planetesi-mals in Turbulent Disks. ApJ, 686:1292–1301.

Jeans, J. H. (1902). The Stability of a Spherical Nebula. *Royal Society of London Philo-sophical Transactions Series A*, 199:1–53.

Johansen, A., Klahr, H., and Henning, T. (2011). High-resolution simulations of plan-etesimal formation in turbulent protoplanetary discs. A&A, 529:A62.

Johansen, A., Oishi, J. S., Mac Low, M.-M., Klahr, H., Henning, T., and Youdin, A. (2007). Rapid planetesimal formation in turbulent circumstellar disks. Nature, 448:1022–1025.

Johansen, A. and Youdin, A. (2007). Protoplanetary Disk Turbulence Driven by the Streaming Instability: Nonlinear Saturation and Particle Concentration. ApJ, 662:627–641.

Johansen, A., Youdin, A., and Klahr, H. (2009a). Zonal Flows and Long-lived Axisym-metric Pressure Bumps in Magnetorotational Turbulence. ApJ, 697:1269–1289.

Johansen, A., Youdin, A., and Mac Low, M.-M. (2009b). Particle Clumping and Plan-etesimal Formation Depend Strongly on Metallicity. ApJ, 704:L75–L79.

Johansen, A., Youdin, A. N., and Lithwick, Y. (2012). Adding particle collisions to the formation of asteroids and Kuiper belt objects via streaming instabilities. A&A, 537:A125.

Kant, I. (1755). *Allgemeine Naturgeschichte und Theorie des Himmels*.

Klahr, H. H. and Lin, D. N. C. (2001). Dust Distribution in Gas Disks: A Model for the Ring around HR 4796A. ApJ, 554:1095–1109.

Kopal, Z., editor (1989). *The Roche problem and its significance for double-star astronomy*, volume 152 of *Astrophysics and Space Science Library*.

Laplace, P. S. and Young, T. (1832). *Elementary illustrations of the celestial mechanics of Laplace.*

Lyra, W., Johansen, A., Klahr, H., and Piskunov, N. (2008). Global magnetohydrody-namical models of turbulence in protoplanetary disks. I. A cylindrical potential on a Cartesian grid and transport of solids. A&A, 479:883–901.

Mendigutía, I., Calvet, N., Montesinos, B., Mora, A., Muzerolle, J., Eiroa, C., Oud-maijer, R. D., and Merín, B. (2011). Accretion rates and accretion tracers of Herbig Ae/Be stars. A&A, 535:A99.

Mendigutía, I., Mora, A., Montesinos, B., Eiroa, C., Meeus, G., Merín, B., and Oudmai-jer, R. D. (2012). Accretion-related properties of Herbig Ae/Be stars. Comparison with T Tauris. A&A, 543:A59.

Moulton, F. R. (1905). On the Evolution of the Solar System. ApJ, 22:165.

Nakagawa, Y., Sekiya, M., and Hayashi, C. (1986). Settling and growth of dust particles in a laminar phase of a low-mass solar nebula. Icarus, 67:375–390.

Nesvorný, D., Vokrouhlický, D., Bottke, W. F., Noll, K., and Levison, H. F. (2011). Observed Binary Fraction Sets Limits on the Extent of Collisional Grinding in the Kuiper Belt. AJ, 141:159.

Nesvorný, D., Youdin, A. N., and Richardson, D. C. (2010). Formation of Kuiper Belt Binaries by Gravitational Collapse. AJ, 140:785–793.

Noll, K. S., Grundy, W. M., Chiang, E. I., Margot, J.-L., and Kern, S. D. (2008a). *Binaries in the Kuiper Belt*, pages 345–363.

Noll, K. S., Grundy, W. M., Stephens, D. C., Levison, H. F., and Kern, S. D. (2008b). Evidence for two populations of classical transneptunian objects: The strong inclination dependence of classical binaries. Icarus, 194:758–768.

Ormel, C. W. and Cuzzi, J. N. (2007). Closed-form expressions for particle relative velocities induced by turbulence. A&A, 466:413–420.

Pan, L. and Padoan, P. (2013). Turbulence-Induced Relative Velocity of Dust Particles I: Identical Particles. *ArXiv e-prints*.

Pan, L., Padoan, P., Scalo, J., Kritsuk, A. G., and Norman, M. L. (2011). Turbulent Clustering of Protoplanetary Dust and Planetesimal Formation. ApJ, 740:6.

Pinilla, P., Birnstiel, T., Ricci, L., Dullemond, C. P., Uribe, A. L., Testi, L., and Natta, A. (2012). Trapping dust particles in the outer regions of protoplanetary disks. A&A, 538:A114.

Press, W. H., Teukolsky, S. A., Vetterling, W. T., and Flannery, B. P. (1992). *Numerical recipes in FORTRAN. The art of scientific computing*.

Rayleigh, L. (1882). Investigations of the character of the equilibrium of an incompressible heavy fluid of variable density. *Proceedings of the London Mathematical Society*, 14:170–177.

Safronov, V. S. (1969). *Evoliutsiia doplanetnogo oblaka*.

Shakura, N. I. and Sunyaev, R. A. (1973). Black holes in binary systems. Observational appearance. A&A, 24:337–355.

Simon, J. B., Beckwith, K., and Armitage, P. J. (2012). Emergent mesoscale phenomena in magnetized accretion disc turbulence. MNRAS, 422:2685–2700.

Sorathia, K. A., Reynolds, C. S., Stone, J. M., and Beckwith, K. (2012). Global Simulations of Accretion Disks. I. Convergence and Comparisons with Local Models. ApJ, 749:189.

Stone, J. M. and Gardiner, T. A. (2010). Implementation of the Shearing Box Approximation in Athena. ApJS, 189:142–155.

Swedenborg, E. (1734). *Opera Philosophica et Mineralia (English: Philosophical and Mineralogical Works)*, volume 1.

Taylor, G. (1950). The Instability of Liquid Surfaces when Accelerated in a Direction Perpendicular to their Planes. I. *Royal Society of London Proceedings Series A*, 201:192–196.

Terebey, S., Shu, F. H., and Cassen, P. (1984). The collapse of the cores of slowly rotating isothermal clouds. ApJ, 286:529–551.

Thomas, P. C., Parker, J. W., McFadden, L. A., Russell, C. T., Stern, S. A., Sykes, M. V., and Young, E. F. (2005). Differentiation of the asteroid Ceres as revealed by its shape. Nature, 437:224–226.

Tsiganis, K., Gomes, R., Morbidelli, A., and Levison, H. F. (2005). Origin of the orbital architecture of the giant planets of the Solar System. Nature, 435:459–461.

Uribe, A. L., Klahr, H., Flock, M., and Henning, T. (2011). Three-dimensional Magnetohydrodynamic Simulations of Planet Migration in Turbulent Stratified Disks. ApJ, 736:85.

von Neumann, J. and Richtmyer, R. D. (1950). A Method for the Numerical Calculation of Hydrodynamic Shocks. *Journal of Applied Physics*, 21:232–237.

Weidenschilling, S. J. (1976). Accretion of the terrestrial planets. II. Icarus, 27:161–170.

Weidenschilling, S. J. (1977a). Aerodynamics of solid bodies in the solar nebula. MNRAS, 180:57–70.

Weidenschilling, S. J. (1977b). The distribution of mass in the planetary system and solar nebula. Ap&SS, 51:153–158.

Weidenschilling, S. J., Spaute, D., Davis, D. R., Marzari, F., and Ohtsuki, K. (1997). Accretional Evolution of a Planetesimal Swarm. Icarus, 128:429–455.

Weizsäcker, C. F. V. (1943). Über die Entstehung des Planetensystems. Mit 2 Abbildungen. ZAp, 22:319.

Weizsäcker, C. F. V. (1951). The Evolution of Galaxies and Stars. ApJ, 114:165.

Whipple, F. L. (1972). On certain aerodynamic processes for asteroids and comets. In Elvius, A., editor, *From Plasma to Planet*, page 211.

Windmark, F., Birnstiel, T., Güttler, C., Blum, J., Dullemond, C. P., and Henning, T. (2012a). Planetesimal formation by sweep-up: how the bouncing barrier can be beneficial to growth. A&A, 540:A73.

Windmark, F., Birnstiel, T., Ormel, C. W., and Dullemond, C. P. (2012b). Breaking through: The effects of a velocity distribution on barriers to dust growth. A&A, 544:L16.

Youdin, A. and Johansen, A. (2007). Protoplanetary Disk Turbulence Driven by the Streaming Instability: Linear Evolution and Numerical Methods. ApJ, 662:613–626.

Youdin, A. N. and Goodman, J. (2005). Streaming Instabilities in Protoplanetary Disks. ApJ, 620:459–469.

Youdin, A. N. and Lithwick, Y. (2007). Particle stirring in turbulent gas disks: Including orbital oscillations. Icarus, 192:588–604.

Youngs, D. L. (1984). Numerical simulation of turbulent mixing by Rayleigh-Taylor instability. *Physica*, 12:32–44.

Zhou, J.-L. and Lin, D. N. C. (2007). Planetesimal Accretion onto Growing Proto-Gas Giant Planets. ApJ, 666:447–465.

Zsom, A., Ormel, C. W., Güttler, C., Blum, J., and Dullemond, C. P. (2010). The outcome of protoplanetary dust growth: pebbles, boulders, or planetesimals? II. Introducing the bouncing barrier. A&A, 513:A57.

Acknowledgment